



University of Strathclyde

Department of Pure and Applied Chemistry

Raman Spectroscopic Techniques for the Detection of Malaria Parasite  
Infection

By Laura Frame

A thesis submitted to the Department of Pure and Applied Chemistry, University of Strathclyde, in fulfilment of the requirements for the degree of Doctor of Philosophy.

JUNE 2017

This thesis is the result of the author's original research. It has been composed by the author and has not been previously submitted for examination which has led to the award of a degree. The copyright of this thesis belongs to the author under the terms of the United Kingdom Copyright Acts as qualified by University of Strathclyde Regulation 3.50. Due acknowledgement must always be made of the use of any material contained in, or derived from, this thesis.

Signed:

Date:

Previously published material:

1. The 532 nm Raman imaging data within Chapter 3, Section 3.2 was published prior to the completion of this thesis – *‘Development of a label-free Raman imaging technique for differentiation of malaria parasite infected from non-infected tissue’*

L. Frame, J. Brewer, R. Lee, K. Faulds, and D. Graham, *Analyst*, 2018, **143**, 157-163.

I was responsible for all aspects of the research and the preparation of the publication. Rebecca Lee, University of Glasgow, provided the tissue sections.

Signed:

Date:

## Acknowledgements

---

I would like to start by thanking my supervisors Professor Duncan Graham and Professor Karen Faulds for allowing me to carry out my PhD within the group and for all their input and guidance throughout. For all the discussions and endless help with my work, I would like to thank all the post docs within the group both past and present. Particularly to Dr. Kirsten Gracie for all her help with all my endless conjugation questions, Dr. Samuel Mabbott for answering so many of my questions throughout my PhD, Dr. Lauren Jamieson for always being available to help and share your knowledge and reading over my thesis, and to Dr. Stacey Laing for all your comments and corrections on my thesis.

Thank you to all the PhD students within the group for fun nights out and lots of laughter within the office. But a massive thank you to all of Vegas: Craig, Fay, Sian, Rachel, Ryan, and Alex! Thank you for all our science chat, listening to my moans and for the amazing Scix trips!!

Finally, the biggest thank you to my family and friends! To my mum and dad for always supporting me throughout my undergraduate degree and PhD. And to David for putting up with me, being the one who has had to listen to my complaints and keep me sane, particularly in the last year of my PhD. I am so thankful for everything you have done. Now I'm finished I can get a real job!!

## Abstract

---

Raman spectroscopy and its analogues, surface enhanced (resonance) Raman scattering (SERS and SERRS) have been widely applied in malaria research to target early diagnosis of malaria infection in blood or plasma samples primarily *via* the identification of the infection specific biomarker hemozoin. However, the capability of Raman spectroscopy to contribute to tackling other areas of malaria research is not as thoroughly investigated. In this work two such areas were studied. The first looked to utilise Raman spectroscopy to differentiate malaria parasite infected tissue from non-infected and the second investigated coupling portable Raman with malaria diagnostic tests to improve detection levels.

Research commenced by investigating the potential of Raman spectroscopy to detect tissue burden within malaria infected samples. Sequestration of parasite infected red blood cells in the vascular endothelium is associated with features of severe malaria pathology such as cerebral malaria. Currently, there is difficulty in assessing the presence of parasites sequestered within tissue during the progression of the infection, with many reported studies carried out post-mortem. Raman imaging coupled with chemometric analysis showed very clear separation of malaria infected mice spleen sections from non-infected, with an associated increase in concentration of heme-based Raman vibrations within the infected dataset. An *in-vivo* mouse study also highlighted the ability of Raman spectroscopy to gain biological information from whole organs. These results demonstrated that Raman spectroscopy can be used to easily discriminate the subtle changes in tissue burden upon malarial infection within tissue sections.

Finally, the coupling of rapid diagnostic tests with a handheld portable Raman spectrometer for the detection of HRP-II malaria biomarker *via* SERRS was investigated. By applying a 3D-microfluidic paper-based device in a sandwich assay format, SERRS detection gave a theoretical LoD of 1.68 ng/mL HRP-II which converted to  $\sim 22$  parasites/ $\mu\text{L}$  ( $\sim 0.00044$  % parasitemia). This detection limit of infection density was lower than what is typically capable of a technician analysing a blood smear by

light microscopy (~100 parasites/ $\mu\text{L}$ , 0.002 % parasitemia), which is a current gold standard detection method. The results displayed the advantages of high sensitivity and specificity gained from SERRS and as it was conducted on a portable Raman spectrometer it has the potential to be implemented as a point-of-care method. This coupling could be applied to enhance the detection capabilities of the already widely applied rapid diagnostic tests. The possibility of being able to reliably detect lower-density parasitemia with this SERRS-3D- $\mu\text{PAD}$  could also allow positive malaria identification in asymptomatic individuals.

## Abbreviations

---

|                       |  |
|-----------------------|--|
| $\mu$ PADs            | Microfluidic paper-based analytical devices        |
| Ab                    | Antibody   |
| Ag                    | Silver   |
| Au                    | Gold   |
| BSA                   | Bovine serum albumin                               |
| CaF <sub>2</sub>      | Calcium fluoride                                   |
| CT(PEG) <sub>12</sub> | Carboxy-polyethylene glycol-thiol                  |
| dH <sub>2</sub> O     | Deionised water                                    |
| DLS                   | Dynamic light scattering                           |
| EDC                   | 1-ethyl-3-(3-dimethylaminopropyl) carbodiimide     |
| Fab                   | Fragment antigen binding                           |
| Fc                    | Fragment crystallisable                            |
| FWHM                  | Full width half maximum                            |
| Hb                    | Hemoglobin   |
| HEPES                 | 4-(2-Hydroxyethyl)-1-Piperazineethanesulfonic Acid |
| HRP-II                | Histidine-rich protein II                          |
| Hz                    | Hemozoin   |
| Ig                    | Immunoglobulin                                     |
| IgG                   | Immunoglobulin G                                   |
| IR                    | Infra-red  |
| kDa                   | kilodalton   |
| LoD                   | Limit of detection                                 |
| LSPR                  | Localised surface plasmon resonance                |
| MGITC                 | Malachite green isothiocyanate                     |
| NIR                   | Near infra-red                                     |
| ORS                   | Orbital raster scanning                            |

|                      |   |
|----------------------|---|
| <i>P. berghei</i>    | <i>Plasmodium berghei</i>                                   |
| <i>P. falciparum</i> | <i>Plasmodium falciparum</i>                                |
| PfEMP1               | <i>Plasmodium falciparum</i> erythrocyte membrane protein 1 |
| PB                   | Phosphate buffer  |
| PBS                  | Phosphate buffer saline                                     |
| PCA                  | Principal component analysis                                |
| RBCs                 | Red blood cells   |
| RDTs                 | Rapid diagnostic tests                                      |
| RRS                  | Resonance Raman scattering                                  |
| R.T.                 | Room temperature  |
| SEM                  | Scanning electron microscopy                                |
| SERRS                | Surface enhanced resonance Raman scattering                 |
| SERS                 | Surface enhanced Raman scattering                           |
| sHz                  | Synthetic hemozoin  |
| sNHS                 | N-hydroxysulfosuccinimide                                   |
| SORS                 | Spatially offset Raman spectroscopy                         |



# Contents

---

|  |     |
|--|-----|
| Acknowledgements.....  | iv  |
| Abstract.....  | v   |
| Abbreviations .....  | vii |
| Contents.....  | ix  |
| 1 Introduction .....   | 1   |
| 1.1 Nanoparticles .....  | 1   |
| 1.1.1 Localised surface plasmon resonance .....                      | 2   |
| 1.2 Raman Spectroscopy .....   | 3   |
| 1.2.1 Theory of Raman scattering.....                                | 3   |
| 1.2.2 Resonance Raman scattering.....                                | 5   |
| 1.2.3 Surface enhanced Raman scattering (SERS) .....                 | 7   |
| 1.2.4 Surface enhanced resonance Raman scattering (SERRS) .....      | 8   |
| 1.2.5 Raman imaging.....   | 9   |
| 1.3 An introduction to malaria .....                                 | 9   |
| 1.3.1 Malaria parasite .....   | 10  |
| 1.3.2 Lifecycle of malaria parasite .....                            | 11  |
| 1.3.3 Malaria biomarkers .....                                       | 12  |
| 1.3.3.1 Hemozoin.....  | 12  |
| 1.3.3.2 Histidine-rich protein-II.....                               | 14  |
| 1.3.3.3 Plasmodium lactate dehydrogenase .....                       | 14  |
| 1.3.3.4 Plasmodium aldolase.....                                     | 15  |
| 1.3.4 Current malaria diagnosis techniques .....                     | 15  |
| 1.3.4.1 Clinical diagnosis.....                                      | 15  |
| 1.3.4.2 Microscopic diagnosis.....                                   | 15  |
| 1.3.4.3 Rapid diagnostic tests .....                                 | 16  |
| 1.3.5 Applications of Raman in malaria diagnosis .....               | 18  |
| 2 Project aims .....   | 20  |
| 3 Label-free Raman imaging of malaria parasite infected tissue ..... | 21  |
| 3.1 Introduction.....  | 21  |

|         |  |     |
|---------|--|-----|
| 3.1.1   | Parasite sequestration .....   | 21  |
| 3.1.2   | Raman analysis of biological tissue samples.....                     | 24  |
| 3.1.3   | Choice of Raman excitation wavelength.....                           | 26  |
| 3.2     | Results and discussion .....   | 28  |
| 3.2.1   | 2D Raman imaging .....   | 29  |
| 3.2.2   | Empirical analysis .....   | 36  |
| 3.2.3   | Principal component analysis .....                                   | 39  |
| 3.2.4   | Animal models.....   | 50  |
| 3.3     | Concluding Remarks .....   | 61  |
| 4       | Lateral flow assay and 3D-paper-based microfluidic device .....      | 65  |
| 4.1     | Introduction.....  | 65  |
| 4.1.1   | Antibodies .....   | 65  |
| 4.1.2   | Lateral flow immunoassays.....                                       | 67  |
| 4.1.3   | Microfluidic paper-based devices .....                               | 68  |
| 4.2     | Results and discussion .....   | 71  |
| 4.2.1   | Au nanoparticle synthesis and characterisation.....                  | 71  |
| 4.2.2   | Antibody conjugated Au nanoparticles.....                            | 72  |
| 4.2.2.1 | MGITC functionalisation to Au nanoparticles.....                     | 73  |
| 4.2.2.2 | Carbodiimide crosslinking conjugation.....                           | 75  |
| 4.2.3   | Development of a lateral flow immunoassay for HRP-II detection ..... | 81  |
| 4.2.3.1 | Immunoassay design and SERRS detection .....                         | 82  |
| 4.2.3.2 | Quantitative analysis of HRP-II using SERRS.....                     | 85  |
| 4.2.3.3 | Colourimetric analysis to quantify HRP-II.....                       | 90  |
| 4.2.3.4 | Issues with lateral flow immunoassay .....                           | 91  |
| 4.2.4   | 3D- $\mu$ PAD for HRP-II detection .....                             | 92  |
| 4.2.4.1 | Running and optimisation of the 3D device .....                      | 92  |
| 4.2.4.2 | SERRS quantitative analysis of the capture layer .....               | 96  |
| 4.2.4.3 | Colourimetric analysis of the capture layer.....                     | 100 |
| 4.2.4.4 | 3D- $\mu$ PAD selectivity .....                                      | 102 |
| 4.2.4.5 | HRP-II detection in a biologically relevant matrix .....             | 103 |
| 4.3     | Concluding Remarks .....   | 106 |
| 5       | Experimental.....  | 108 |

|         |  |     |
|---------|--|-----|
| 5.1     | Materials.....   | 108 |
| 5.1.1   | Chemicals .....  | 108 |
| 5.1.2   | Buffer Preparation .....   | 108 |
| 5.1.2.1 | PBS .....  | 108 |
| 5.1.2.2 | PB .....   | 108 |
| 5.1.2.3 | HEPES buffer .....   | 108 |
| 5.2     | Instrumentation.....   | 108 |
| 5.2.1   | Extinction spectroscopy .....                                      | 108 |
| 5.2.2   | DLS and zeta potential .....                                       | 109 |
| 5.2.3   | SEM measurements .....   | 109 |
| 5.2.4   | IR measurements .....  | 109 |
| 5.3     | Tissue work.....   | 109 |
| 5.3.1   | Infections and tissue preparation .....                            | 109 |
| 5.3.2   | Poly-L-lysine coating of Raman-grade CaF <sub>2</sub> slides ..... | 110 |
| 5.3.3   | Synthetic hemozoin preparation .....                               | 110 |
| 5.3.4   | Reference spectra .....  | 110 |
| 5.3.5   | Raman mapping .....  | 111 |
| 5.3.6   | PCA Analysis .....   | 111 |
| 5.3.7   | Prussian blue staining of tissue.....                              | 111 |
| 5.3.8   | Animal model .....   | 112 |
| 5.4     | Lateral flow assay and 3D-paper-based microfluidic device.....     | 113 |
| 5.4.1   | Synthesis of Au nanoparticles .....                                | 113 |
| 5.4.2   | SEM preparation .....  | 113 |
| 5.4.3   | Antibody conjugated Au nanoparticles.....                          | 113 |
| 5.4.3.1 | MGITC functionalisation to Au nanoparticles.....                   | 113 |
| 5.4.3.2 | Carbodiimide crosslinking conjugation.....                         | 114 |
| 5.4.3.3 | Gel electrophoresis.....   | 114 |
| 5.4.3.4 | Lateral flow immunoassay .....                                     | 114 |
| 5.4.4   | Fabrication and running of lateral flow immunoassay .....          | 115 |
| 5.4.4.1 | SERRS quantification.....  | 115 |
| 5.4.4.2 | Colourimetric quantification.....                                  | 116 |
| 5.4.5   | Fabrication and running of the 3D- $\mu$ PAD.....                  | 116 |

|         |  |     |
|---------|--|-----|
| 5.4.5.1 | SERRS quantification .....                             | 117 |
| 5.4.5.2 | Colourimetric quantification.....                      | 117 |
| 5.4.5.3 | 3D- $\mu$ PAD selectivity .....                        | 117 |
| 5.4.5.4 | HRP-II detection in biologically relevant matrix ..... | 118 |
| 6       | Conclusions .....                                      | 119 |
| 7       | References .....                                       | 124 |
|         | Appendices.....  | 134 |

# 1 Introduction

---

## 1.1 Nanoparticles

Nanoparticles are defined as particles with one or more dimensions less than 100 nm in size.<sup>1</sup> They are of great interest due to their unique properties that differ from the bulk material, including their interaction with light and properties such as size, shape, and colour which can be tuned to suit a particular application. A number of metallic elements, such as gold (Au),<sup>2</sup> silver (Ag),<sup>3</sup> iron,<sup>4</sup> and platinum,<sup>5</sup> can be found as colloidal suspensions.

Examples of the use of nanoparticles can be seen throughout history, with one of the most famous being the Lycurgus cup, dating back to 4<sup>th</sup> century A.D. The cup was found to have Ag and Au nanocrystals incorporated into the glass which gave it its unique optical properties. These tiny crystals change the visual colour of the cup, with it appearing green in reflected light but ruby red in scattered light.<sup>6</sup> In current research, nanoparticles are also being applied in areas such as cancer cell imaging,<sup>7</sup> biosensing<sup>8</sup> and DNA detection,<sup>9</sup> with Au and Ag nanoparticles being the most popular form of nanomaterial used for optical applications.

Nanoparticles are most commonly synthesised *via* the chemical reduction of metal salts by reducing agents such as trisodium citrate,<sup>2,10</sup> ethylenediaminetetraacetic acid (EDTA)<sup>11</sup> or sodium borohydride.<sup>12</sup> Surface functionalisation of the nanoparticles can also be carried out to impart selectivity and sensitivity for the specific target analytes that do not have sufficient specific affinity to the metal surface. An example of this is the conjugation of nanoparticles with antibodies, which combines the properties of the nanoparticles themselves with the specific and selective recognition capabilities of the antibody to the target antigen.<sup>13</sup>

Their unique optical properties coupled with the ability to control their size, shape, and surface chemistry make nanoparticles preferred substrates for diagnostic applications. The most commonly exploited property of metallic nanoparticles is their

associated localised surface plasmon resonance, which occurs when the nanoparticles interact with light of a specific wavelength.

### 1.1.1 Localised surface plasmon resonance

Nanomaterials consisting of metals, such as Au and Ag, display a strong surface plasmon band in their extinction spectra due to their unique interaction with incident light. This localised surface plasmon resonance (LSPR) arises due to the collective oscillation of conduction band electrons on the surface of the nanoparticles which occurs in the presence of an applied electromagnetic field (Figure 1.1).<sup>14,15</sup>

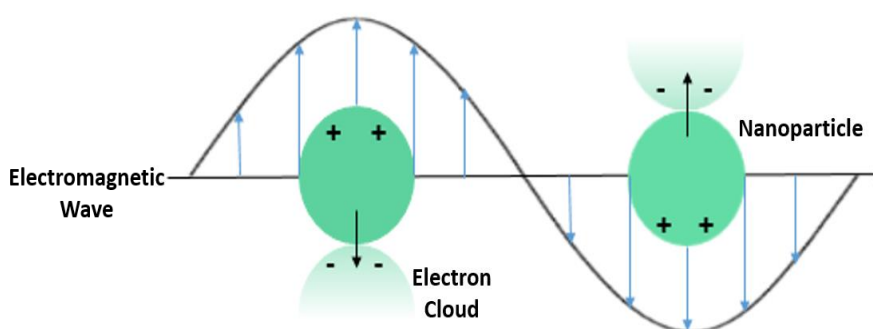


**Figure 1.1** Schematic representation of the localised surface plasmon resonance showing the oscillation of electrons in spherical metal nanoparticles in an applied electromagnetic field.

Gustav Mie first described the LSPR phenomenon in 1908, when he solved Maxwell's equation for spherical nanoparticles.<sup>16</sup> He concluded that the plasmon band was due to dipole oscillations of the free electrons in the conduction band occupying the energy states directly above the Fermi energy level.<sup>15</sup> The surface plasmon band for ~20 nm Au nanoparticles is ~520 nm<sup>15</sup> and for ~35 nm Ag nanoparticles it is ~400 nm.<sup>3</sup> However, the surface plasmon band will shift depending on nanoparticle size, shape, the inter-particle distance and changes in the local environment such as the refractive index or the surrounding medium.<sup>17</sup>

An important feature of nanoparticles' LSPR, which makes them ideal for bio-sensing applications, is the distance dependant nature of the surface plasmon band. As the inter-particle distance of the nanoparticles decreases, coupling of the surface plasmons occur, resulting in a red-shift of the nanoparticle extinction to longer

wavelengths.<sup>18</sup> Larger red-shifts result as the inter-particle distance becomes shorter. This surface plasmon coupling can also be monitored through a colour change, for example Au nanoparticles change from red to purple when the interparticle distance decreases.<sup>19</sup> The ability to cause controlled aggregation of nanoparticles, and in turn have an observable colour change, has led to the development of colorimetric biosensors for the detection of biological analytes such as DNA,<sup>20,21</sup> oligonucleotides,<sup>22</sup> and proteins.<sup>23</sup> With one of the most well-known biosensors being the home pregnancy test. Not only can biorecognition events be detected through changes to the nanoparticles' extinction spectra, but they can also be studied through the enhancement of the molecules' Raman scattering due to the presence of nanoparticles.

## **1.2 Raman Spectroscopy**

Raman spectroscopy is a structural characterisation technique which relies on the inelastic scattering of monochromatic light. The process of inelastic scattering of photons was first postulated in 1923 by Smekal,<sup>24</sup> however, the 'Raman effect' was not observed experimentally until 1928 by Raman and Krishnan.<sup>25</sup> This experiment showed the existence of scattered radiation and proved that it had an altered frequency from the incident light.<sup>26</sup> These findings formed the basic characteristics of Raman spectroscopy.

### *1.2.1 Theory of Raman scattering*

When a photon of light interacts with a molecule, polarisation of the molecules surrounding electron cloud occurs, which results in a short lived excited 'virtual state'.<sup>27</sup> Rayleigh (or elastic) scattering, which is the dominant process, involves only the distortion of the electron cloud without any nuclear movement, resulting in small changes in the frequency. The photon is therefore scattered at the same frequency as the incident light.<sup>28</sup> However, if nuclear motion is induced during the scattering process, a transfer of energy from the incident photon to the molecule (Stokes scattering) or a transfer of energy from the molecule to the scattered photon (anti-

Stokes scattering) will occur.<sup>29</sup> In this instance, a change of energy by one vibrational unit occurs and this is known as Raman (or inelastic) scattering. These scattering processes are shown in the form of a Jablonski diagram in Figure 1.2.

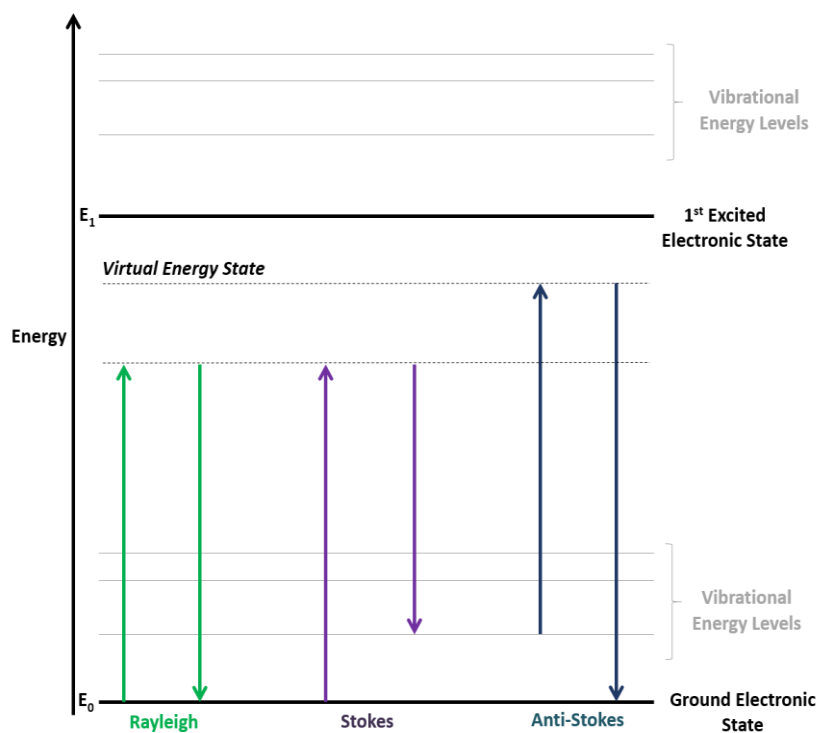


Figure 1.2 A Jablonski diagram illustrating the processes of Rayleigh and Raman scattering

In Stokes scattering, the photons are scattered with less energy than the incident photons, as the molecules are promoted to a higher energy excited vibrational state from the ground state. At higher temperatures, some molecules will be in an excited vibrational state and when these molecules lose energy to the scattered photons and return to the ground state, anti-Stokes scattering occurs.<sup>26</sup> At room temperature, most molecules will be in the ground vibrational state, therefore the intensity of Stokes scattering is likely to be greater than that of anti-Stokes scattering and so Stokes scattering is most commonly recorded. The population of the energy levels and the ratio of the intensities of Stokes and anti-Stokes scattering can be calculated using the Boltzmann equation<sup>30</sup> (Equation 1.1), where  $N_n$  is the number of molecules



in the excited vibrational energy level,  $N_m$  is the number of molecules in the ground vibrational energy level,  $g$  is the degeneracy of the energy level,  $E_n - E_m$  is the difference in energy between the vibrational energy levels  $E_n$  and  $E_m$ ,  $k$  is the Boltzmann constant ( $1.3807 \times 10^{-23} \text{ JK}^{-1}$ ) and  $T$  is the temperature (K).

**Equation 1.1** Boltzmann Equation

$$\frac{N_n}{N_m} = \frac{g_n}{g_m} \exp \left[ \frac{-(E_n - E_m)}{kT} \right]$$

However, Raman scattering is an inherently weak process with only one in every  $10^6 - 10^8$  scattered photons being Raman scattered.<sup>26</sup> The intensity of the Raman scattering can be described by Equation 1.2, where  $I$  is the Raman intensity,  $K$  consists of constants including the speed of light,  $I_L$  is the laser power,  $\alpha$  is the polarizability of the electrons in the molecule and  $\omega$  is the frequency of the incident radiation.

**Equation 1.2** Intensity of Raman scattering

$$I = KI_L \alpha^2 \omega^4$$

By changing the laser power ( $I_L$ ) and the frequency ( $\omega$ ), the Raman scattering intensity can be maximised. From the equation, the intensity ( $I$ ) has a 4<sup>th</sup> power dependency on the excitation frequency, therefore, the lower the excitation wavelength that is used e.g. in the UV region, the more intense the Raman scattering will be.<sup>26</sup> Although many compounds will absorb UV radiation and along with higher energy photons in this region, issues with sample burning and degradation can occur.<sup>31</sup> To overcome these problems and improve the signal obtained from Raman scattering, the techniques of resonance Raman and surface enhanced Raman scattering have been developed.<sup>26</sup>

### 1.2.2 Resonance Raman scattering

The sensitivity and selectivity of Raman scattering may be enhanced by choosing a laser frequency close to an electronic transition in the molecule of interest.<sup>26</sup> This

effect, known as resonance Raman scattering (RRS), has been reported to give signal enhancements of up to  $10^6$ ; however, it is more typically in the region of  $10^3 - 10^4$ .<sup>32</sup> When using RRS the absorption of a photon induces the excitation of the molecule into an excited electronic vibrational state, as opposed to Raman scattering where excitation is to a virtual state (Figure 1.3). As a result, when RRS is employed, electronic and vibrational information of the molecule is simultaneously obtained<sup>26</sup> which can allow the identification of selected chromophore molecules within complex biological matrices, such as heme structures within hemoglobin.<sup>32</sup>

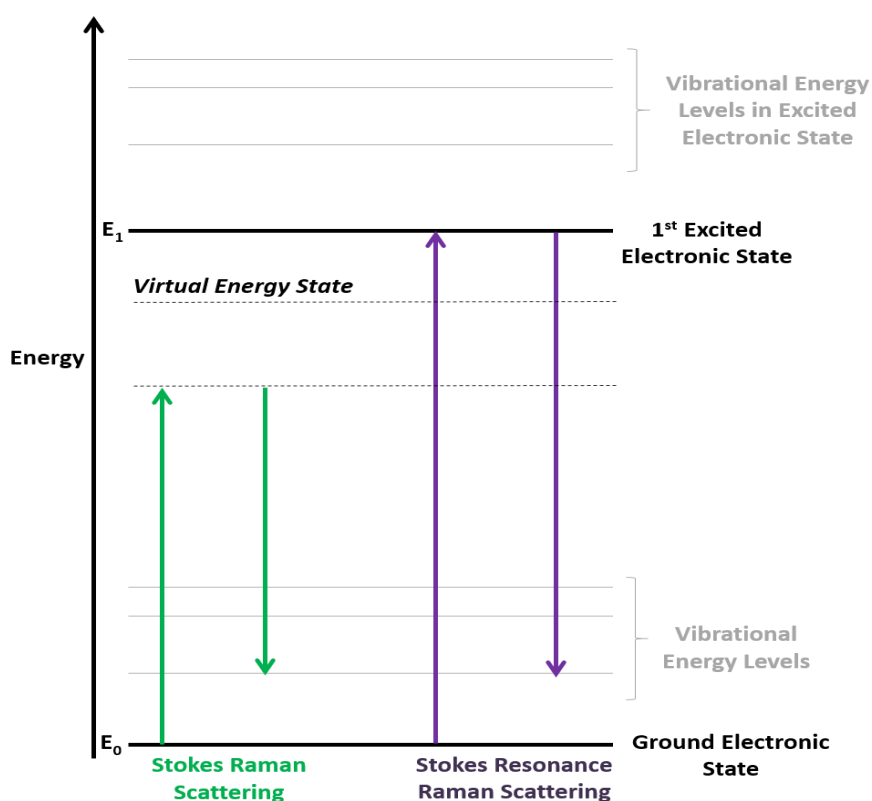


**Figure 1.3** A Jablonski diagram illustrating the processes of Raman and resonance Raman scattering

RRS does have problems with sample degradation and competing fluorescence processes that can result in a high, unwanted fluorescence background. However, by making use of the time discrimination between fluorescence, which takes places over a nanosecond as nuclei relax to equilibrium geometry of the excited state, and Raman scattering that occurs before nuclei reach equilibrium positions in the excited state,

interference can be minimised.<sup>26</sup> To overcome the limitations of RRS, particularly fluorescence backgrounds, surface enhanced Raman scattering can be used.

### 1.2.3 Surface enhanced Raman scattering (SERS)

The phenomenon of SERS was first observed in 1974 by Fleischmann *et al.*<sup>33</sup> who reported an intense Raman signal from pyridine on a roughened Ag electrode, which showed enhancement in comparison to adsorption on a smooth Ag electrode. This enhancement was initially attributed to an increase in surface area allowing more pyridine to adsorb on to the surface, however, subsequent studies later came up with different theories which both disputed Fleischmann's hypothesis.<sup>34,35</sup> Jeanmaire and Van Duyne proposed that the enhancement was due to an electromagnetic effect<sup>34</sup> whereas Albrecht and Creighton suggested a charge transfer effect.<sup>35</sup>

It is widely accepted that SERS enhancement is a combination of both the electromagnetic and charge transfer effects; however, the electromagnetic enhancement is the dominant process. This occurs when an analyte is adsorbed onto or held in close proximity to a roughened metal surface, *i.e.* nanoparticles, resulting in an interaction between the analyte molecules and the surface plasmons.<sup>36</sup> When incident light interacts with the nanoparticle surface it causes the localised surface plasmons to oscillate, which increases the local field that is experienced by the analyte, causing greater polarisation around the molecule and thus increasing the resulting scattering. To create scattering, the metal surface must be roughened to create a component of the plasmon with a vector perpendicular to the surface.<sup>37</sup> However, the greatest enhancement does not occur evenly around all isolated particles but at points where nanoparticles are touching or are clustered. These points are known as 'hot spots' where the interstices between nanoparticles generate large electric fields, resulting in strong SERS responses in these areas.<sup>26</sup>

Chemical, or charge transfer, enhancement involves the formation of a bond between the analyte and metal surface.<sup>37</sup> This interaction induces a charge transfer between the analyte and the metal, creating new electronic states that are in

resonance with the laser excitation wavelength and so increase the polarisability of the molecule and, in turn, increase the scattering effect.<sup>26</sup>

The roughened metal surface required for SERS may be introduced in several forms, with the most common including electrodes, metal thin films, and colloidal suspensions of metal nanoparticles.<sup>37</sup> Au and Ag are the most commonly used nanoparticles for Raman scattering as their surface plasmons lie in the visible region, enabling good enhancement factors to be obtained<sup>26</sup> and they are also relatively easy to prepare.<sup>37</sup>

#### *1.2.4 Surface enhanced resonance Raman scattering (SERRS)*

Surface enhanced resonance Raman scattering (SERRS) is a combination of RRS and SERS that incorporates surface enhancement with resonant chromophores to produce enhancement factors of up to  $10^{14}$ .<sup>37</sup> As with RRS, the laser excitation must coincide, or lie close to, the absorption maxima of the chromophore. With SERRS even greater enhancement is achieved if this frequency also coincides with the resonant frequency of the metal surface plasmons.<sup>26</sup>

The use of SERRS overcomes many limitations associated with Raman scattering, as the combination of enhancements increases the sensitivity which allows lower laser powers and shorter accumulation times to be used, which in turn can reduce sample degradation. As only Raman bands originating from the chromophore of the analyte are enhanced, selective detection of resonant analytes in the presence of non-resonant contaminants is afforded.<sup>36</sup> Any fluorescence interference is quenched by the metal surface, so Raman peaks will dominate and any fluorescence background is reduced, meaning both fluorescent and non-fluorescent dyes can be used as analytes.<sup>38</sup> Furthermore, by using a combination of dyes with varying resonant frequencies, multiple laser wavelengths can be used to achieve multiplexed detection. Its multiplexing capabilities and high sensitivity make SERRS a rival detection method to fluorescence-based methods.<sup>39</sup>

### *1.2.5 Raman imaging*

Raman spectral imaging (or mapping) is a method used for generating detailed chemical images from a samples Raman spectrum. It involves scanning a desired area by moving the laser across the surface, whilst collecting a spectrum at each pixel. False-colour images can then be generated for selected vibrations, showing the intensity distribution of the Raman band over the mapped area.

This technique shows the distribution of chemicals and other components within a sample, and has thus been applied to the analysis of cells,<sup>40</sup> tissue,<sup>41</sup> pharmaceutical drugs,<sup>42</sup> and even food.<sup>43</sup> As well as collecting spectral information in a 2D-setup (within the x-y plane), 3D images of samples can also be built by moving through the z-plane. 3D Raman mapping can be used to show the distribution of components within the volume of a sample and to study its architecture.<sup>44</sup>

Overall, Raman spectroscopy provides characteristic structural information from molecules and can be used in a label-free manner or can be coupled with nanoparticles and resonant dyes to increase the sensitivity of the technique. It can be used in many different applications, some of which are explored in this thesis.

## **1.3 An introduction to malaria**

Malaria is a mosquito-borne infectious disease that is widespread in many tropical and subtropical regions. A World Health Organisation report stated that in 2016 there were over 200 million cases of malaria infection worldwide, with an estimated 445 000 deaths.<sup>45</sup> A disproportionately high share of the global malaria burden is found in Sub-Saharan Africa with 90 % of all malaria cases and 91 % of all reported deaths occurring within these regions.<sup>45</sup> With these statistics, new techniques which could enhance or replace current methods to help reduce malaria incidence and mortality rates would be extremely advantageous.

### 1.3.1 *Malaria parasite*

The causative agent of malaria infection is a protozoan parasite of genus *Plasmodium*, which is transmitted to humans through the bites of infected female *Anopheles* mosquito vectors.<sup>46</sup> Four species, *P. falciparum*, *P. vivax*, *P. ovale*, and *P. malariae* are known to cause malaria in humans<sup>46</sup> along with the recently discovered *P. knowlesi*, a zoonotic form of human malaria.<sup>47</sup>

When a mosquito takes a blood meal, the parasite is injected into the human host's bloodstream with the mosquito saliva. An incubation period of between 7 - 30 days occurs before the first symptoms appear.<sup>48</sup> Shorter incubation periods are observed more frequently with *P. falciparum* infection, while longer periods with *P. malariae*.<sup>49</sup> *P. vivax* and *P. ovale* parasites can remain dormant in the host's liver for months or years, producing no physical symptoms of infection and may reactivate and cause disease long after the individual has left the malaria endemic region.<sup>46,49</sup>

Symptoms of infection typically include chills, fever, headaches, muscle aches and vomiting, these will be found in cases of uncomplicated malaria.<sup>48</sup> However, in extreme circumstances, infections can be complicated by serious organ failure or abnormalities in the patient's bloodstream, known as severe malaria and manifestations include cerebral malaria, severe anaemia, acute kidney failure, and hyperparasitemia.<sup>48,49</sup> All clinical symptoms, in both uncomplicated and severe malaria, are caused by the asexual erythrocytic stage parasites.<sup>50</sup>

### 1.3.2 Lifecycle of malaria parasite

Through the course of an infection, the malaria parasite passes through two distinct pathways known as the asexual (symptomatic) and sexual reproductive pathways (Figure 1.4).

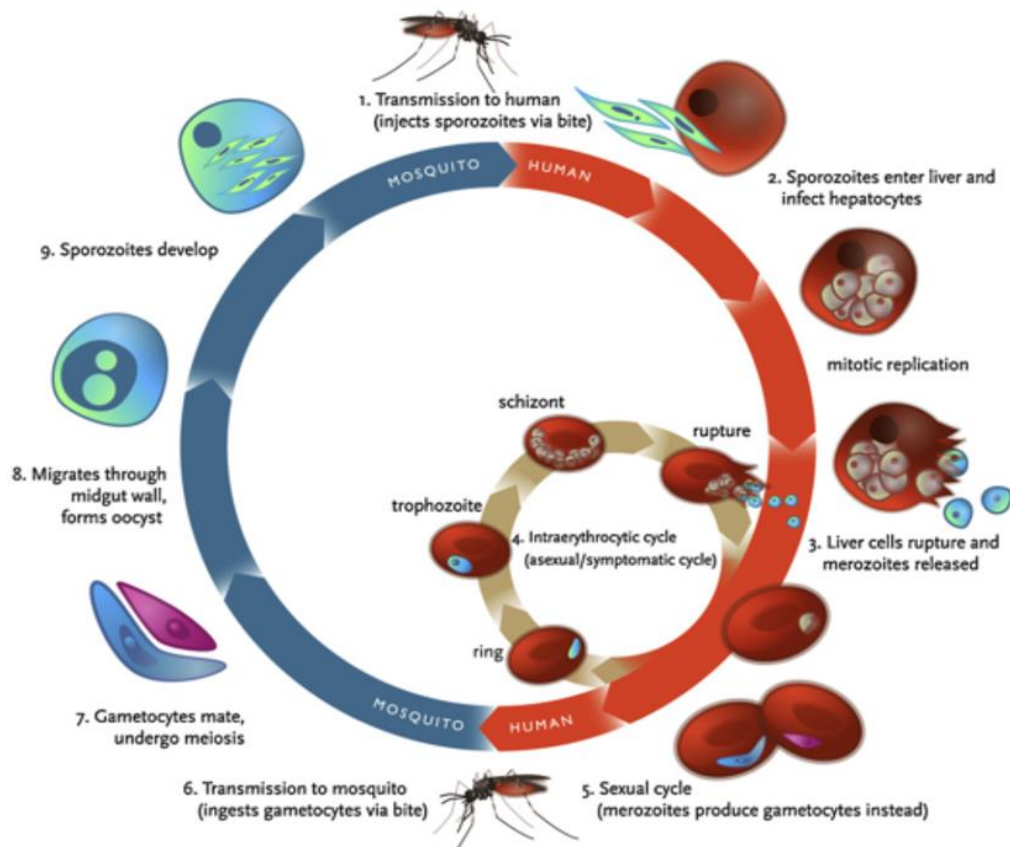


**Figure 1.4** Diagram illustrating the life-cycle of the malaria parasite. The right side (red) details the asexual cycle of the parasite. Here immature forms of the parasite, known as sporozoites, are injected into the human host's bloodstream where they quickly invade the liver cells and begin asexually replicating. After a period of ~7 – 30 days, the liver cells rupture, releasing thousands of merozoites into the bloodstream where they invade the red blood cells (RBCs). Over ~48 hours the parasite multiplies while progressing through three distinct phases (ring, trophozoite and schizont). At the end of the schizont stage, the RBCs rupture releasing more merozoites which can go on and infect more RBCs. Large numbers of RBCs bursting at the same time, correspond to the cycle of fever and chills in malaria. With each replication stage some of the merozoites will develop into gametocytes, instead of producing new merozoites (left side). These can then infect susceptible mosquitos, bringing the transmission cycle full circle.<sup>52</sup> Reprinted from International Journal of Antimicrobial Agents, **41**(4), Klein, E.Y., *Antimalarial drug resistance: a review of the biology and strategies to delay emergence and spread*, 311-317, Copyright 2013, with permission from Elsevier.

Following an infected mosquito bite, hundreds of sporozoites are released into the host's bloodstream where they quickly migrate to the liver and infect hepatocytes. Here they can remain dormant (*P. vivax* or *P. ovale*) or initiate development to

produce thousands of merozoites. This typically occurs over a 7 – 30 day period, after which the merozoites burst out of the liver and invade the red blood cells (RBCs) to initiate the intraerythrocytic phase. Within this phase the parasite begins replicating mitotically, moving through three set phases: ring, trophozoite, and schizont.<sup>46,51</sup> The schizonts then burst, often in close synchrony with other parasites,<sup>51</sup> producing the characteristic symptoms of high fever followed by chills and rigor. This cycle is repeated every ~48 hours in *falciparum*, *ovale*, or *vivax*; every ~72 hours in *malariae* infections; and ~24 hours in *knowlesi*.<sup>52</sup> Once free in the blood these new parasites can go on to infect further erythrocytes, resulting in exponential parasite proliferation.<sup>50</sup> However, after each replication some merozoites will instead develop into gametocytes, which can go on to infect susceptible mosquitos and continue the cycle.<sup>46</sup>

Identification of parasites within the host's blood is commonly used to diagnosis infection;<sup>53</sup> however, malaria-related biomarkers will also be present and these can be studied to improve current diagnostic tools.

### 1.3.3 Malaria biomarkers

A biomarker is a measurable 'biological marker' that correlates with a specific state, mainly those indicating the risk of contraction, presence or stage of a disease.<sup>54</sup> Biomarkers of various types can be used in research and clinical settings for disease monitoring and diagnosis, to guide treatment or to observe a therapeutic response. The ability to detect specific biomarkers of *Plasmodium* mediated infection, particularly at early stages, is crucial for reducing malaria morbidity and mortality. Several malaria-associated biomarkers have been utilised for disease identification and the most common are briefly described below.

#### 1.3.3.1 Hemozoin

During the intraerythrocytic phase the parasite catabolises up to 80 %<sup>55</sup> of the host's hemoglobin (Hb) within the parasitic food vacuole.<sup>56</sup> Degradation of Hb is believed to be a key source of amino acids for the parasite<sup>57</sup> and is also necessary to make room for itself as it multiplies within the cell.<sup>56</sup>



Along with amino acids the degradation of Hb also produces free heme moieties (ferrous [Fe<sup>II</sup>] protoporphyrin IX) that are toxic to the parasite. As the *Plasmodium* species lack the heme oxygenase enzyme that is responsible for the degradation of the heme moiety in vertebrates,<sup>58</sup> an alternative route for detoxification must be employed. The parasite achieves this by first oxidising heme to ferric [Fe<sup>III</sup>] protoporphyrin IX crystals (hematin). These single crystals then aggregate to form an insoluble complex known as hemozoin (Hz) or ‘malaria pigment’.<sup>58,59</sup>

Hz consists of an array of hematin units, linked into dimers through reciprocal iron-carboxylate bonds between central iron atoms of one heme and the propionic acid side chain of another. These dimers are then connected by hydrogen bonding to build a large regular network (Figure 1.5).<sup>52,58</sup> Aggregated Hz crystals are chemically inert and stored within the parasitic food vacuole as brick-like shaped deposits with maximum dimensions of 50 – 1000 nm.<sup>59</sup>

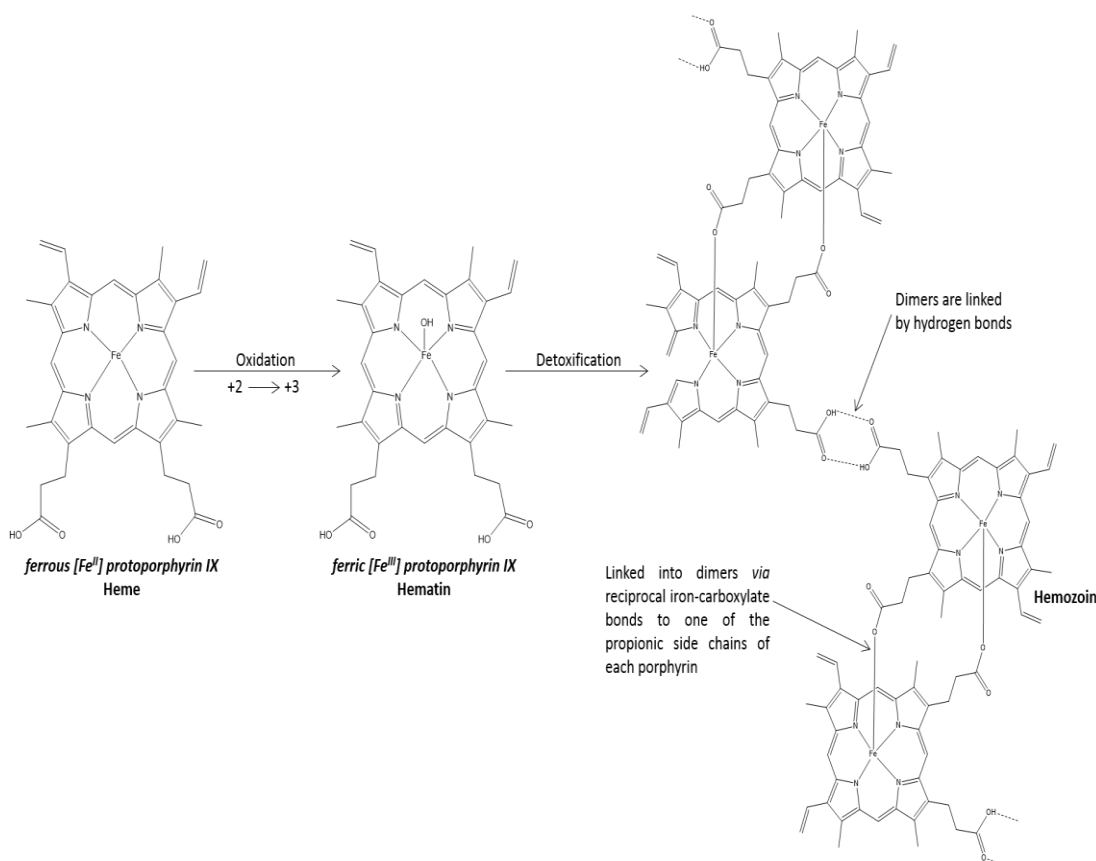


**Figure 1.5** Diagram illustrating the formation of hemozoin. Heme moiety is oxidised to form hematin molecules. These then form dimers with other hematin units *via* reciprocal iron-carboxylate bonds. Dimers are then linked *via* hydrogen bonds to form a large regular network. This forms what is known as the ‘malaria pigment’.

At the end of the intraerythrocytic cycle when the RBCs rupture, Hb is released into the bloodstream along with merozoites. These insoluble crystals are not degraded under physiological conditions and so circulate in the blood until they are eventually scavenged by macrophages in the liver and spleen.<sup>60,61</sup>

The majority of Hb degradation takes place during the trophozoite and schizont phases,<sup>58</sup> therefore the presence of Hb is most prominent within these later stages and has become a key biomarker for parasite identification.<sup>52</sup>

When carrying out *in vitro* malaria studies, a synthetic form of Hb known as  $\beta$ -hematin (or sHb) can be used as a substitute. This is chemically,<sup>55</sup> spectroscopically,<sup>62</sup> and crystallographically<sup>62</sup> identical to natural Hb and has the added advantage that it does not have to be isolated and extracted from the parasite.

#### 1.3.3.2 Histidine-rich protein-II

Histidine-rich protein-II (HRP-II) is regarded as a vital biomarker unique to *P. falciparum* and is produced by trophozoites and young gametocytes.<sup>52,63</sup> It is localised in the parasite cytoplasm and on the parasitised erythrocyte membrane. The concentration of HRP-II is known to increase as the parasite develops from the ring stage to the late trophozoite and can be detected at lower levels of parasitemia than panmalarial antigens such as aldolase.<sup>64</sup> This water-soluble protein can be detected in serum, plasma, cerebral-spinal fluid and urine samples.<sup>65</sup>

The function of HRP-II is not fully understood but reports have demonstrated that its main role is heme-binding and initiation of hemozoin formation within the malaria parasites.<sup>52</sup> HRP-II is a commonly targeted antigen for *P. falciparum* malaria diagnosis in immunochromatography-based rapid tests in a need for more objective and quantitative tools to replace traditional microscopy.

#### 1.3.3.3 Plasmodium lactate dehydrogenase

*Plasmodium* lactate dehydrogenase (*p*LDH) is an enzyme found in the glycolytic pathway of malaria parasites<sup>66</sup> and is produced by both asexual and sexual (gametocytes) stages.<sup>67</sup> Different isomers of *p*LDH for the *Plasmodium* spp. which infect humans exist and, when coupled with the HRP-II antigen in

immunochromatographic techniques, non-*falciparum* malaria infection can be distinguished from *P. falciparum*.<sup>53</sup>

#### 1.3.3.4 *Plasmodium aldolase*

Aldolase is a further key enzyme in the parasite glycolytic pathway<sup>52</sup> having a key role in the cleavage of fructose-1,6-bisphosphate into glyceraldehyde-3-phosphate and dihydroxyacetone phosphate.<sup>66</sup> It can be found localised in the parasite cytoplasm as an active and soluble form, or associated with the membrane fraction as an insoluble form.<sup>66</sup> This malaria antigen has also been investigated as a target in malaria diagnosis, mainly for non-*falciparum* species identification.<sup>53</sup>

#### 1.3.4 *Current malaria diagnosis techniques*

Prompt and accurate diagnosis of malaria is crucial for the effective treatment and management of infection. Diagnosis typically involves identification of the *Plasmodium* parasite or antigen / by-products in the patient's blood. However, the efficacy of detection is dependent on the method chosen.

##### 1.3.4.1 *Clinical diagnosis*

Clinical diagnosis is based on a patient's signs and symptoms, and on physical findings at an examination, which makes it a relatively inexpensive approach.<sup>68</sup> However, early symptoms are non-specific and variable and quite often overlap with other tropical diseases, which can lead to the indiscriminate use of antimalarials and compromise the quality of care for patients suffering from non-malarial fevers.<sup>69</sup>

Where possible, suspected cases of malaria should be confirmed by laboratory tests, as clinical diagnosis alone is unreliable. Two of the most highly utilised laboratory techniques are microscopic diagnosis<sup>70</sup> and rapid diagnostic tests (RDTs).<sup>53</sup>

##### 1.3.4.2 *Microscopic diagnosis*

The accepted 'gold standard' for malaria diagnosis is the preparation and microscopic examination of blood films (Figure 1.6), typically stained with Giemsa, to directly detect the parasite in the blood.<sup>53,70</sup> Microscopy offers many advantages including sensitivity of being able to typically detect ~100 parasites /  $\mu\text{L}$  blood,<sup>53</sup> the ability to

characterise parasites in terms of their species and of the circulating stage,<sup>71</sup> and, finally, the low cost involved in the method.<sup>67</sup>

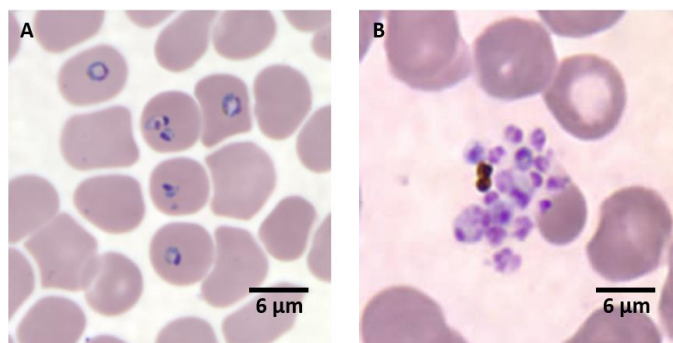


**Figure 1.6** Images of Giemsa stained blood smears. (A) *P. falciparum* rings in a thin blood smear. (B) *P. falciparum* ruptured schizont in a thin blood smear. *P. falciparum* schizonts are seldom observed in peripheral blood. Mature schizonts contain 8 to 24 merozoite, seen as dark pigment clumped in one mass.<sup>72</sup> Scale bar are shown on both images.

However, a disadvantage of microscopic diagnosis is that results can be subjective and depend heavily on the experience and training of the diagnostician, particularly at low levels of parasitemia.<sup>72</sup> It is also a labour-intensive technique with the time between specimen collection and results taking ~60 minutes, often with further delays in clinicians receiving microscopy results which can hinder treatment decisions.<sup>67</sup> More recently the advent of RDTs, which measure the presence of malaria parasite antigens, have expanded the range of diagnostic options.

#### 1.3.4.3 Rapid diagnostic tests

RDTs are based on the detection of malaria parasite specific antigens in peripheral blood, using lateral flow immunochromatographic techniques.<sup>53</sup> They employ a prefabricated strip of carrier material bearing monoclonal antibodies directed against the target parasite antigen (Figure 1.7). Their use is intended to allow simple and swift diagnosis, particularly in areas where standard laboratory diagnosis is limited or not possible. Many RDT kits are commercially available, although they have varying degrees of performance quality.<sup>73</sup>

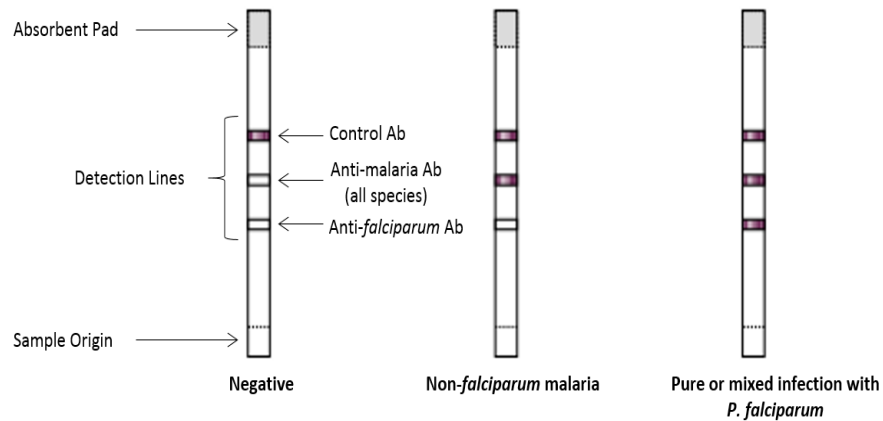


**Figure 1.7** Example results and interpretation from a typical commercial RDT. Also labelled are the basic component parts of a dipstick RDT.<sup>67</sup> Copyright (2018) World Health Organisation.

RDTs are simple and quick to employ with a typical test taking 15 – 20 minutes to run.<sup>68</sup> Unlike traditional light microscopy techniques, they do not require a highly skilled specialist to run and it has been reported that interpretation of results varies little among users.<sup>53</sup> As RDTs detect circulating antigens, it is possible for them to detect *P. falciparum* infection even when the parasites are sequestered in the deep vascular compartment and so undetectable by microscopic examination of a peripheral blood smear.<sup>67</sup> However, when compared to microscopy detection thresholds of 5 – 10 parasites /  $\mu\text{L}$  blood, limits are slightly higher for RDTs at 40 – 100 parasites /  $\mu\text{L}$  blood.<sup>53</sup> Many are also non-quantitative devices, only providing visual indication of infection, and so do not provide information of the possible prognostic importance. These immunochromatographic techniques also suffer from the fact that, as of yet, they cannot differentiate between non-*falciparum* parasite infections.<sup>67</sup>

With further work to improve their disadvantages, RDTs offer a practical chance of moving malaria diagnosis away from time-consuming laboratory microscopy and nearer to the patient for quicker and more specific treatment choices.

### 1.3.5 Applications of Raman in malaria diagnosis

Raman spectroscopy has been extensively used for the identification of malaria infection, most commonly *via* the detection of the 'malaria pigment', H<sub>z</sub>. It has been widely reported by groups including Frosch *et al.*<sup>55</sup> and Wood *et al.*<sup>74</sup> that the choice of Raman excitation wavelength is key to gaining selective resonant enhancement of Hb and H<sub>z</sub> porphyrin ring bands over other non-resonant cellular components within blood, plasma and tissue samples.

In 1999, Ong *et al.* used resonance Raman to study erythrocytes infected with *P. berghei*, a rodent malaria parasite.<sup>75</sup> From the Raman spectra they were able to easily determine if erythrocytes were infected by studying the appearance of multiple heme-resonance enhanced bands, including the 754 cm<sup>-1</sup> porphyrin band. Wood *et al.*<sup>76</sup> reported that by exploiting the resonance Raman characteristics of H<sub>z</sub>, coupled with partial dark field microscopy, there was potential to determine targets within *P. falciparum* infected erythrocytes as the H<sub>z</sub> deposits within the parasites 'light up' under a dark field effect. Rapid confocal Raman imaging then allowed the presence of H<sub>z</sub> to be confirmed, which in turn confirmed the presence of malaria infection.<sup>76</sup> More recently, Hobro *et al.* applied resonance Raman imaging to study the progression of *P. yoelii* non-lethal parasite infection *via* blood and plasma samples.<sup>77</sup> They showed, with the aid of chemometrics, that within infected blood samples, changes associated with a loss of Hb and an increase in H<sub>z</sub> could be detected after four days of infection. However, when plasma samples were analysed, it was shown that H<sub>z</sub> could be detected one day post-infection due to a reduced heme background.

These studies highlight how valuable Raman spectroscopic techniques are for the study of biological matrices within malarial infection. Extensive research has been carried out to understand the Raman spectral profile of H<sub>z</sub> and its detection within erythrocytes using both rodent<sup>75,77,78</sup> and human malaria parasite models.<sup>56,74,76,79</sup>

However, to date, little work has been done to discover if Raman spectroscopy can be utilised to understand and diagnose tissue burden within malaria parasite infected tissue or if SERRS can be coupled with RDT's to improve their sensitivity in detecting

malaria specific biomarkers. These possibilities will be explored further within this thesis.

## 2 Project aims

---

This thesis investigates the application of Raman spectroscopic techniques for the detection of malaria parasite infection and can be separated into two main sections. The initial aim was to investigate the application of label-free Raman imaging to differentiate malaria parasite infected from non-infected tissue. Malaria parasite sequestration within the vascular endothelium of organs is largely responsible for the symptoms and severity of infection. Therefore, Raman imaging coupled with chemometric analysis was applied to mouse spleen tissue sections, both infected and non-infected, to determine if any biological alterations associated with infection could be detected and linked to tissue burden. Following this, the ability of Raman spectroscopy to be applied *in-vivo* to non-invasively detect tissue burden was studied. A portable Raman system was used to interrogate the spleen and liver of mice that had been injected with infected and non-infected red blood cells.

The second objective was to investigate the coupling of rapid diagnostic paper-based devices with SERRS for the sensitive detection of the *P. falciparum* specific biomarker, HRP-II. Quantification of the target antigen *via* SERRS detection was converted to parasite densities of infection and compared to the current 'gold standard' detection of light microscopy analysis of blood smears. Colourimetric analysis of the device test spots was also carried out determine whether SERRS detection could improve the conventional colourimetric method for analysing these paper-based diagnostic tests. Finally, the ability of a 3D-paper-based diagnostic device and SERRS to detect HRP-II in a biologically relevant matrix was tested.



## 3 Label-free Raman imaging of malaria parasite infected tissue

---

### 3.1 Introduction

As reported in section 1.3, at the end of the parasite erythrocytic cycle, RBCs rupture, releasing Hz and parasites into the bloodstream. However, under physiological conditions, the Hz is not degraded and circulates in the bloodstream until it is digested by macrophages present within specific organs.<sup>61</sup> The spleen is the primary organ involved in the development of an immune response<sup>80</sup> during the erythrocytic stage of infection, along with the elimination of parasitised RBCs and Hz.<sup>81,82</sup> However, *P. falciparum* parasites have developed mechanisms to avoid clearance which can lead to diagnostic difficulties.

#### 3.1.1 Parasite sequestration

Erythrocytes infected with mature forms of the *P. falciparum* malaria parasite are known to cytoadhere to the vascular endothelium of several organs, including the brain, liver, and spleen to avoid clearance from the bloodstream.<sup>83</sup> Proteins of the *P. falciparum* erythrocyte membrane protein 1 (*PfEMP1*) family mediate this adhesion through specific binding to multiple endothelial cell receptors.<sup>84</sup> Binding to endothelium results in widespread sequestration of infected RBCs and therefore their reduced splenic clearance (Figure 3.1). Also because they are sequestered in the

deep microvasculature, diagnosis is more challenging as they are not seen in the peripheral blood.<sup>83</sup>

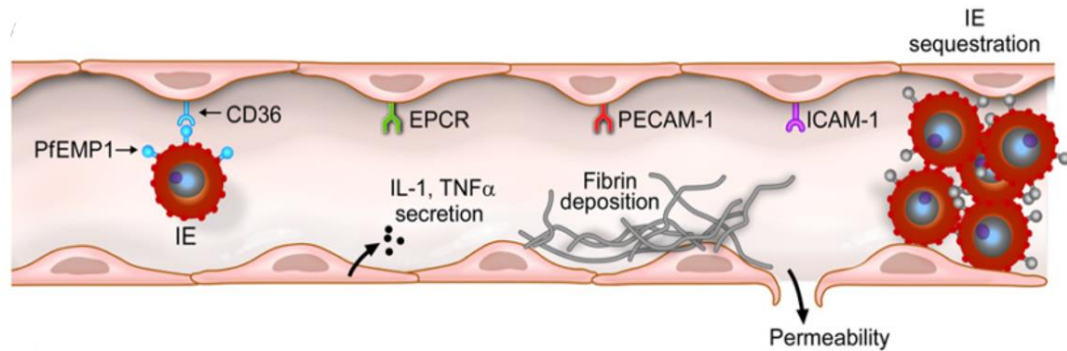


**Figure 3.1** Schematic of a typical microvessel found in multiple organs and tissues in malaria parasite infected patients. *P. falciparum* parasites sequester in microvessels to avoid splenic clearance from the bloodstream. The parasite on the left is expressing a PfEMP1 variant on the infected erythrocyte (IE) surface that binds CD36 on endothelial cells. In addition to CD36, endothelial cells may also express EPCR, PECAM-1, and ICAM-1. Infected erythrocyte binding to these different receptors is encoded by specific PfEMP1 domain cassettes. Activation of the endothelium by developing parasites and downstream events such as secretion of proinflammatory cytokines (IL-1 and TNF $\alpha$ ), deposition of fibrin, and loss of barrier integrity, result in microvascular inflammation, obstruction, and perivascular leakage.<sup>85</sup> Reprinted with permission from Aird, W., *et al.*, *Plasmodium falciparum* picks (on) EPCR. *Blood*, 2014, **123**(2), 163-168. Copyright (2018) American Society of Hematology.

PfEMP1 – *P. falciparum* erythrocyte membrane protein 1; CD36 – platelet glycoprotein 4; EPCR – endothelial protein C receptor; PECAM-1 – platelet endothelial cell adhesion molecule-1; ICAM-1 – intercellular adhesion molecule-1; IL-1 – interleukin 1; TNF $\alpha$  – tumor necrosis factor alpha.

Sequestration of parasite infected RBCs is largely responsible for the severity and symptoms of infection<sup>83,85</sup> and is associated with a number of features of severe malaria pathology such as cerebral malaria, severe anaemia, and hyperlactataemia.<sup>86</sup> Cerebral malaria is a major complication of *P. falciparum* infections<sup>87,88</sup> and is linked with a high risk of death, particularly in young children. The sequestration of parasitised RBCs to vascular endothelium can cause microvascular obstruction and is considered to be a major feature leading to cerebral malaria related pathology.<sup>86,89</sup> Studies carried out on brain tissue, post-mortem, have shown numerous sequestered parasitised RBCs within the cerebral microvasculature,<sup>90,91</sup> however, there is a difficulty in assessing the presence of parasites within the tissue during the progression of the disease. Therefore, a technique, such as Raman spectroscopy,

which could non-invasively detect tissue burden would be a great step forward in diagnosing cerebral malaria at an earlier stage, so treatment plans could be implemented.

The rodent parasite, *Plasmodium berghei* (*P. berghei*), is one of the most widely employed models in malaria research to understand infection in humans.<sup>85</sup> RBCs infected with mature schizont stage *P. berghei* ANKA parasites, sequester effectively in a large number of mice organs, such as lungs, spleen, liver, and brain.<sup>85,92</sup> This accumulation has been visually highlighted by Franke-Fayard *et al.*<sup>89</sup> who reported a system for the real-time *in vivo* imaging of sequestration (Figure 3.2). Through modifying the parasite genome with GFP-luciferase, only the schizont stage was made visible when bioluminescence signals were detected which showed this mature stage of the parasite was specifically localised in lungs, the spleen and adipose tissue.<sup>89</sup>

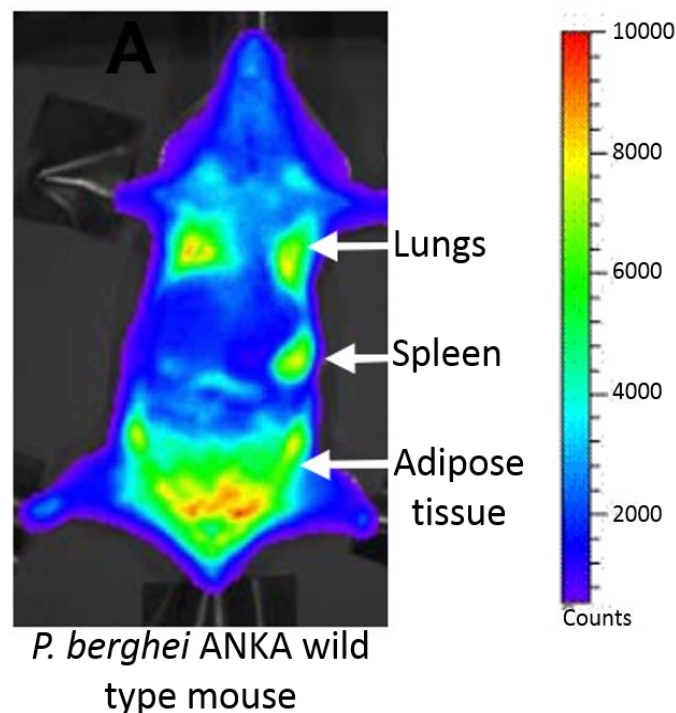


**Figure 3.2** Imaging of transgenic *P. berghei* ANKA parasites *in vivo*. CD36-mediated sequestration of schizonts were visible in the lungs, spleen, and adipose tissue of a wild type mouse.<sup>90</sup> Reprinted with permission from Franke-Fayard, B., *et al.*, *Murine malaria parasite sequestration: CD36 is the major receptor, but cerebral pathology is unlinked to sequestration*. *Proceedings of the National Academy of Sciences*, 2005, **102**(32), 11468 – 11473. Copyright (2018) National Academy of Sciences.

The absence of *P. berghei* schizonts in peripheral blood has also been observed in mice and rat models.<sup>92</sup> This *P. berghei* ANKA infection in mice resembles *P. falciparum* infection of humans in that parasite sequestration and tissue accumulation does occur and the process is limited to only mature parasite stages.<sup>85</sup> As a result of these characteristics with spleen recognised as a key tissue for sequestration of this parasite, *P. berghei* ANKA infected spleen was chosen to carry out proof-of-concept work on the ability of Raman spectroscopic imaging to identify infected tissue *via* differentiation from non-infected controls.

### *3.1.2 Raman analysis of biological tissue samples*

The coupling of Raman spectroscopy with microscopy within biology is becoming increasingly popular as it can provide both biochemical and structural information, along with direct visualisation of the sample.<sup>31</sup> Along with single point spectra, Raman microspectroscopy can also produce highly informative Raman images of selected sampling areas non-invasively, non-destructively, and with high molecular specificity.<sup>93</sup> These studies can accumulate large, information rich spectral data sets and to effectively extract the relevant underlying chemical and compositional data, multivariate analysis techniques can be applied allowing conclusions to be drawn with statistical significance.<sup>94</sup>

During the pathogenesis of disease, biological alterations occur, that lead to changes in the biochemical composition of affected tissues. These changes in structure, concentration, and composition of biomolecules can be reflected in the Raman spectra of tissue samples. Indeed, Raman spectroscopy has been used to study the subtle molecular changes in tissue samples associated with many diseases. Kochan *et al.*<sup>95</sup> utilised Raman microspectroscopic imaging to investigate the pathological changes in the liver induced by diabetes and atherosclerosis.

Their work focussed heavily on the changes in content and distribution of lipids within the mouse model livers. By creating false colour Raman images (Figure 3.3) Kochan *et al.* visually highlighted that lipid content was highest in diabetic mice livers, relatively high in atherosclerotic mice, whereas in control mice lipid-rich areas were comparatively small. This study showed Raman imaging as a powerful tool for accurate chemical analysis of tissue sections.

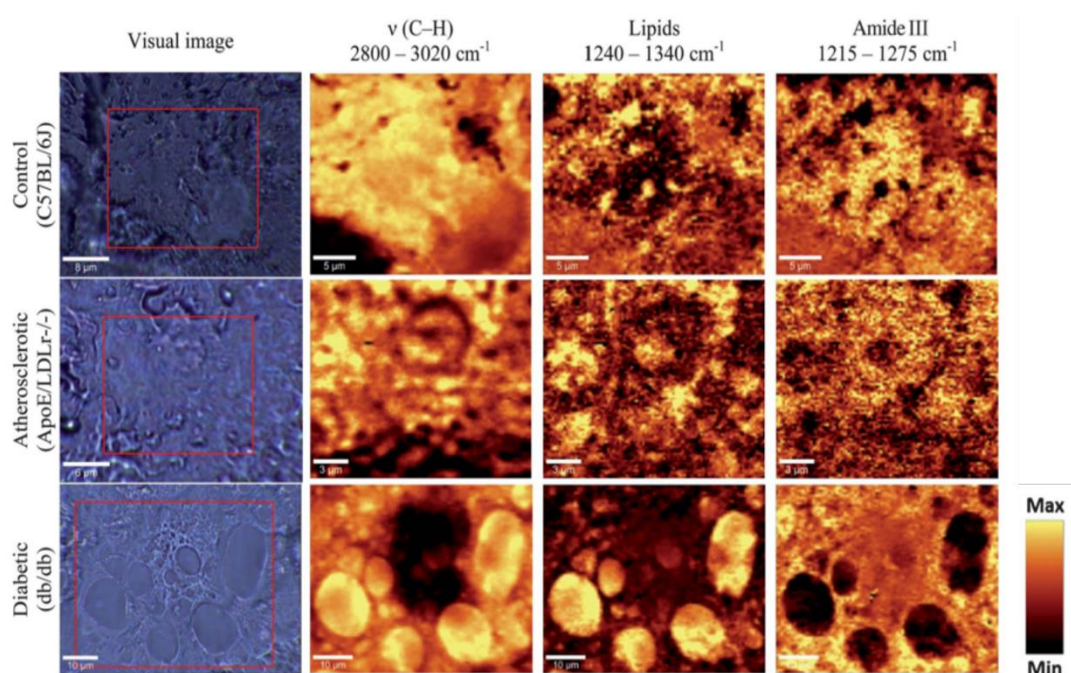


**Figure 3.3** Raman maps providing an accurate insight into the biochemical composition of mice livers analysed with this vibrational technique. White light images of the cross-section of liver tissues taken from control (top), atherosclerotic (middle), and diabetic (bottom) mice with interrogated areas outlined in red. False colour Raman maps of lipid and protein distributions obtained by integration of marker bands in regions of  $2800 - 3020 \text{ cm}^{-1}$  (C-H),  $1240 - 1340 \text{ cm}^{-1}$  (lipids), and  $1215 - 1275 \text{ cm}^{-1}$  (amide III band of proteins). Scale bars also shown.<sup>96</sup> Reproduced from Kochan, K., *et al. Pathological changes in the biochemical profile of the liver in atherosclerosis and diabetes assessed by Raman spectroscopy*, *Analyst*, 2013, **138**, 3885-3890, with permission of The Royal Society of Chemistry.

Raman spectroscopic imaging has also been proven successful in differentiating dysplastic tissue from normal gastric mucosa tissue,<sup>96</sup> in the differential diagnosis of lung malformations,<sup>97</sup> and in accurately classifying breast lesions from samples of benign and malignant human breast tissue.<sup>98</sup>

SERS studies of *ex-vivo* tissue sections have also been investigated using both Au<sup>99</sup> and Ag<sup>100,101</sup> nanoparticles incubated on top of the tissue sections, to differentiate between a variety of diseased and healthy samples. Schlucker and co-workers<sup>102</sup> also showed *in situ* detection of antigens in tissue sections *via* SERS from Au nanoparticles with an aromatic Raman label covalently linked to the antigen-specific antibody.

Traditional Raman spectroscopy has generally been restricted to probing surface or near-surface areas of biological tissues with penetration depths of only several hundred microns into tissue, which limits its ability for application to *in vivo* disease detection.<sup>103</sup> However, with the development of spatially offset Raman spectroscopy (SORS), accurate analysis through millimetres of material, when obscuring barriers such as skin are present, is now achievable.<sup>104,105</sup> Along with the development of handheld portable SORS instruments, that have also been shown to be able to detect through millimetres of obscuring barriers,<sup>106</sup> the ability to gain biochemical information to detect diseased tissue *in vivo* has become a real possibility.

### 3.1.3 Choice of Raman excitation wavelength

For biological tissues, a near infra-red (NIR) laser excitation is commonly used as the optical window (700 – 900 nm) for these specimens exists within the NIR region, where the absorption of light within tissue is minimal.<sup>107,108</sup> Within this optical window, tissue is relatively transparent to light, and measurements in this region minimise contributions from tissue autofluorescence.<sup>109</sup> Although scattering efficiency is higher at lower wavelengths, such as 532 nm, resulting in the use of shorter integration times and lower laser powers, significantly less tissue damage occurs when NIR lasers are employed.<sup>107</sup> As a consequence of this, a 785 nm excitation laser was used to interrogate both the malaria parasite infected spleen tissue and the uninfected samples. As some substrates, particularly glass, emit a large fluorescent background signal in the NIR region,<sup>107</sup> spleen tissue sections were placed on Raman-grade calcium fluoride (CaF<sub>2</sub>) slides.

It is well documented that resonance Raman enhancements of the porphyrin rings of Hb can be gained through excitation in the regions of the Soret absorption band

(near-UV ~400 – 436 nm) or the Q-bands (visible region ~490 – 650 nm).<sup>110–113</sup> As the malaria pigment, Hz, shares the same porphyrin core as Hb, resonance enhancement of this compound can also be achieved by selecting the correct laser wavelength. Within malaria research, it has been widely reported by groups including Frosch *et al.*<sup>55</sup> and Wood *et al.*<sup>74</sup> that the choice of Raman excitation wavelength is key to gaining selective enhancement of Hb and Hz bands over other non-resonant cellular components. Wood *et al.*<sup>76</sup> reported that by exploiting the resonance Raman characteristics of Hz through using a 532 nm excitation source, coupled with partial dark-field microscopy, there was potential to detect low-pigmented phases of the malaria parasite's life-cycle within infected erythrocytes. Further on from this, Hobro *et al.*<sup>77</sup> applied resonance Raman imaging, with a 532 nm laser wavelength, to study the progression of malaria infection *via* blood and plasma samples. Their work showed that within infected blood samples, changes associated with a loss of Hb and an increase in Hz could be detected after four days of infection. They also showed the ability to detect Hz in plasma after only one day post *Plasmodium* infection. This potential for earlier diagnosis was attributed to the reduced heme-background associated with the plasma samples. These studies highlight how valuable Raman spectroscopic techniques are for the study of biological matrices with malaria infection. Therefore, a 532 nm laser excitation was also chosen to study the spleen tissue sections, on glass slides, to gain resonance Raman enhancement of any heme-based (Hb &/or Hz) components within the samples.

In this work, two laser excitation wavelengths were used to gain Raman (785 nm) and resonance Raman (532 nm) information to study the subtle changes in the biochemical composition of mouse spleen tissue sections following infection with the rodent malaria parasite, *P. berghei*, to determine if Raman spectroscopy could be utilised as a tool for detecting tissue burden.

## 3.2 Results and discussion

Spleen tissue samples were obtained from two female BALB/c mice infected with asynchronous *P. berghei* ANKA (euthanised when peripheral blood parasitemia reached 5 %), along with two female control uninfected mice. At this level, although high, the infection is asymptomatic in BALB/c mice. Ten tissue sections were taken from the infected spleens, along with a further ten from the uninfected spleens (at a thickness of 10  $\mu\text{m}$ ) and placed on poly-L-lysine glass slides for analysis at 532 nm. For analysis with a 785 nm laser excitation, four infected and four uninfected 10  $\mu\text{m}$  spleen tissue sections were placed on poly-L-lysine coated Raman-grade  $\text{CaF}_2$  slides. These  $\text{CaF}_2$  slides were used for analysis at 785 nm as the standard glass slides gave a large fluorescence background that interfered with any Raman peaks present. Tissue-Tek O.C.T compound,<sup>114</sup> a formulation of water-soluble glycols and resins, was used as a tissue freezing medium to preserve the whole spleen structure for cryosectioning. This was also used to aid the attachment of spleen sections to the glass and  $\text{CaF}_2$  slides. Prior to Raman analysis the sample slides were washed once with PBS (10 mM, pH 7.2), followed by a rinse with  $\text{dH}_2\text{O}$  to remove the Tissue-Tek O.C.T. This left no residue on the slides and the polycationic nature of poly-L-lysine allowed interactions with the anionic sites of the tissue sections,<sup>115</sup> resulting in strong adhesion of the samples even after the freezing medium had been removed. This method of tissue preparation was chosen over traditional formaldehyde fixation as formaldehyde fixation can cause change to the biochemistry of the tissue as it works by cross-linking chemical groups such as amines, and therefore it can cause significant changes to the Raman spectrum.<sup>116</sup>

Once washed, Raman spectroscopic imaging was performed using a Raman spectrometer equipped with a 532 nm (resonant) and 785 nm (non-resonant) laser excitation to study the changes in the biochemical composition of the mice spleen tissue sections following infection with *P. berghei*. Firstly, the Raman spectra of infected samples were compared with non-infected samples to detect any changes in the Raman spectral signature associated with infection. The multivariate



chemometric analysis technique, principal component analysis (PCA) was then applied to decompose the spectral data into components and attempt to identify subtle changes to biological groups within tissue sections that could differentiate infected tissue burden from non-infected samples. A synthetic form of hemozoin,  $\beta$ -hematin, was synthesised to be used as a reference spectrum in the analysis of tissue imaging results. This was synthesised using an acid catalysed dehydration of hematin method adapted from Egan *et al.*<sup>117</sup> and Egan *et al.*<sup>118</sup> Characterisation of the  $\beta$ -hematin crystals was carried out using IR, Raman, and UV-visible spectroscopic techniques (Appendix I).  $\beta$ -hematin will be referred to as sHz in the following results and discussion section.

### 3.2.1 2D Raman imaging

Multiple areas of infected and non-infected tissue sections were mapped to gain large, information rich data sets. Firstly, an infected and non-infected (control) map were selected, for both wavelengths, to study the resonant (Figure 3.4) and non-resonant (Figure 3.5) spectral features of the tissue and changes in relative peak intensity were investigated using spectra subtraction and intensity ratio maps. At each wavelength, both tissue types showed a very similar spectral profile, highlighting that the biochemical compositions were closely linked (Figure 3.4(A) & Figure 3.5(A)). Tentative peak assignments of the Raman bands for the data collected with a 532 nm and 785 nm excitation are listed in

Table 3.1 and Table 3.2, respectively. Similar Raman peaks were recorded using the 532 nm and 785 nm laser excitation ( $\sim 1130$ , 1338, 1585, and 1618  $\text{cm}^{-1}$ ) for both the control and infected spleen tissue. However, the relative Raman peak intensity for the  $\sim 1130 \text{ cm}^{-1}$  and  $\sim 1585 \text{ cm}^{-1}$  peaks were much greater when the 532 nm laser was used. Both peaks can be assigned to vibrations from Hb ( $1130 \text{ cm}^{-1} - \nu_5$  and  $1585 \text{ cm}^{-1} - \nu_{37}$ )<sup>112,119</sup>, as well as smaller contributions from some other proteins<sup>116</sup> and lipids.<sup>97</sup> Resonance Raman contributions from the Hb vibrations can be used to explain the observed increase in peak intensity from the tissue analysed with a 532 nm laser, compared to the non-resonant 785 nm spectra.

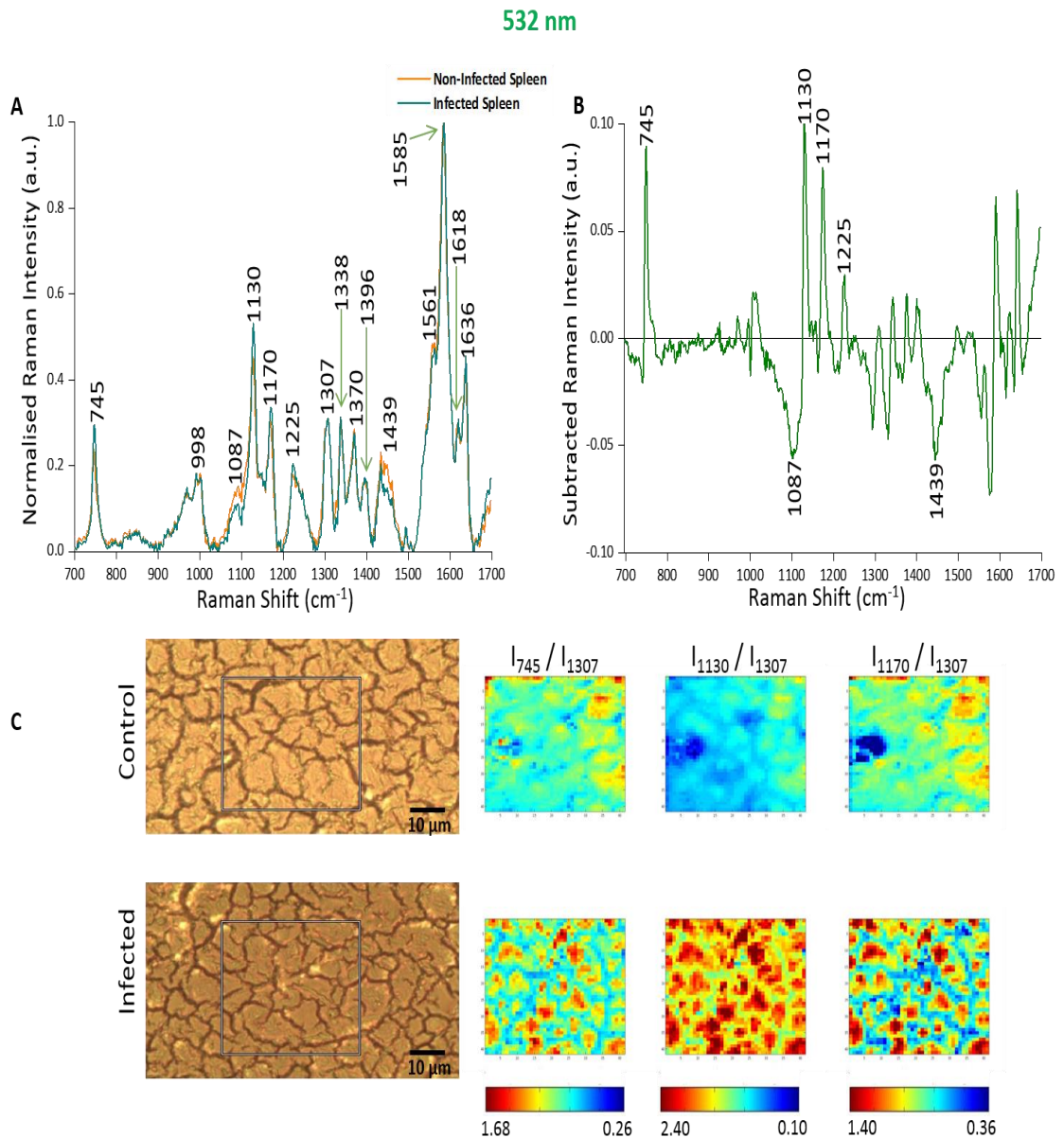


**Figure 3.4** Analysis of Raman peak intensity for control and *P. berghei*-infected tissue sections mapped at 532 nm. (A) Averaged, normalised spectra from a mapped area of control and infected tissue (41 x 41  $\mu\text{m}$ , step size 1  $\mu\text{m}$ ). Spectra were then normalised against the peak at 1585  $\text{cm}^{-1}$ . (B) Subtracted Raman spectrum. The average, normalised control spectrum was subtracted from the average, normalised infected spectrum, both shown in (A), to highlight any potential biological components that were being altered within the malaria infected tissue. (C) Image shows white light images of both tissue sections, with the grey box indicating the area that was mapped, along with peak intensity ratio maps for selected Raman peaks. Intensity ratio maps were created using the peak intensities for: 745  $\text{cm}^{-1}$ , 1130  $\text{cm}^{-1}$ , 1170  $\text{cm}^{-1}$ , and 1307  $\text{cm}^{-1}$  ( $I_{745}/I_{1307}$ ;  $I_{1130}/I_{1307}$ ;  $I_{1170}/I_{1307}$ ). These ratio maps visually show relative changes in the intensity of these Raman peaks within the area of *P. berghei*-infected tissue that was mapped compared to the uninfected area. These maps suggest an increase or alteration to some key biological components within the infected tissue including, multiple hemoglobin vibrations,<sup>113, 120</sup> lipids,<sup>98</sup> and proteins.<sup>117</sup>

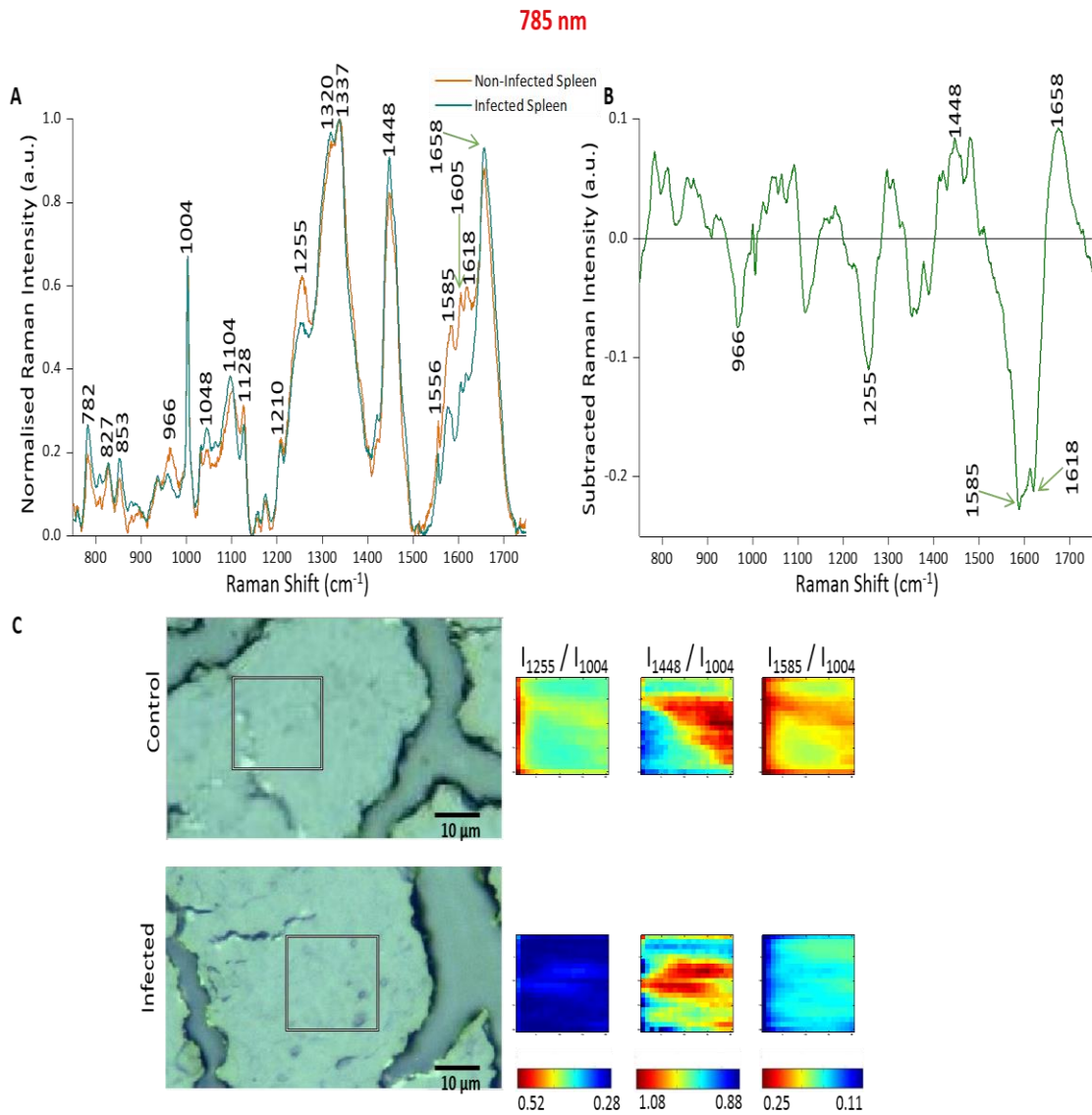


**Figure 3.5** Analysis of Raman peak intensity for control and *P. berghei*-infected tissue sections mapped at 785 nm. (A) Averaged, normalised spectra from a mapped area of control and infected tissue (20 x 20  $\mu\text{m}$ , step size 1  $\mu\text{m}$ ). Spectra were then normalised against the peak at 1337  $\text{cm}^{-1}$ . (B) Subtracted Raman spectrum. The average, normalised control spectrum was subtracted from the average, normalised infected spectrum, both shown in (A), to highlight any potential biological components that were being altered within the malaria infected tissue. (C) Image shows white light images of both tissue sections, with the grey box indicating the area that was mapped, along with peak intensity ratio maps for selected Raman peaks. Intensity ratio maps were created using the peak intensities for: 1255  $\text{cm}^{-1}$ , 1448  $\text{cm}^{-1}$ , 1585  $\text{cm}^{-1}$ , and 1004  $\text{cm}^{-1}$  ( $I_{1255}/I_{1004}$ ;  $I_{1448}/I_{1004}$ ;  $I_{1585}/I_{1004}$ ). These ratio maps visually show relative changes in the intensity of these Raman peaks within the area of *P. berghei*-infected tissue that was mapped compared to the uninfected area. These maps suggest alterations and possible decreases in intensity to some key biological components within the infected tissue including, multiple protein vibrations, including Amide III,<sup>97</sup> and lipids.<sup>98</sup>

**Table 3.1** Tentative peak assignments for the main peaks observed in the spectral profile for both non-infected and *P. berghei* infected spleen samples, Raman imaged with a 532 nm laser excitation source.

| 532 nm laser excitation   |   |
|---------------------------|---|
| Raman                     |   |
| shift (cm <sup>-1</sup> ) | Assignment <sup>a</sup>   |
| 745                       | $\nu_{15}$ Hb [ $\nu$ (pyr breathing)]  |
| 998                       | $\nu_{45}$ Hb [ $\nu$ (CC)asym], Proteins (Phe)   |
| 1087                      | DNA/nucleic acids [ $\nu_s$ (PO <sub>2</sub> <sup>-</sup> ), $\nu$ (CC)], Hb              |
| 1130                      | $\nu_5$ Hb [ $\delta$ (=CH <sub>2</sub> ) <sub>4</sub> ], Lipids (C=C backbone stretches) |
| 1170                      | $\nu_{30}$ Hb [ $\nu$ (pyr half-ring) <sub>asym</sub> ], Proteins (Tyr)                   |
| 1225                      | $\nu_{13}/\nu_{42}$ Hb [ $\delta$ (CH)], Proteins (amide III)                             |
| 1307                      | $\nu_{21}$ Hb [ $\delta$ (CH)], Lipids (CH <sub>2</sub> deformation band)                 |
| 1338                      | $\nu_{41}$ Hb [ $\nu$ (pyr half-ring) <sub>sym</sub> ], Nucleic acid modes                |
| 1370                      | $\nu_4$ Hb [ $\nu$ (pyr half-ring) <sub>sym</sub> ]                                       |
| 1396                      | $\nu_{20}$ Hb [ $\nu$ (pyr quarter-ring)], CH <sub>2</sub> deformation                    |
| 1439                      | Lipids [ $\delta$ (CH <sub>2</sub> )]   |
| 1561                      | $\nu_{11}$ Hb [ $\nu$ (CC)]   |
| 1585                      | $\nu_{37}$ Hb [ $\nu$ (CC) <sub>asym</sub> ]  |
| 1618                      | $\nu_{19}$ Hb [ $\nu$ (CC) <sub>asym</sub> ], Proteins (Tyr, Trp C=C stretches)           |
| 1636                      | $\nu_{10}$ Hb [ $\nu$ (CC) <sub>asym</sub> ], Proteins (amide I)                          |

<sup>a</sup> Abbreviations:  $\nu$  – stretch vibration;  $\delta$  – in-plane bending vibration; sym – symmetric; asym – asymmetric; Hb – hemoglobin; Phe – phenylalanine; Tyr – tyrosine; Trp - tryptophan. Assignments from ref. <sup>93,95,119</sup>

When comparing the averaged, normalised spectra, differences in the relative Raman peak intensities for infected vs. control tissue were observed for both wavelengths. These were highlighted through subtraction of the average, normalised control spectra from the infected (Figure 3.4(B) and Figure 3.5(B)). With the resonant Raman tissue data, subtraction emphasised some peaks that appeared to increase (~745, 1130, 1170 and 1225 cm<sup>-1</sup>) and decrease (~1087 and 1439 cm<sup>-1</sup>) in Raman signal intensity within the *P. berghei* infected tissue compared with the non-infected, control. This change in relative peak intensity suggested an alteration in the biological

composition of the spleen at this level of infection, characterised by changes in level and/or composition of the biological species assigned to these Raman signals.

**Table 3.2** Tentative peak assignments for the main peaks observed in the spectral profile for both non-infected and *P. berghei* infected spleen samples, Raman imaged with a 785 nm laser excitation source.

| <b>785 nm laser excitation</b>  |  |
|---------------------------------|--|
| Raman shift (cm <sup>-1</sup> ) | Assignment <sup>a</sup>  |
| 966                             | Lipids   |
| 1004                            | Proteins (Phe sym ring breathing mode), Hb   |
| 1048                            | Glycogen, Protein (C–O & C–N stretching)   |
| 1104                            | Proteins (Phe)   |
| 1128                            | Phospholipids, $\nu_5$ Hb [ $\delta(=CH_2)_4$ ]  |
| 1210                            | Proteins (Trp, Phe)  |
| 1255                            | Proteins (amide III), Lipids (CH <sub>2</sub> in-plane deformation)  |
| 1320                            | Phospholipids, Nucleic acids (CH <sub>3</sub> CH <sub>2</sub> twisting modes)                              |
| 1337                            | Proteins (amide III), CH <sub>2</sub> /CH <sub>3</sub> wagging, collagens & lipids                         |
| 1448                            | Proteins ( $\delta(CH_2)$ , $\delta(CH_3)$ , collagen), Lipids ( $\delta(CH_2)$ scissoring, phospholipids) |
| 1556                            | Proteins (amide II, Trp), Hb   |
| 1585                            | Proteins (Phe, $\delta(C=C)$ ), $\nu_{37}$ Hb [ $\nu(CC)_{asym}$ ]   |
| 1605                            | Proteins (Phe, Tyr)  |
| 1618                            | Proteins ( $\nu(C=C)$ , Trp), $\nu_{19}$ Hb [ $\nu(CC)_{asym}$ ]   |
| 1658                            | Proteins ( $\nu(C=O)$ amide I, $\alpha$ -helix, collagen, elastin)   |

<sup>a</sup> Abbreviations:  $\nu$  – stretch vibration;  $\delta$  – in-plane bending vibration; sym – symmetric; asym – asymmetric; Hb – hemoglobin; Phe – phenylalanine; Tyr – tyrosine; Trp – tryptophan. Assignments from ref. <sup>93,96,97,116</sup>

When studying the subtraction of the control spectrum from the infected, using a 785 nm laser, a similar trend of peaks appearing to increase ( $\sim 1448$  and  $1658$  cm<sup>-1</sup>) and decrease ( $\sim 966$ ,  $1255$ ,  $1585$  and  $1618$  cm<sup>-1</sup>) in Raman signal intensity upon infection was again observed. However, different peaks were highlighted to be potentially altering upon infection, showing that by using a 785 nm excitation, complementary

biological information could be gained about the spleen tissue. The prominent Raman peaks at  $1448\text{ cm}^{-1}$  and  $1658\text{ cm}^{-1}$  that appeared to increase in intensity for infected tissue were characteristic of the  $\text{CH}_2\text{CH}_3$  bending modes of proteins (collagen)/ $\text{CH}_2$  vibrational modes of lipids<sup>97</sup> and the Amide I band of proteins in the  $\alpha$ -helix conformation<sup>116</sup>, respectively, implying that *P.berghei* infection within spleen tissue may increase the relative amount of these biological species. However, vibrations attributable to amide III proteins ( $1255\text{ cm}^{-1}$ )<sup>96</sup>, C=C vibrations of phenylalanine<sup>93</sup> ( $1585\text{ cm}^{-1}$ ), and some Hb vibrations<sup>93</sup> ( $1585\text{ cm}^{-1}$  and  $1618\text{ cm}^{-1}$ ) that showed a decrease in signal intensity, suggested that infection may be associated with a decrease and/or alteration in the relative amounts of these particular proteins.

Intensity ratio maps (Figure 3.4(C) and Figure 3.5(C)) were also created to visually show these relative peak changes. The  $1307\text{ cm}^{-1}$  and  $1004\text{ cm}^{-1}$  peaks were used as constant backgrounds for the ratio maps created from the 532 nm and 785 nm data, respectively. With respect to the resonant heat intensity maps, a clear overall increase in the peak intensity ratios within the infected mapped areas compared to the control samples were observed. This suggested alterations to possible biological components including Hb<sup>112,119</sup> ( $\sim 745, 1130$  and  $1170\text{ cm}^{-1}$ ), lipids<sup>93</sup> ( $\sim 1130\text{ cm}^{-1}$ ) and other proteins<sup>93</sup> ( $\sim 1170\text{ cm}^{-1}$ ) at this level of *P. berghei* infection. However, the presence of lipids is typically associated with prominent Raman band at  $\sim 1448\text{ cm}^{-1}$ ,<sup>93</sup> and its absence within the difference spectrum (Figure 3.4(B)) may indicate that lipids are not being seen. Also, within these maps, for both uninfected and infected samples, particularly intense regions were present (Figure 3.4(C)). This could be explained through enhanced Raman intensity from resonance contributions of the biological components within these areas of tissue.

Slightly different trends were observed for the non-resonant heat intensity maps, with an overall decrease in intensity for the infected tissue maps compared to control for  $1255\text{ cm}^{-1}$  (amide III proteins and lipids)<sup>97</sup> peak and  $1585\text{ cm}^{-1}$  (phenylalanine and Hb),<sup>116</sup> which was in good agreement with what was observed in the subtracted Raman spectrum (Figure 3.5(C)). Again, providing evidence of alterations and/or a decrease in concentration to these components upon infection. Whereas, the heat

intensity map  $I_{1448} / I_{1004}$  showed a similar trend of low and high intensity areas for both the control and infected areas that were analysed. Therefore, although from the average, subtracted spectrum it appeared that this biological peak ( $\sim 1448 \text{ cm}^{-1}$  – protein  $\text{CH}_2\text{CH}_3$  modes and  $\text{CH}_2$  vibrations of lipids)<sup>116</sup> increased slightly within the infected spleen sample, when the whole mapped area was studied the distribution of this component was very similar in the non-infected and infected tissue sample. These ratio maps visually showed relative changes in biological peaks in a simple manner and can be used alongside empirical analysis and PCA to aid in classification of tissue types from Raman spectroscopy data.

### 3.2.2 Empirical analysis

Diagnostic algorithms based on peak intensity ratios have been widely employed in the literature for tissue classification using Raman spectroscopy.<sup>95,96,116</sup> These have been shown to successfully correlate variations in tissue spectra with tissue pathology<sup>96</sup> in a simple manner. An empirical analysis based on the peak intensity ratio of two Raman bands was used for tissue classification within this study.

In this study, the empirical analysis focused on the ratio of the Raman peak intensity at  $\sim 745 \text{ cm}^{-1}$  ( $\nu_{15}$  Hb),<sup>93,119</sup> to the peak intensity at  $\sim 1307 \text{ cm}^{-1}$  ( $\nu_{21}$  hemoglobin & lipids)<sup>95,119</sup> for both tissue types imaged at 532 nm. With regards to analysis of the data collected with a 785 nm excitation, the ratio of the peak intensity at  $\sim 1255 \text{ cm}^{-1}$  (amide III protein vibrations) to the peak intensity at  $\sim 1004 \text{ cm}^{-1}$  (phenylalanine)<sup>116</sup> was investigated. An unpaired Student's t-test was used in both instances to assess whether the difference in the Raman intensity ratios ( $I_{745}/I_{1307}$  and  $I_{1255}/I_{1004}$ ) between non-infected and infected tissues was statistically significant.<sup>95,96</sup>

To manage the data for analysis, all infected Raman maps were combined to give one large data matrix containing thousands of Raman spectra, the same process was carried out with the uninfected data. These were then averaged to leave 43 final infected Raman spectra and 43 control spectra ( $n = 43$ ) for both the 532 nm and 785 nm analyses. These data were subsequently used for empirical and multivariate analysis. The intensity ratios for all samples were plotted to observe sample



distribution, along with the average intensity ratio plot for both the control and infected tissue at both wavelengths. This analysis was performed on the same data set used for the PCA model.

Figure 3.6(A) shows the scatter plot of the ratio of Raman peak intensity at  $745\text{ cm}^{-1}$  to  $1307\text{ cm}^{-1}$  ( $I_{745}/I_{1307}$ ) for the 43 averaged *P. berghei* infected samples and 43 uninfected samples analysed with 532 nm excitation. A clear separation was observed in the scatter plot for the two data sets, with replicate data within each tissue type being grouped closely together, indicating little intra-sample variation in the intensity ratios. The mean ratio values (mean  $\pm$  std. dev.) for both control ( $0.90 \pm 0.02$ ) and infected ( $1.12 \pm 0.02$ ) data sets are also given (Figure 3.6(B)). It was shown that the differences between the mean ratios for each tissue type were statistically significant (unpaired Student's t-test,  $p < 0.0001$ ). The infected tissue showed a higher ratio value compared with control, which could be explained by the increase in heme-based Raman vibrations ( $\sim 745\text{ cm}^{-1}$  assigned to  $\nu_{15}\text{ Hb}^{119}$ ) due to the potential presence of hemozoin within the infected samples.

Very good separation was also observed in the scatter plot for the control and infected peak ratios ( $I_{1255}/I_{1004}$ ) analysed at 785 nm (Figure 3.6(C)). As with the 532 nm data, there was little intra-sample variability within the scatter plot for  $I_{1255}/I_{1004}$ , however, in this instance the non-infected ( $1.55 \pm 0.06$ ) data-set displayed a higher ratio value compared with the *P. berghei* infected ( $0.91 \pm 0.03$ ), Figure 3.6(D). This lower average ratio within the infected data-set could be attributed to a decrease in the relative amounts of amide III protein vibrations and  $\text{CH}_2$  modes of lipids upon infection (assigned to  $1255\text{ cm}^{-1}$  peak). This correlates well with what was observed in both the subtracted Raman spectrum (Figure 3.5(B)) and the intensity ratio maps (Figure 3.5(C)) relating to the  $1255\text{ cm}^{-1}$  Raman peak.

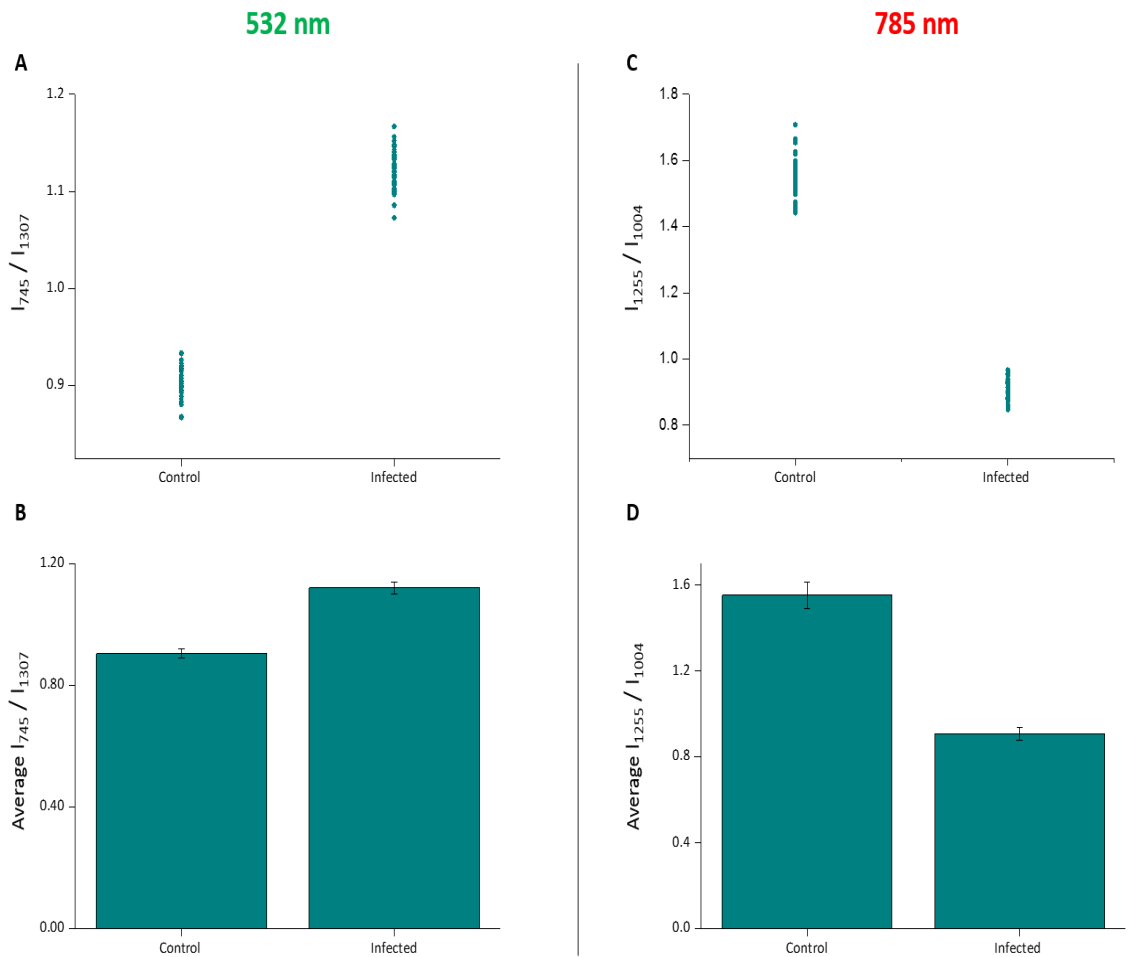


**Figure 3.6** Empirical analysis results for 532 nm ( $I_{745} / I_{1307}$ ) and 785 nm ( $I_{1255} / I_{1004}$ ) tissue imaging data. (A) Scatter plot of peak intensity ratios ( $I_{745} / I_{1307}$ ) for 43 average Raman spectra from all the control and malaria infected mice spleen tissue sections that were mapped with a 532 nm laser excitation. (B) Average intensity ratio plots for the control ( $0.90 \pm 0.02$ ) and infected ( $1.12 \pm 0.02$ ) data sets at 532 nm. This difference in mean ratios was shown to be statistically significant (unpaired Student's t-test,  $p < 0.0001$ ). (C) Scatter plot of peak intensity ratios ( $I_{1255} / I_{1004}$ ) for 43 average Raman spectra from all the control and malaria infected mice spleen tissue imaged with a 785 nm laser excitation. (D) Average intensity ratio plots for the control ( $1.55 \pm 0.06$ ) and infected ( $0.91 \pm 0.03$ ) 785 nm data sets. This difference in mean ratios was shown to be statistically significant (unpaired Student's t-test,  $p < 0.0001$ ). The scatter plots for both data sets (A and C) showed very clear separation of the control and infected groups, with very little intra-sample variability. Error bars (B and D) highlight the standard deviation of the 43 control and 43 infected tissue spectra.

For analysis at both wavelengths used, these results highlight that intensity ratios could be a potential simple and reliable marker to indicate the presence of infection within tissue samples. It was also shown that other peak ratios can also be used to classify the two tissue types with good results (Appendix II). However, this method did not consider the entire Raman spectrum. So, to help improve tissue analysis and classification, PCA was employed to highlight the most diagnostically significant Raman peaks.

### 3.2.3 *Principal component analysis*

PCA was applied to decompose the spectral data into components and attempt to identify subtle changes to biological species within tissue sections which could differentiate infected tissue burden from non-infected samples, in an unsupervised manner. The PCA results for the 532 nm data set are shown in Figure 3.7, which gives the scores plot for PC1 (97.6% variance) against PC2 (1.45% variance), along with the corresponding loadings vectors. As can be seen from the scores plot (Figure 3.7(A)), PC1 was primarily responsible for the separation of the two tissue types. The loadings plot (Figure 3.7(B)) for PC1 indicated that the peaks in the negative half of the plot were spectrally important as they described the Raman peaks that were increasing within the infected tissue vs. the control ( $\sim 750, 1130, 1170, 1225, 1370, 1529, 1588$  and  $1628\text{ cm}^{-1}$ ), with the latter few being more indicative of Hz than Hb. The negative peaks at  $\sim 1529$  and  $1628\text{ cm}^{-1}$  matched closely with that of the sHz reference spectra in Figure 3.8 (core structures of Hb and Hz shown in Appendix III to highlight structural similarities) and therefore suggested detection of the insoluble pigment by Raman. This conclusion was drawn as the  $\sim 1628\text{ cm}^{-1}$  peak matched closely to an intense peak observed at  $1625\text{ cm}^{-1}$  in the sHz reference spectrum but in the Hb reference spectrum this peak was found to have shifted to  $1636\text{ cm}^{-1}$ . Also, a shoulder peak occurring at  $1530\text{ cm}^{-1}$  in the sHz spectrum matched closely with the  $\sim 1529\text{ cm}^{-1}$  PCA peak, whereas this shoulder was seen at  $1538\text{ cm}^{-1}$  in the Hb reference. The negative  $\sim 1370\text{ cm}^{-1}$  peak was present in both reference spectra; however, it was much more prominent within sHz and so suggested that Hz was likely contributing to this peak's appearance within the PC1 loadings plot. It is well known that Hz accumulates within

the spleen,<sup>80,81</sup> therefore it follows that there will be an associated increase in concentration of heme-based Raman vibrations. This is clearly shown in this PCA model as many of the peaks separating the infected tissue from the uninfected samples can be assigned to heme-vibrations, including Hz. Although other proteins and lipids will be present within the tissue and exhibit many similar Raman shifts to those of Hb ( $\sim 1130, 1170, 1225$  &  $1396\text{ cm}^{-1}$ ), resonance effects would mean Hb would tend to dominate the spectra (excitation in the regions of Q-absorption bands),<sup>111,112,119</sup> with the other biological components, such as proteins and lipids, having only small contributions to the observed spectra.

To verify if the Raman peaks being assigned to Hz were correct, its presence within the infected spleen sections was confirmed through tissue staining. An uninfected spleen section and *P. berghei* infected section, on a glass slide, were stained with Prussian blue stain (Figure 3.9). Prussian blue stain was chosen as this can differentiate between the malaria pigment, Hz, from hemosiderin (a normal by-product of Hb degradation). With a typical Giemsa stain, both will stain brown. However, with Prussian blue Hz stains brown and hemosiderin stains blue, therefore allowing differentiation.<sup>120</sup> Images of the stained tissue sections were taken at 10 $\times$  and 20 $\times$  magnification and within the *P. berghei* infected images in Figure 3.9 brown hemozoin deposits were clearly observed (indicated by the black arrows). This provided extra confidence, along with the reference spectra, that Hz was contributing to the infected tissue Raman spectra and that the  $\sim 1529\text{ cm}^{-1}$  and  $\sim 1628\text{ cm}^{-1}$  peaks could be assigned to Hz.

Within the positive peaks in the PC1 loadings plot, the relatively broad  $\sim 1087\text{ cm}^{-1}$  peak was likely to have a significant contribution from Hb (Figure 3.8), however, its broadness suggested contributions from other components. Raman bands within this region could also be assigned to C–C and O–P–O vibrations of nucleic acids.<sup>93,95</sup> The other prominent positive peak at  $\sim 1439\text{ cm}^{-1}$  could primarily be assigned to Raman vibrations from lipids,<sup>95,97</sup> although it may also have had slight Hb contributions ( $\sim 1432\text{ cm}^{-1}$  peak in reference spectrum). The direction and magnitude of these peaks in the loadings plot indicated that they had increased in Raman intensity within

the control tissue over the infected and so contributed to the separation of the two sample groups along PC1. Analysis of the PC1 loadings plot indicated that at this level of *P. berghei* malaria infection Raman spectroscopy could clearly detect H<sub>2</sub> accumulation within the spleen, with the positive peaks (~1087 and 1439 cm<sup>-1</sup>) indicating that as the amount of H<sub>2</sub> increased within the spleen there was a corresponding decrease to Hb and some lipids/ nucleic acid vibrations.

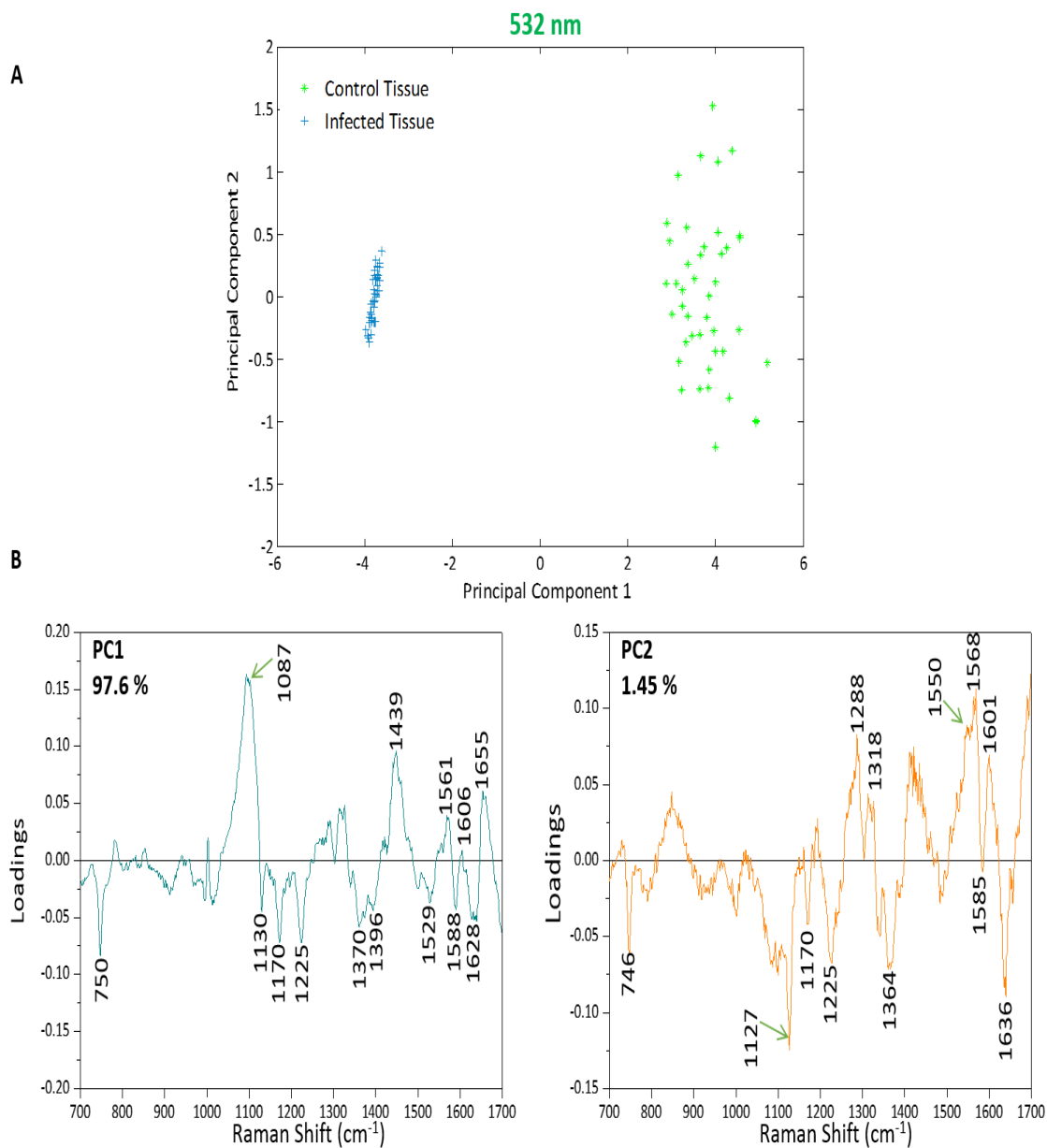


**Figure 3.7** PCA plot for control ( $n = 43$ ) and malaria infected ( $n = 43$ ) samples from mouse spleen tissue sections analysed with 532 nm excitation. (A) Scores plot showing very clear separation of the control (green) and infected (blue) data sets. Separation occurred mainly across PC1, with little separation across PC2. (B) Loadings plots for PC1 and PC2, with the main peaks in both indicated. The peaks in the negative half of PC1 described the prominent biological species that were increasing in Raman signal intensity within the infected tissue when compared to the control samples.

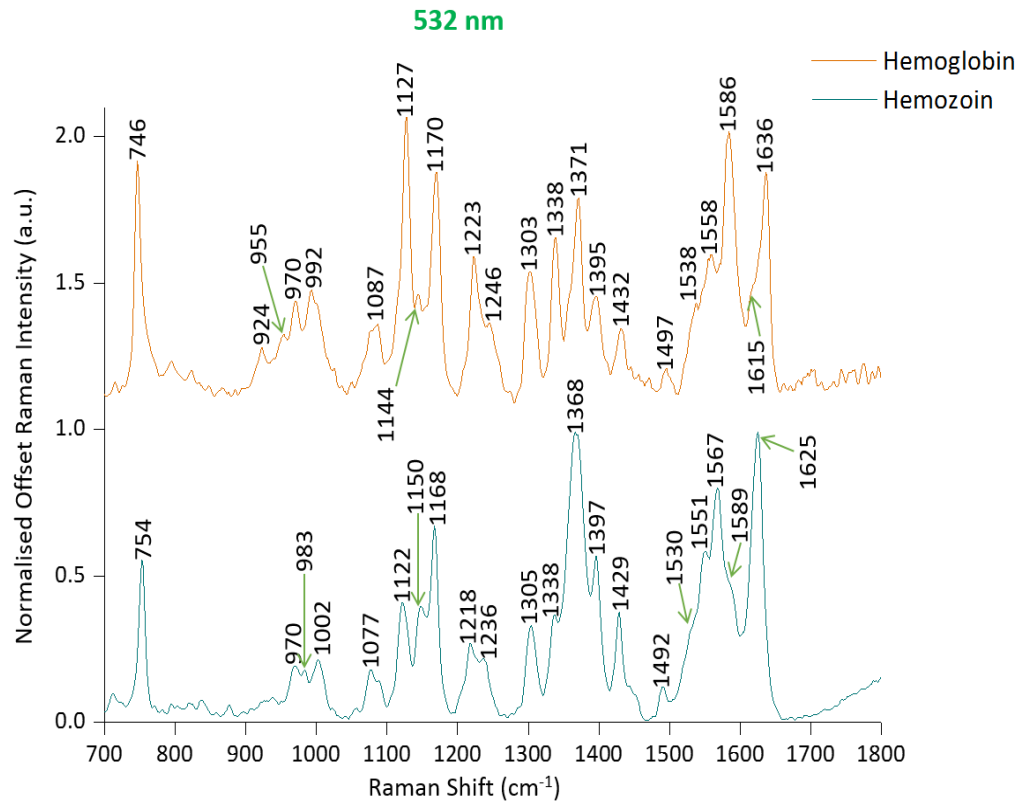


**Figure 3.8** Raman reference spectra of hemoglobin (Hb) and synthetic hemozoin (sHz) with the key Raman bands indicated. Spectra were obtained using 532 nm excitation, 30 s acquisition time with 0.1 mW laser power. Spectra were the average of five replicates of each sample and were baseline corrected using Matlab. They were then normalised to the highest peak and offset for clarity.

PC2 described little separation between the control and infected samples. From the PC2 loadings plot (Figure 3.7(B)) the positive peaks ( $\sim 1550, 1568, 1601 \text{ cm}^{-1}$ ) originated mainly from Hb vibrations, whereas the negative peaks had contributions from Hb as well as from other proteins<sup>93,95</sup> ( $\sim 1170, 1225$  and  $1636 \text{ cm}^{-1}$ ) and lipids<sup>97</sup> ( $\sim 1127 \text{ cm}^{-1}$ ).

With analysis at 532 nm excitation, the separation highlighted an overall increase in heme-based Raman vibrations within the infected samples, which correlated with the accumulation of Hz within the spleen. Hz detection was clear with the identification of key peaks occurring at  $\sim 1370, 1529, 1588,$  and  $1628 \text{ cm}^{-1}$  which matched closely with the reference spectrum. PCA also showed that at the level of *P. berghei* infection reported here, changes to Hb and possibly some other lipid/nucleic acid vibrations

corresponded with an increase in H<sub>2</sub>O content within the spleen. Other proteins (tyrosine  $\sim 1130\text{ cm}^{-1}$ , and amide III  $\sim 1225\text{ cm}^{-1}$ ) were also observed to be contributing to the separation of infected tissue from control. Lipids were also assigned to some Raman shifts ( $\sim 1130\text{ cm}^{-1}$ ) within Table 3.1 and could possibly have been contributing to the separation of the infected tissue within the PCA model (Figure 3.7). However, due to the lack of the prominent lipid band, particularly at  $\sim 1448\text{ cm}^{-1}$ , in both the 532 nm difference spectrum (Figure 3.4(C)) and the PCA loadings plots (Figure 3.7(B)) it is unlikely that lipids were involved in the differences observed between healthy and diseased tissue at this excitation wavelength.

Also due to the resonance effects of heme-based compounds, the separation contribution from other non-heme biological components was slightly smaller as indicated by the peaks in the loadings that were increasing within the infected samples being assigned predominantly to Hb or H<sub>2</sub>O vibrations. When analysed with 532 nm excitation, the separation of non-infected from infected tissue was dominated by the resonance effects from any H<sub>2</sub>O that had been deposited within the infected tissue. However, as can be seen from the stained tissue sections (Figure 3.9) there was not a homogeneous distribution of H<sub>2</sub>O throughout the spleen and it is well documented that the majority of H<sub>2</sub>O deposits are found in the red pulp zones of the splenic structure.<sup>81,121</sup> This makes resonance Raman enhancement and separation of infected spleen tissue reliant on accurately finding the areas within the tissue where H<sub>2</sub>O may be accumulated. Also, Raman imaging would be applied *in-vivo* at the early stages of a suspected malaria infection when the presence of H<sub>2</sub>O may be small. Therefore, PCA was also carried out on the tissue data obtained with 785 nm excitation to determine if a clear separation of non-infected from infected tissue could be obtained without the aid of heme-based resonance enhancements.



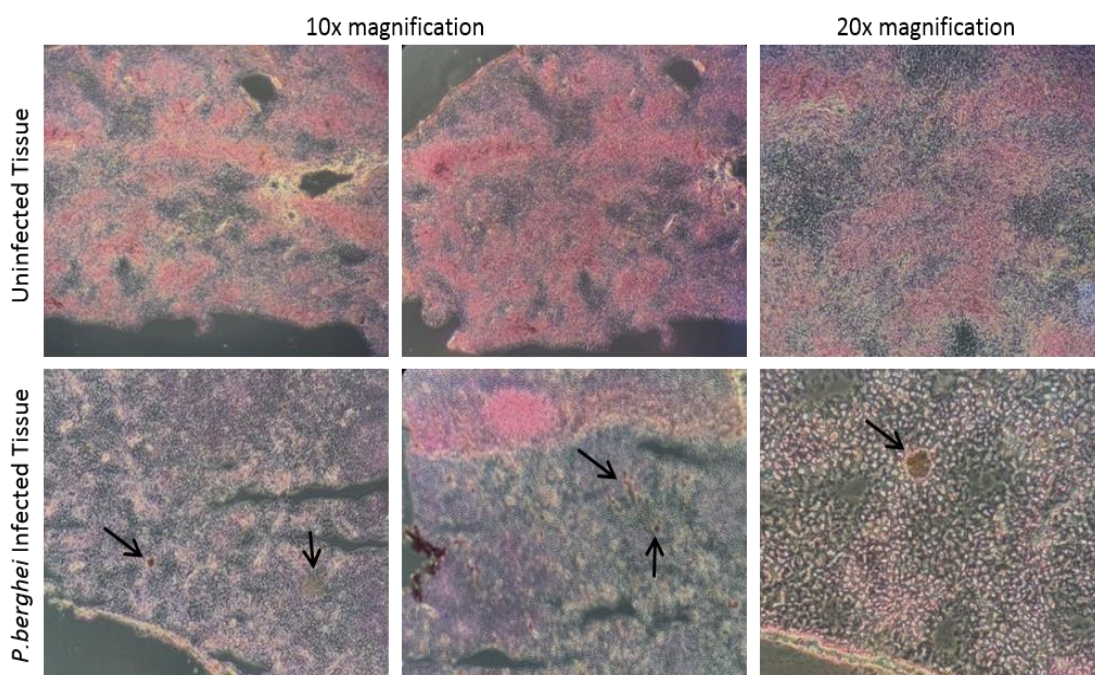


**Figure 3.9** Images of uninfected and *P. berghei* infected spleen sections, stained using Prussian blue stain. Brown H<sub>2</sub>O<sub>2</sub> deposits within the infected samples are indicated by the black arrows. Other results: iron (hemosiderin) - blue; nuclei - red; background - pink.

Figure 3.10 shows the results of the PCA applied to the tissue imaging data set obtained with 785 nm excitation. As with 532 nm data, very clear separation of the two sample groups was observed in the scores plot (Figure 3.10(A)) and as before PC1 accounted for the largest variance (98.3 % variance), with a slight spread of data over PC2 (1.3 % variance). The PC1 loadings plot (Figure 3.10(B)) described the spectral features that contributed to the separation *via* an increase in the intensity for infected compared to control samples ( $\sim 1004$ , 1048, 1320, 1337, 1448, 1585, and 1605  $\text{cm}^{-1}$ ). Tentative peak assignments (Table 3.2) and comparison with Hb/sHz reference spectra (Figure 3.11) showed very little contribution from Hb and/or Hz to these PC1 peaks, with only  $\sim 1585 \text{ cm}^{-1}$  being assigned to Hb vibrations ( $\nu_{37}$ )<sup>97</sup> and a slight shoulder at 1589  $\text{cm}^{-1}$  in the Hz reference spectrum. Also, there could have been a slight contribution from Hb at 1004  $\text{cm}^{-1}$ . This clearly highlights that with 785 nm excitation there was no resonance enhancement from Hb or Hz and other biological components, that were previously masked with 532 nm excitation, were being detected.

The two most distinct peaks that appeared to have an influence on the infected tissue separation were  $1004\text{ cm}^{-1}$ , assigned to  $\alpha$ -amino acid phenylalanine ring breathing mode<sup>97</sup>, and  $1448\text{ cm}^{-1}$ , that originated from  $\text{CH}_2\text{CH}_3$  deformation vibrations of proteins<sup>97</sup> and  $\text{CH}_2$  bending mode of phospholipids.<sup>96</sup> Other peaks were assigned to multiple  $\text{CH}_3\text{CH}_2$  twisting modes of proteins, amide III, phenylalanine, and tyrosine ( $1048$ ,  $1337$ ,  $1585$ , and  $1605\text{ cm}^{-1}$ ).<sup>93,96,97,116</sup> Also, phospholipids ( $1320$ , and  $1337\text{ cm}^{-1}$ ),<sup>93</sup> collagen ( $1337\text{ cm}^{-1}$ ),<sup>116</sup> and some nucleic acid vibrational modes ( $1320$ , and  $1337\text{ cm}^{-1}$ ).<sup>93,96</sup> These spectral features indicated that *P. berghei* infection within the spleen may have caused an increase in the concentration of biological species such as proteins (Amide III, tyrosine, phenylalanine) and phospholipids. The increase in protein concentration upon infection may have had contributions from parasite proteins, for example the highly variable protein PfEMP1 that is expressed by the parasite and involved in sequestration of infected RBCs.<sup>89</sup>

Within the positive peaks in the PC1 loadings plot, one relatively broad and intense peak was observed at  $1255\text{ cm}^{-1}$ , that could be assigned to amide III proteins (mainly in  $\alpha$ -helix conformation)<sup>96</sup> and  $\text{CH}_2$  in-plane deformation of lipids.<sup>93</sup> There were also two less intense peaks in the loadings around  $\sim 1104\text{ cm}^{-1}$  and  $1128\text{ cm}^{-1}$  that were attributed to the biochemical components phenylalanine<sup>93</sup> and phospholipids / Hb vibrations ( $\nu_5$ ),<sup>97</sup> respectively. Analysis of the PC1 loadings plot indicated that at the level of *P. berghei* infection studied here, there was a decrease in the total amount of these biomolecules, relative to the non-infected tissue studied. This decrease was also highlighted in the intensity ratio map in Figure 3.5(C) for  $I_{1255}/I_{1004}$  which showed a much lower intensity distribution throughout the infected tissue, suggesting a decrease in the abundance of these biomolecules upon infection. This indicated that *P. berghei* infection within the spleen altered the structure of key proteins (Amide III) as they were of much greater concentration within the non-infected samples.

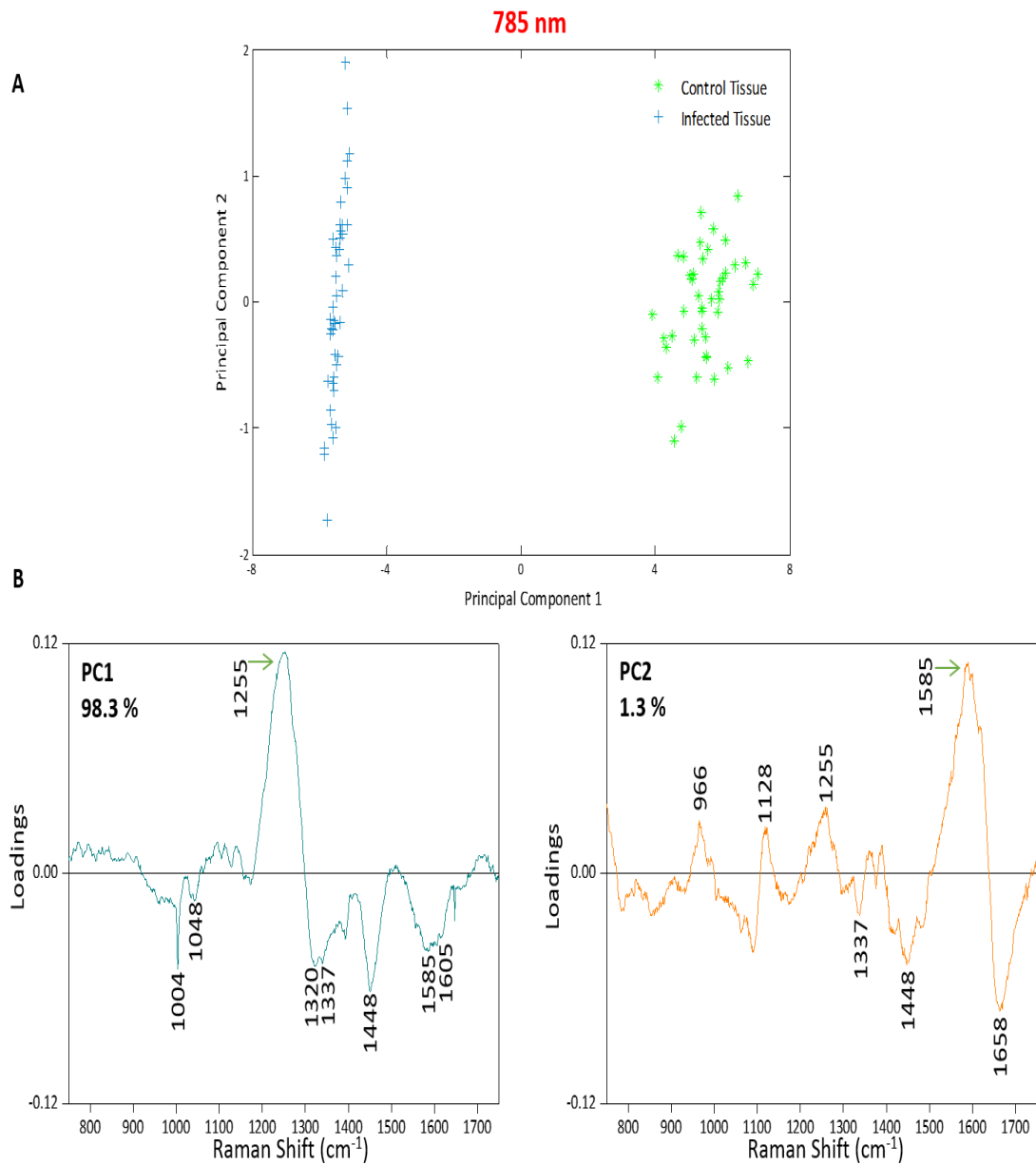


**Figure 3.10** 785nm PCA plot for control ( $n = 43$ ) and malaria infected ( $n = 43$ ) samples from mouse spleen tissue sections. (A) Scores plot showed very clear separation of the control (green) and infected (blue) data sets. Separation occurred mainly across PC1, with a slight spread of data across PC2. (B) Loadings plot for PC1 and PC2, with the main peaks indicated in both. The peaks in the negative direction in PC1 described the biological components that were increasing in Raman signal intensity within the infected tissue compared to the controls.

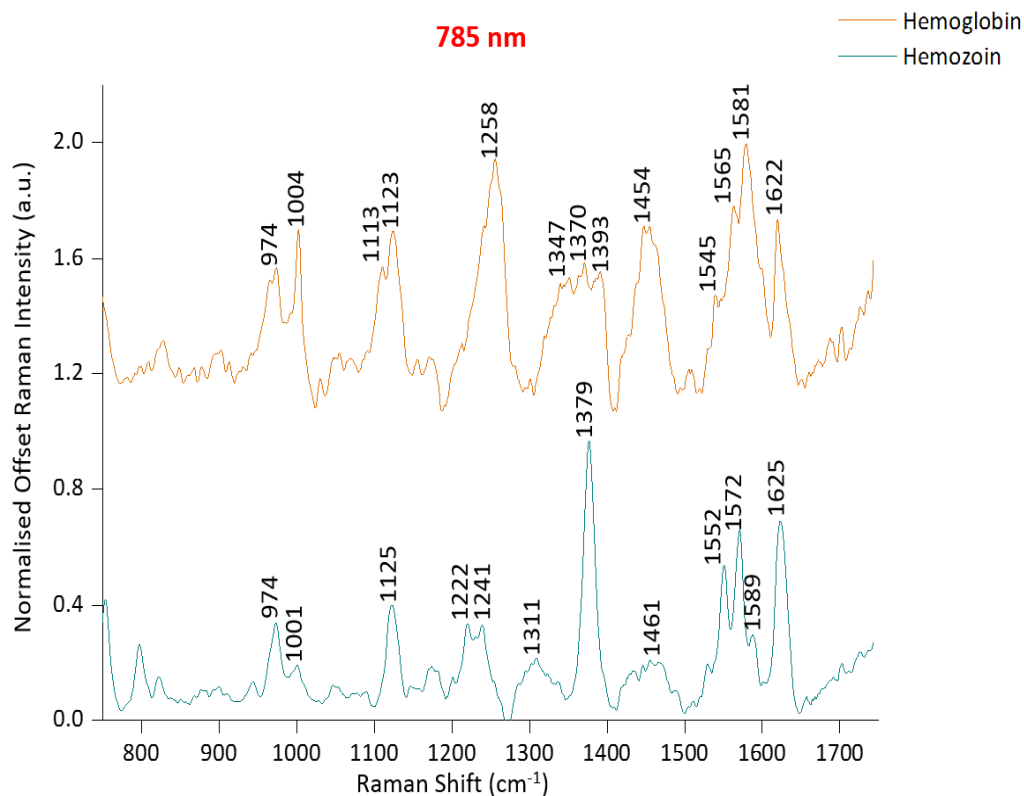


**Figure 3.11** Raman reference spectra of hemoglobin (Hb) and synthetic hemozoin (sHz) with the key Raman bands indicated. Spectra were obtained using 785 nm excitation, 6 s acquisition time with 190 mW laser power. Spectra were the average of five replicates of each sample and were baseline corrected using Matlab. They were then normalised to the highest peak and offset for clarity.

As before, PC2 described little of the separation between the two sample groups, only 1.3 % of the variance. From the PC2 loadings plot (Figure 3.10(B)) the positive peaks ( $\sim 966, 1128, 1255, 1585 \text{ cm}^{-1}$ ) originated primarily from lipids (phospholipids,  $\text{CH}_2$  in-plane deformation),<sup>93</sup> amide III protein,<sup>97</sup> phenylalanine,<sup>116</sup> and Hb vibrations ( $\nu_5$  and  $\nu_{37}$ ).<sup>97</sup> Whereas, the negative peaks ( $\sim 1337, 1448, 1658 \text{ cm}^{-1}$ ) can be attributed to  $\text{CH}_2\text{CH}_3$  deformations of collagen,<sup>96</sup> amide I and III ( $\alpha$ -helix),<sup>93,97</sup> and  $\text{CH}_2$  vibrations of lipids/phospholipids.<sup>96</sup> Within the scores plot there was a large intra-sample spread of the infected tissue along PC2. This range of data most likely occurred because the tissue had a heterogenous distribution of infection so the infected peaks in the positive half of PC2 had a much greater contribution from the biochemical components assigned to these peaks, whereas the infected data in the

negative half of PC2 had much greater characteristics from the molecules assigned to  $\sim 1337$ ,  $1448$  and  $1658\text{ cm}^{-1}$  peaks. However, this spread of infected data along PC2 did not influence the separation from the controls in the scores plot and it was very clear that the information rich PC1 loadings was the most important one to use to describe the separation.

These PCA results indicated that Raman imaging, using both a resonant and non-resonant excitation wavelength, provided rich biochemical information about tissue samples and excellent discrimination was achieved between *P. berghei* infected spleen from uninfected samples. When a  $532\text{ nm}$  excitation was used the separation of the two data sets highlighted an overall increase in heme-based Raman vibrations within the infected samples, which correlated with the accumulation of Hb within the spleen. Hb detection was clear with the identification of key peaks occurring at  $\sim 1370$ ,  $1529$ ,  $1588$ , and  $1628\text{ cm}^{-1}$  that matched closely with its reference spectra. Chemometric analysis also showed that at the level of *P. berghei* infection under study, changes to Hb and some other lipid/nucleic acid vibrations corresponded with an increase in Hb content within the spleen. Other proteins (tyrosine  $\sim 1130\text{ cm}^{-1}$ , and amide III  $\sim 1225\text{ cm}^{-1}$ ) and lipids ( $\sim 1130\text{ cm}^{-1}$ ) were also contributing to the separation of infected tissue from control. However, due to the resonance effects of heme-based compounds, mainly Hb, the separation contribution from these biological components was smaller. By imaging the tissue with  $785\text{ nm}$  excitation, biomolecular information was gained about the non-resonant components that were possibly masked by the intense heme-based Raman peaks in the  $532\text{ nm}$  data collection. From analysis of the Raman spectra and the resulting PCA loadings, it was noted that there was very little influence from Hb or Hb, highlighting that this excitation wavelength was not giving resonance Raman enhancement.

Imaging tissue sections demonstrated the potential use of Raman spectroscopy to provide detailed chemical information from a biological matrix, however, this needs to be transferable to *in-vivo* diagnostics to be useful in detecting malaria infection burden. So, to investigate this possibility, an *in-vivo* mouse model that had been

injected with human *P. falciparum* infected RBCs was analysed using a portable in-house built Raman spectrometer equipped with 785 nm laser.

### 3.2.4 Animal models

An *in-vivo* Raman imaging mouse model was used to study the potential of Raman spectroscopy to gain biological information from whole organs and to discover if the data gained from the tissue sections was translatable to what was observed *in-vivo*. Raman measurements were performed using an in-house built system with a 785 nm excitation laser (Figure 3.12). The laser was coupled to a fibre-optic Raman probe (Probe 1), with the probe being mounted, at a 90° angle, on a xyz translation stage for precise positioning of the mouse.<sup>122</sup>

All animal dosing and handling was carried out by Dr Gavin Meehan at the University of Glasgow. Five NSG mice (an immunodeficient mouse strain) were imaged, three of which were injected, *via* intravenous tail vein injection, with human *Plasmodium falciparum* parasite infected RBCs (purified parasitemia 60 - 70 %). Once injected, the infected RBCs circulated the mouse body and rapidly entered the spleen and liver. Two control mice were also studied and received uninfected RBCs *via* tail vein injection. Once anaesthetised the fur was removed and the mouse was manipulated underneath the Raman probe to allow imaging of the spleen and liver. Single point spectra were taken in three different areas of the spleen and liver. Once the spectra had been collected the mice were culled, and the spleen and liver harvested to allow *ex-vivo* spectra to be recorded from three different areas of each organ. All the collected spectra were then averaged to give a single averaged spectrum for each mouse. The results from the analysis of the liver and the spleen, both *in-vivo* and *ex-vivo*, are shown in Figure 3.13 and Figure 3.14, respectively.

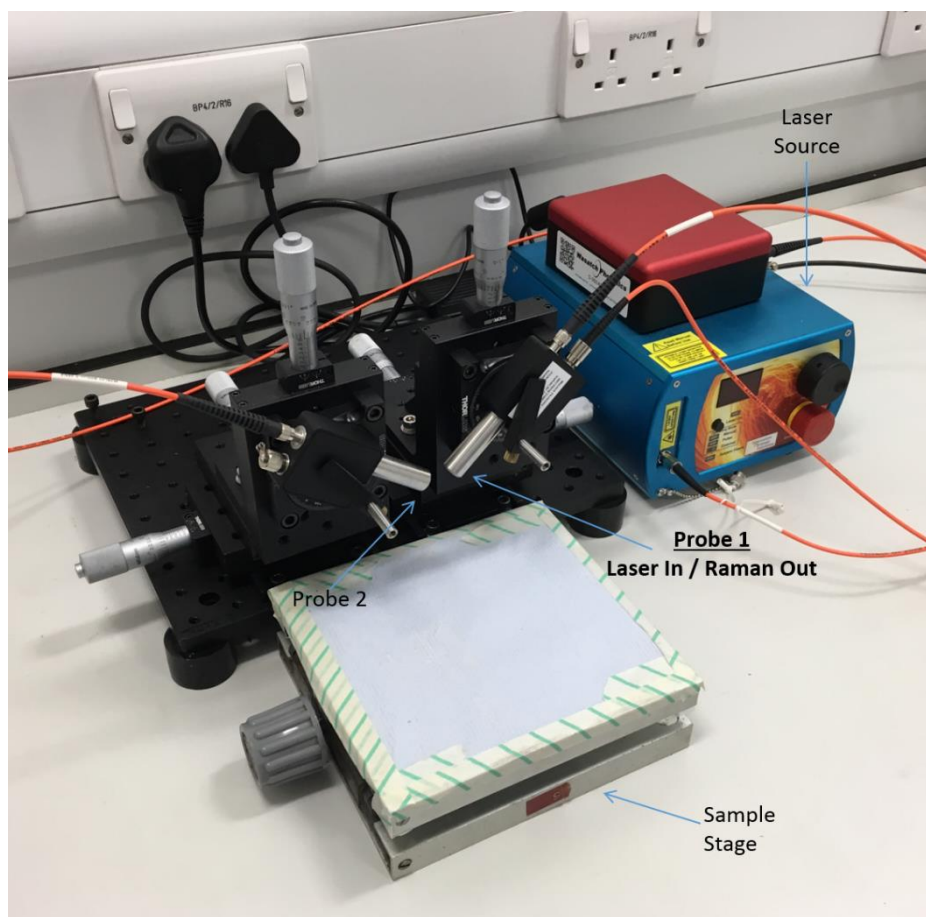


**Figure 3.12** Photograph of in-house built 785 nm system used in animal experiments. Each mouse was manipulated underneath probe 1 to allow Raman spectra from either the liver or spleen to be collected. *Ex-vivo* organs were placed on glass slides and positioned underneath the probe. Although angled in the photograph, for Raman measurements probe 1 was positioned at 90° angle to the sample stage. The sample stage could be moved in the xyz plane to allow precise positioning of each mouse. The key components of the instrument are also labelled.

Imaging of the liver and spleen both *in-vivo* and *ex-vivo* showed very similar Raman peaks for both the infected (Mouse 1-3) and non-infected (Mouse 4-5) mice, with tentative peak assignments in Table 3.3. Multiple peaks recorded from the mouse models match closely with those seen in the spleen tissue sections mapped at 785 nm ( $\sim 1255, 1320, 1337, 1448, 1585, \text{ and } 1658 \text{ cm}^{-1}$ ). These biochemical peaks can be attributed to multiple protein assignments including amide I ( $\alpha$ -helix), amide III, collagen, elastin, and phenylalanine, native C-H, and  $\delta(\text{CH}_2)$  of lipids in tissue, fatty acids, and some nucleic acid vibrations within the whole organs.

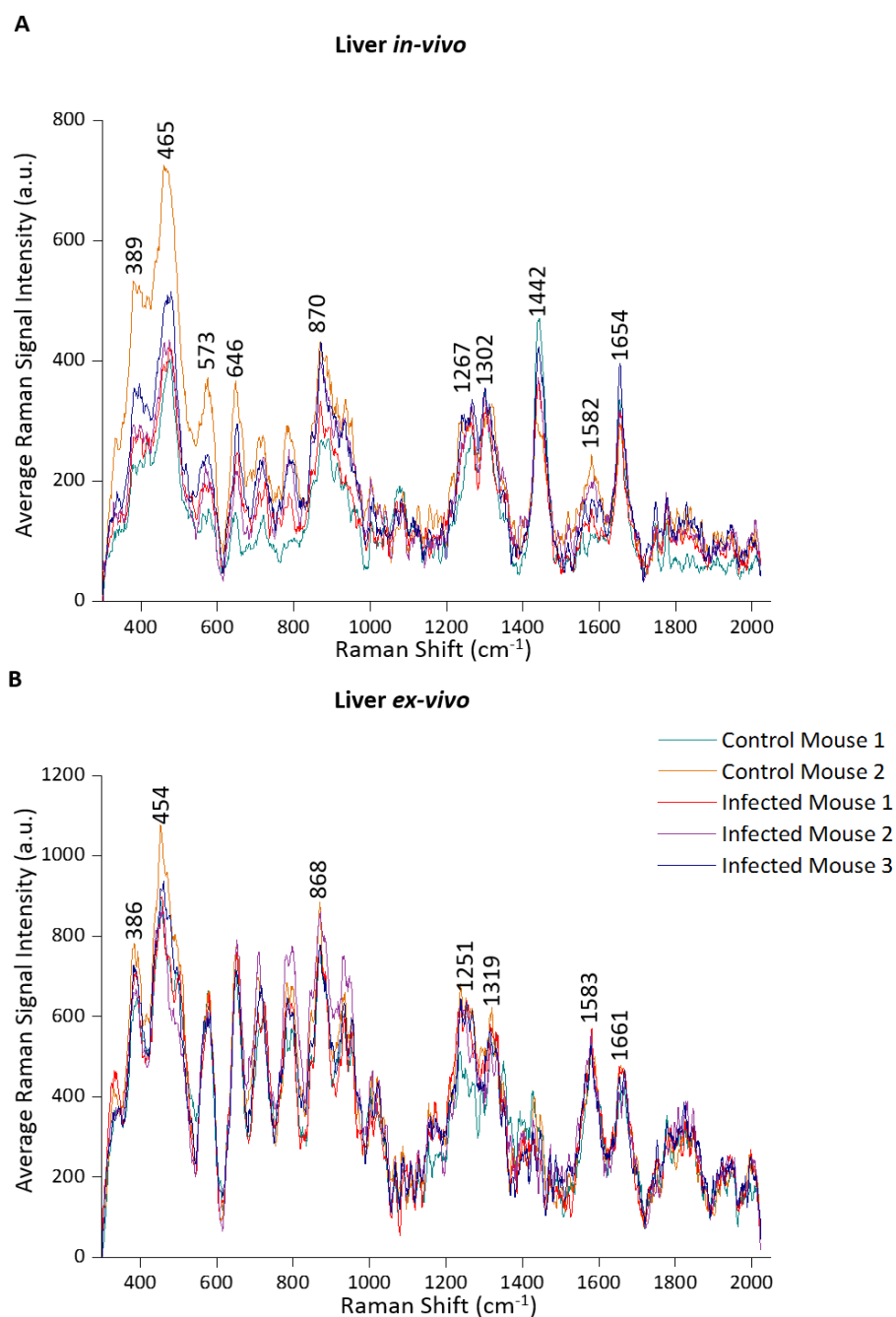


**Figure 3.13** Analysis of mouse liver with in-house built 785 nm (A) Average spectra from the 5 mice studied, taken from the liver *in-vivo*. (B) Average liver *ex-vivo* spectra for the same 5 mice. The spectra for control mouse 1 (cyan), control mouse 2 (orange), infected mouse 1 (red), infected mouse 2 (purple), and infected mouse 3 (dark blue) are the average of 3 spectra taken from different points on the liver. Spectra were recorded with 1 s acquisition time, 0.45 mW 785 nm laser excitation, and baselined using Matlab software. The most prominent Raman peaks are also labelled.



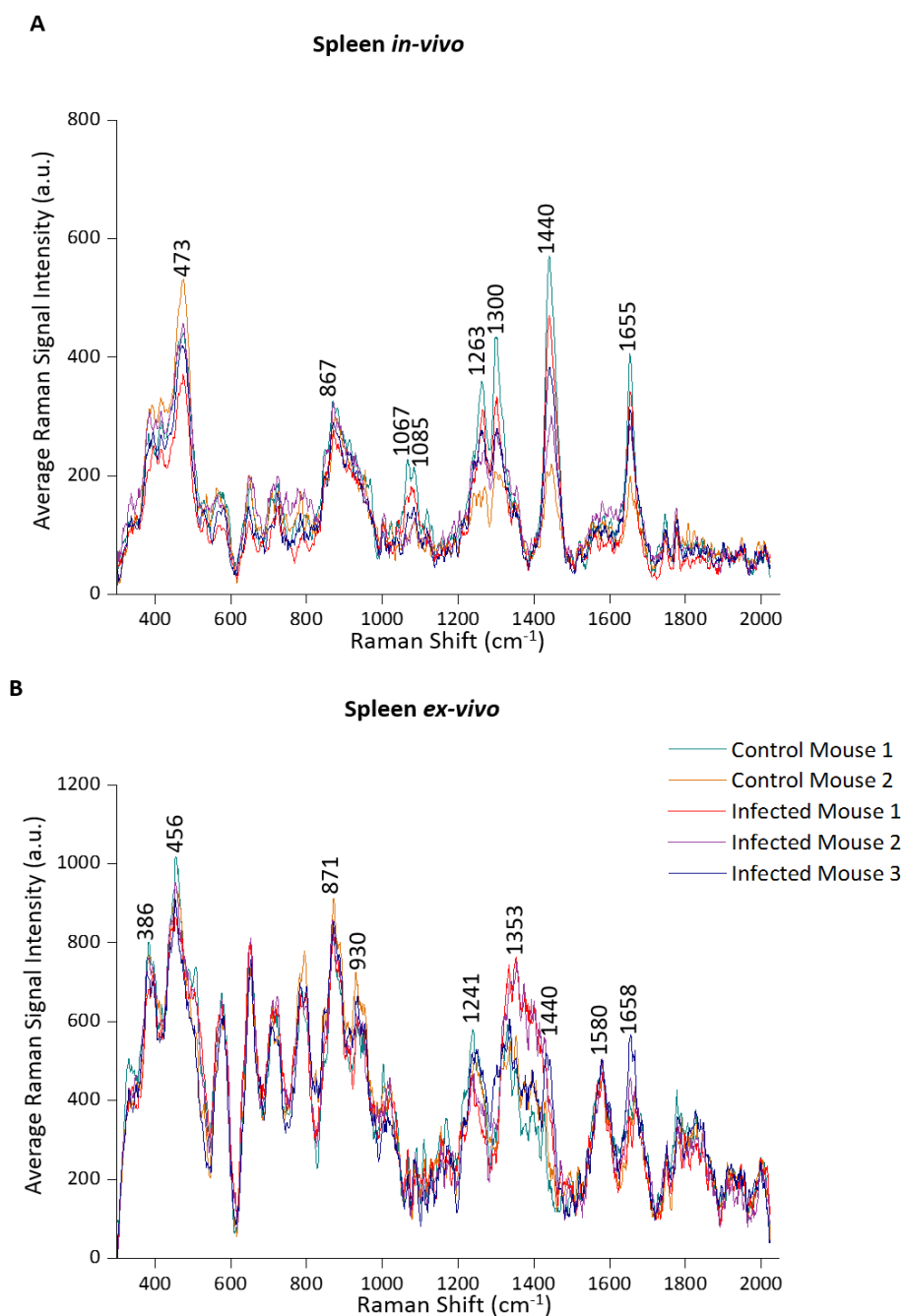


**Figure 3.14** Analysis of mouse spleen with in-house built 785 nm (A) Average spectra from the 5 mice studied, taken from the spleen *in-vivo*. (B) Average spleen *ex-vivo* spectra for the same 5 mice. The spectra for control mouse 1 (cyan), control mouse 2 (orange), infected mouse 1 (red), infected mouse 2 (purple), and infected mouse 3 (dark blue) are the average of 3 spectra taken from different points on the spleen. Spectra were recorded with 1 s acquisition time, 0.45 mW 785 nm laser excitation, and baselined using Matlab software. The most prominent Raman peaks are also labelled.

**Table 3.3** Tentative peak assignments for the main Raman peaks observed for Raman imaged liver and spleen organs both *in-vivo* and *ex-vivo*, with 785 nm excitation source.

| Liver                           |                | Spleen         |                | Assignments <sup>a</sup>  |
|---------------------------------|----------------|----------------|----------------|---|
| <i>In-vivo</i>                  | <i>Ex-vivo</i> | <i>In-vivo</i> | <i>Ex-vivo</i> |   |
| Raman Shift (cm <sup>-1</sup> ) |                |                |                |   |
| 389                             | 386            | -              | 386            | -   |
| 465                             | 454            | 473            | 456            | Ring torsion of phenyl, Polysaccharides   |
| 573                             | -              | -              | -              | Tryptophan/cytosine, guanine  |
| 646                             | -              | -              | -              | C-C twisting mode of Phe & Tyr  |
| 870                             | 868            | 867            | 871            | $\nu$ [single bond] for amino acids proline & valine & polysaccharides  |
| -                               | -              | -              | 930            | $\nu$ (C-C) amino acids proline & valine, skeletal C-C, $\alpha$ -helix   |
| -                               | -              | 1067           | -              | Proline (collagen)  |
| -                               | -              | 1085           | -              | Phosphodiester groups in nucleic acids  |
| 1267                            | 1251           | 1263           | 1241           | Proteins (amide III), C-H (lipids in tissue), DNA ring breathing modes, $[\text{PO}_2^-]_{\text{asym}}$ (nucleic acids)                         |
| 1302                            | 1319           | 1300           | 1353           | Amide III, $\delta$ (CH <sub>2</sub> ) lipids & proteins (collagen), fatty acids  |
| 1442                            | -              | 1440           | 1440           | Proteins ( $\delta$ (CH <sub>2</sub> ), $\delta$ (CH <sub>3</sub> ), collagen), Lipids ( $\delta$ (CH <sub>2</sub> ) scissoring, phospholipids) |
| 1582                            | 1583           | -              | 1580           | Proteins (Phe, $\delta$ (C=C)), $\nu_{37}$ Hb [ $\nu$ (CC) <sub>asym</sub> ]  |
| 1654                            | 1661           | 1655           | 1658           | Proteins ( $\nu$ (C=O) amide I $\alpha$ -helix, collagen, elastin), Fatty acids   |

<sup>a</sup> Abbreviations:  $\nu$  – stretch vibration;  $\delta$  – in-plane bending vibration; sym – symmetric; asym – asymmetric; Hb – hemoglobin; Phe – phenylalanine; Tyr – tyrosine. Assignments from ref.<sup>93</sup>

Many of the same Raman peaks were observed in the *ex-vivo* spectra, for both organs, as those in the *in-vivo* interrogation. This highlighted that Raman spectra were being recorded from the surface of the target organs *in-vivo*, although there will have been large contributions from biological components such as lipids within the mouse skin. Raman contributions from animal skin may explain the slightly sharper and more resolved peaks seen in the *in-vivo* spectra (Figure 3.13(A) and Figure 3.14(A)). From analysis of the average spectra from both organs no clear peak variations were observed between the control and *P. falciparum* infected mice. To

investigate if any subtle changes to the biological components within the organs could be detected, PCA was applied to decompose the spectral data. Six spectra of infected tissue, selected randomly from the nine point spectra collected from the infected mice (each of the three infected mice were interrogated with the laser three times), and the six control mice spectra (three from each control mouse) for *in-vivo* and *ex-vivo* samples of both organs were used in the PCA models, with the scores plot results shown in Figure 3.15.

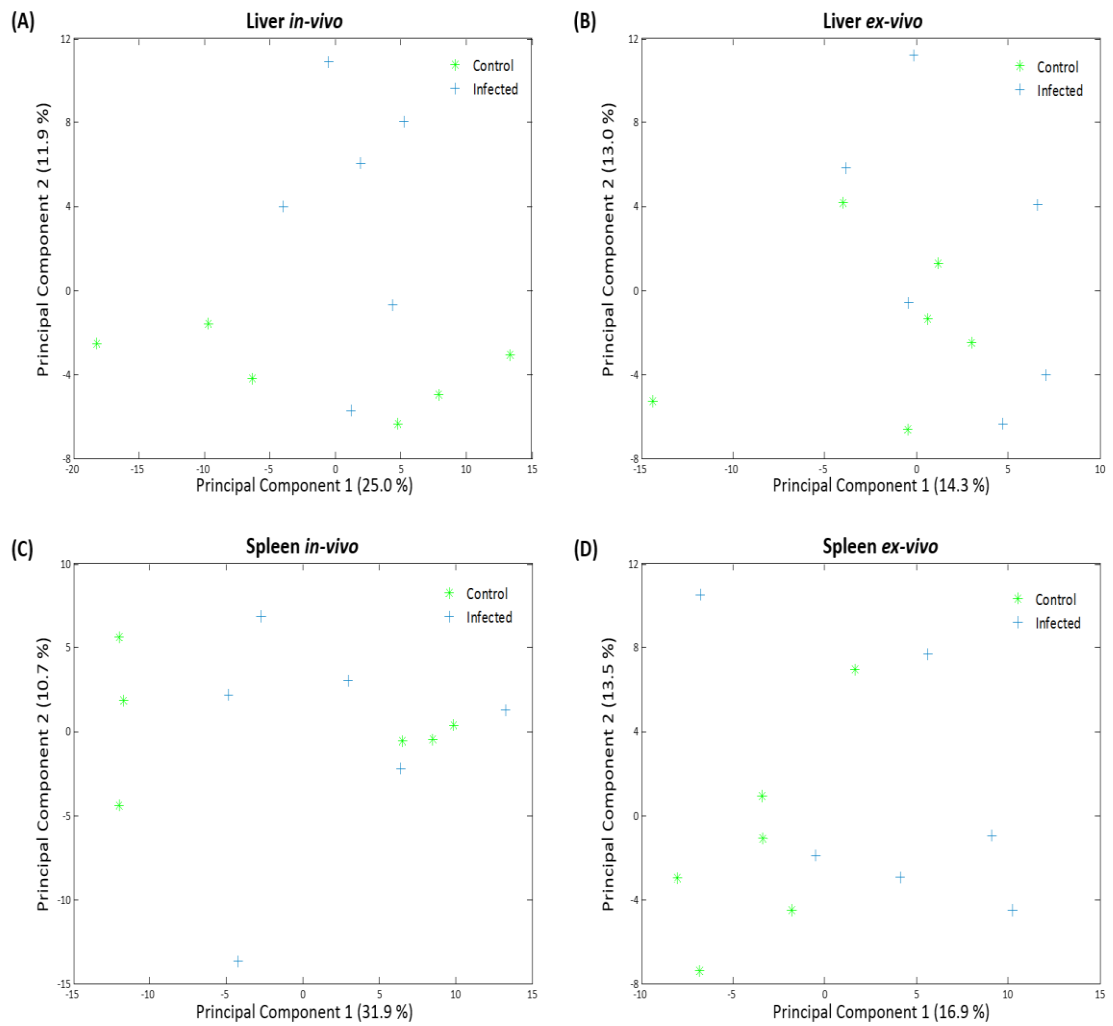


**Figure 3.15** PCA scores plot results for PCA of each sample set. (A) Sores plot for the PCA of 6 control and 6 *P. falciparum* infected mice spectra gained from the liver in-vivo. (B) PCA scores plot of data gained from the same mice liver ex-vivo. (C) Scores plot from PCA results of mice spleen recorded in-vivo. (D) PCA scores plot of the same mice spleen, data recorded ex-vivo. PCA analysis overall showed no clear separation of the control and infected data sets for the mice liver or spleen under the two conditions they were analysed under. Control samples are shown in green and infected shown in blue within the score's plots.

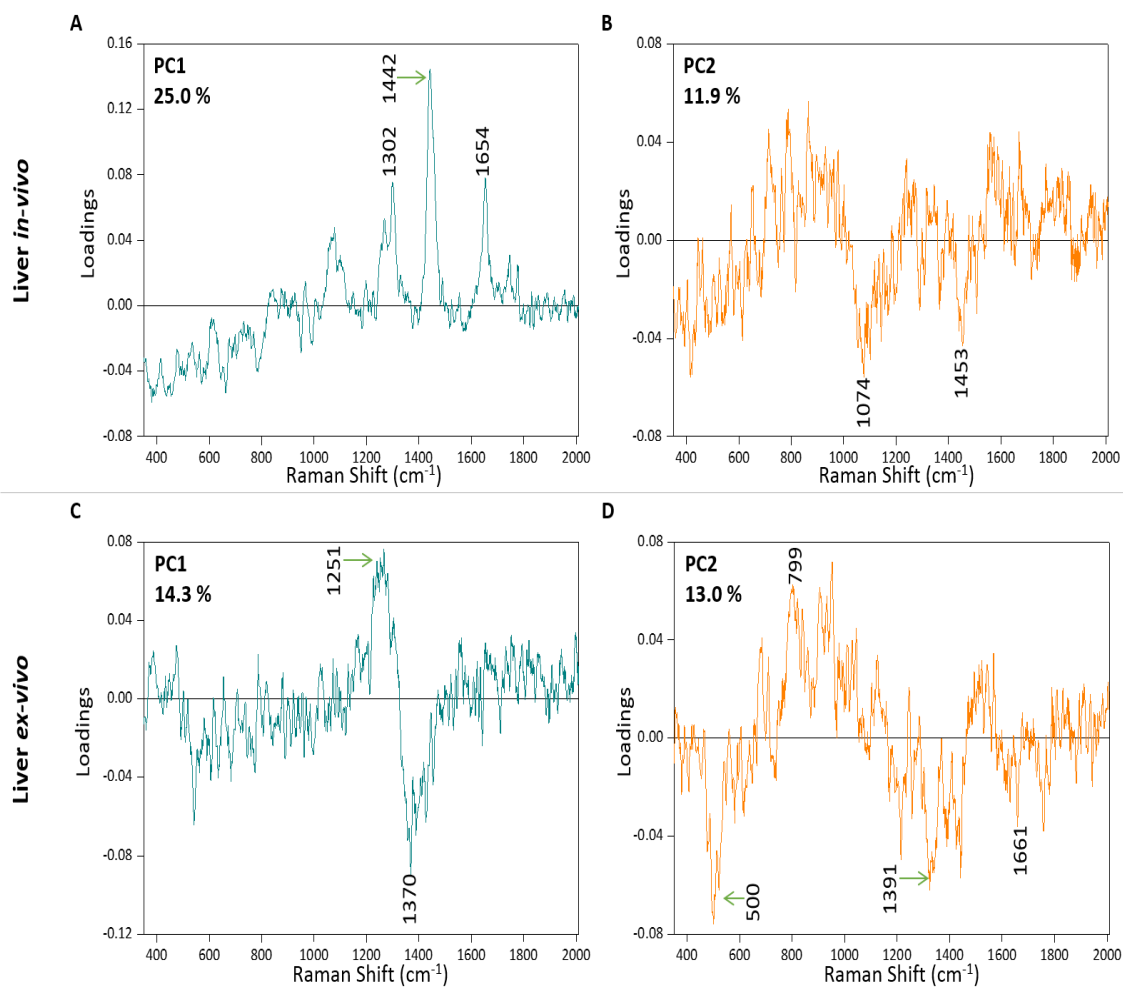


**Figure 3.16** PCA loadings plots. (A) Corresponding PC1 loadings plot for PCA carried out on *in-vivo* liver data. (B) PC2 loadings plot for *in-vivo* liver PCA. (C) Corresponding PC1 loadings plot for PCA carried out on *ex-vivo* liver data. (D) PC2 loadings plot for *ex-vivo* liver PCA.

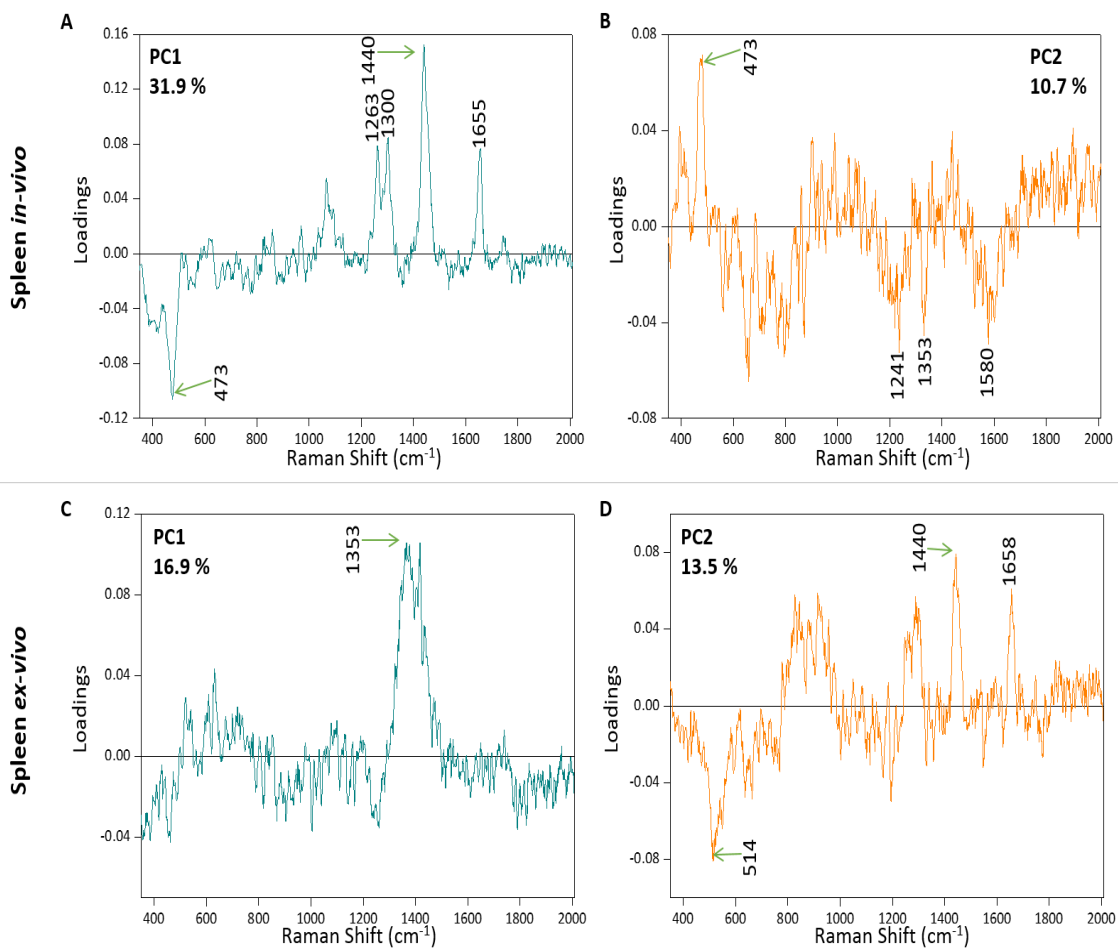


**Figure 3.17** PCA loadings plots. (A) Corresponding PC1 loadings plot for PCA carried out on *in-vivo* spleen data. (B) PC2 loadings plot for *in-vivo* spleen PCA. (C) Corresponding PC1 loadings plot for PCA carried out on *ex-vivo* spleen data. (D) PC2 loadings plot for *ex-vivo* spleen PCA.

PCA for the liver and the spleen, both *in-vivo* and *ex-vivo*, showed little to no meaningful separation of the two mice groups. Analysis of the liver *in-vivo* scores plot (Figure 3.15(A)) highlighted a cluster of three control data-points appearing to separate from the rest of the data along PC1 to the negative side (25.0 % variance) and a slight cluster of four *P. falciparum* infected spectra separating along PC2 (11.9 % variance). PC1 loadings plot for the *in-vivo* liver PCA (Figure 3.16(A)) highlighted the data within the positive part of PC1 had slightly more influence from the peaks occurring at ~1302 (amide III protein,  $\delta(\text{CH}_2)$  lipids, and fatty acids), 1442 (proteins [ $\delta(\text{CH}_2)$ ,  $\delta(\text{CH}_3)$ , collagen],  $\delta(\text{CH}_2)$  lipids), and 1654  $\text{cm}^{-1}$  (amide I proteins, elastin, collagen, and fatty acids). Little information was gained from *in-vivo* liver PC2 loadings (Figure 3.16(B)) with the infected data appearing in the positive half seeming to separate due to peaks ~1582 ( $\delta(\text{C}=\text{C})$  proteins, phenylalanine) and 1654  $\text{cm}^{-1}$  (amide I proteins, collagen, and fatty acids). However, these peaks were not well resolved within the PC2 loadings plot, describing little variance within the whole data set for the liver *in-vivo* analysis. With regards to the *ex-vivo* liver analysis, PCA described even less variance within the data compared to the *in-vivo* model showing no statistical difference between the infected and control mice livers. The corresponding loadings plots for PC1 and PC2 (Figure 3.16(C and D)) were poorly resolved.

The spleen *in-vivo* scores plot (Figure 3.15(C)) showed little separation of the data, with a grouping of three control spectra and then three infected in the negative part of PC1 loadings (31.9 % variance). From the PC1 loadings plot (Figure 3.17(A)) the peaks that appeared in the positive side ~1263, 1300, 1440, and 1655  $\text{cm}^{-1}$  were attributed to biological components including amide III, C-H lipids, collagen, fatty acids, amide I proteins, and elastin. Also, one intense peak seen in the negative half of PC1 loadings, ~473  $\text{cm}^{-1}$ , was assigned to ring torsion of phenyl and polysaccharides. As with the liver *in-vivo* PC2 loadings, the corresponding spleen *in-vivo* PC2 loadings (Figure 3.17(B)) provided little information on the data, with the peaks that were identified being noisy and poorly resolved. PCA carried out on the spleen *ex-vivo* data also showed no statistical separation of the control and *P.*

*falciparum* infected mice, with both PC1 and PC2 (Figure 3.17(C and D)) describing very little variance, 16.9 % and 13.5 %, respectively.

With the very small data set studied in this investigation, no relevant separation was achieved between the control and infected mice groups, either *in-vivo* or *ex-vivo* for either organs. To study further if Raman spectroscopy has the capability to differentiate infected mice from a control group, a larger *n* number of mice must be used with a greater number of spectra taken from each organ to perhaps gain a more representative Raman spectrum of the whole organ. Also, a common problem that was observed with imaging live animals, and *ex-vivo*, within the optical tissue window (650 – 950 nm) was large backgrounds due to tissue autofluorescence (Appendix IV). These backgrounds were removed with subtraction, although it is possible that some biological information could have been lost in this process.

A further drawback of *in-vivo* Raman measurements is the surface selectivity of the measurement. The observed spectrum has major contributions from the surface layer of the sample, such as the mouse skin, which makes the collection of spectral information from the subsurface challenging. However, with the development of SORS, biological information can be collected from the subsurface of a multi-layered system.<sup>105,109,122</sup> SORS provides a means of subsurface analysis when obscuring barriers such as tissue are present. By varying the distance of the collection probe from the laser excitation (sometimes by a few millimetres), Raman contributions from subsurface layers can be acquired.<sup>103</sup> The in-house built spectrometer used in this study to collect Raman spectra has the capability to carry out SORS measurements by using probe 1 as the laser input and probe 2 (shown in Figure 3.12) as the SORS collection probe. Further animal studies could look as using a SORS set-up to gain more relevant spectral information from depth within the spleen and/or liver of mice.



### 3.3 Concluding Remarks

Here work was carried out primarily as a proof-of concept to highlight the ability of Raman imaging to be able to differentiate malaria parasite infected tissue from non-infected samples. *P. berghei* malaria infected mouse spleen was chosen as it is a well-used model in malaria research to understand human infection and parasitised RBCs are known to sequester within this organ. This was investigated with the idea that Raman spectroscopy, or more likely an analogue such as SORS, could non-invasively be applied to assess tissue burden in suspected cerebral malaria cases and assist in earlier identification of this severe form of malaria.

A combination of 532 nm laser excitation, to give resonance Raman information from the tissue, and 785 nm excitation to study the Raman contributions, along with multivariate analysis, resulted in very clear discrimination of *P. berghei* infected tissue sections from the non-infected samples. From the resonance Raman data, the PCA separation highlighted an overall increase in heme-based Raman vibrations within the infected samples, which correlated with the accumulation of Hz within the spleen contributing to this. Hz detection was clear with the identification of key peaks occurring at  $\sim 1370$ , 1529, 1588, and  $1628\text{ cm}^{-1}$  which matched closely with the sHz reference spectrum. It was also concluded that changes to Hb and potentially other lipid/nucleic acid vibrations corresponded with an increase in Hz content. Other protein bands assigned to tyrosine and amide III were also found to be contributing to the separation of infected from the non-infected tissue. However, as discussed above, resonance effects from exciting in the region of the Q-absorption bands of Hb and Hz (as it shares the same heme-core as Hb) meant that contributions to the observed Raman spectra from other biological components would have been minimal.

Tentative peak assignments and comparison of reference spectra for the 785 nm data revealed very little contribution from heme-based Hb or Hz within the spectra, showing no heme-resonance enhancement was gained using this laser excitation. Chemometric analysis identified two key peaks at  $\sim 1004\text{ cm}^{-1}$  (phenylalanine) and  $1448\text{ cm}^{-1}$  (proteins such as collagen) that appeared to be altered within the *P.*

*berghei* infected tissue compared with the control. Further peaks attributed to multiple CH<sub>3</sub>CH<sub>2</sub> twisting modes of proteins, amide III, phenylalanine, and tyrosine (1048, 1337, 1585, and 1605 cm<sup>-1</sup>) phospholipids (1320 and 1337 cm<sup>-1</sup>), collagen (1337 cm<sup>-1</sup>), and nucleic acid vibrational modes (1320, 1337 cm<sup>-1</sup>) were also important in describing the alteration of spleen tissue in the infected state. This analysis highlighted that *P. berghei* malaria infection within the spleen had altered the concentration and/or the composition of these assigned biomolecules, relative to the non-infected control samples. It was also concluded that infection led to a decrease in the total amount of some biomolecules when compared to the control, mainly ~1255 cm<sup>-1</sup> (amide III and CH<sub>2</sub> lipids), 1104 cm<sup>-1</sup> (phenylalanine), and 1128 cm<sup>-1</sup> (phospholipids and Hb vibrations,  $\nu_5$ ). These changes, seen in both the tissue analysis at 532 nm and 785 nm, were also reflected within the intensity ratio maps.

The use of peak ratio maps and empirical analysis for the tissue analysed at 532 nm highlighted an overall increase in biological components including Hb ( $\nu_{15}$ ,  $\nu_5$ ,  $\nu_{30}$ ), lipids, and proteins (tyrosine) going from the control towards an infected tissue state. Analysis with 785 nm excitation revealed different trends to what was observed in the resonance Raman images. Within the infected areas of the ratio maps, an overall decrease in Raman peak intensity, and so abundance of biological components such as amide III proteins (1255 cm<sup>-1</sup>), phenylalanine, and Hb (1585 cm<sup>-1</sup>) occurred. The tissue area studied also showed that the distribution and relative Raman intensity of the 1448 cm<sup>-1</sup> peak (CH<sub>2</sub>CH<sub>3</sub> deformation vibrations of proteins, and CH<sub>2</sub> bending modes of lipids) was similar between the control and infected area. However, in the PCA model, which was carried out on a data set obtained from the accumulation of multiple Raman tissue maps, this peak was shown to vary in the infected samples vs. the controls. This shows that Raman peak ratio maps should be interpreted with some caution as they are only focussing on small areas of a larger sample. Empirical analysis carried out for both the resonant and non-resonant data gave very good discrimination between control and infected samples, with little intra-sample variability. These two simple data analysis methods could be used as tools in

combination with PCA to help improve efficiency of Raman tissue analysis and classification.

Results from *in-vivo* animal studies, with a 785 nm excitation, gave spectra that matched very closely with the Raman peaks recorded from the *ex-vivo* tissue sections, with components including amide I and III proteins, collagen, elastin, phenylalanine, and fatty acids being detected from the whole intact spleen and liver. These peaks were also observed *ex-vivo* for both organs highlighting the capability of the instrument, when focussed correctly, to hit the target organ and not just gain signal from the surface layer which in this case would have been mouse skin. However, with the small data set collected in this study no statistically relevant separation in the PCA model was observed.

As discussed previously, the Raman imaging technique used in this study had a short penetration depth and would not be suitable for *in-vivo* diagnostics moving on from small animal models. However, with the development of SORS techniques it may be possible to gain biochemical information from millimetre depths *in-vivo* in the near future. A further consideration to be made if Raman spectroscopy could ever be employed to detect tissue burden in cerebral malaria cases would be the ability to penetrate through the skull and into the delicate microvasculature of the brain to gain Raman spectra. Investigations have been carried out into gaining compositional information from within bone material using SORS.<sup>123,124</sup> Sharma *et al.* have also shown the ability of surface enhanced SORS to measure spectra from tissue through varying thicknesses of bone (3 – 8 mm).<sup>125</sup> However, this was gained through enhancement with nanoparticles and would not be suitable for most *in-vivo* investigations.

Overall, this approach demonstrates the potential use of Raman spectroscopy to provide detailed chemical information from both malaria parasite infected and control tissue. By interrogating the tissue with two laser excitations complimentary information about the samples was collected. From the resonant 532 nm data spectra centred mainly around changes to Hb levels upon infection and the accumulation of

Hz within the infected tissue was detectable. Whereas, by studying the biological information gained from a 785 nm excitation the effect *P. berghei* infection had on other components, that were previously masked by the strong heme-resonant signals, was discovered. With regards to the *ex-vivo* tissue sections, when this label-free Raman imaging was coupled with PCA, discrimination due to infection burden was achieved between the *P. berghei* infected spleen sections and the non-infected controls.

## 4 Lateral flow assay and 3D-paper-based microfluidic device

---

### 4.1 Introduction

The first step in treating a disease is being able to detect it quickly and effectively. To meet this aim, antigen-detecting RDTs are typically employed as mentioned previously (Section 1.3.4). A typical substrate material for RDTs is paper and related porous hydrophilic materials. Paper has many advantages over traditional device materials including power-free fluid transport *via* capillary action and the ability to store reagents in active form within its fibre network.<sup>126</sup> This chapter focuses on the SERS detection of the *P. falciparum* specific antigen, HRP-II, using a traditional lateral flow assay platform and a 3D printed paper-based microfluidic device.

#### 4.1.1 Antibodies

Antibodies, also known as immunoglobulins (Ig), are a group of glycoproteins typically produced by plasma cells in an immune response to the introduction of foreign pathogens, such as bacteria and viruses.<sup>127</sup> They can be divided into five major classes (IgA, IgD, IgE, IgG, and IgM) which can then be further grouped into subclasses (IgG<sub>1</sub>, IgG<sub>2</sub> etc.). IgG is the predominant class present in human serum, constituting ~75 % of total serum Ig.<sup>128</sup>

IgGs consist of four polypeptide chains, two small light chains and two large heavy chains, linked together by several disulphide bonds to form an antigen-binding fragment (F<sub>ab</sub>) and a crystallisable fragment (F<sub>c</sub>) (Figure 4.1).<sup>129</sup> The two identical heavy chains have a molecular weight of around 50 kDa and the two light chains about 25 kDa.<sup>130,131</sup>

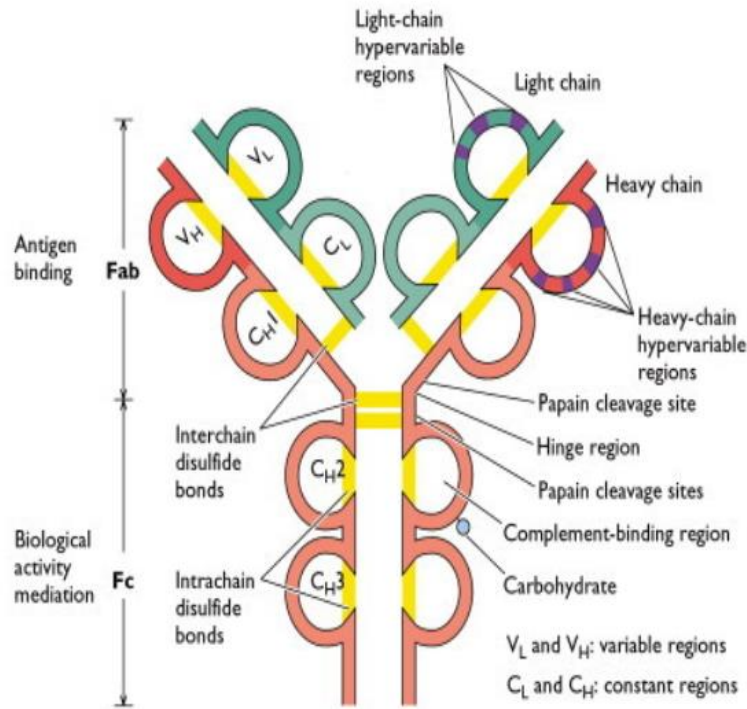


Figure 4.1 Structure of an IgG antibody.<sup>132</sup>

The F<sub>ab</sub> region consists of one constant and one variable domain of the heavy and light chain, respectively. It is the variable region of the light chain which is unique to an antibody due to its variable amine terminated paratope, which binds to the epitope of its target antigen. Whereas, the F<sub>c</sub> in the tail region of the antibody is composed of the heavy chains. This is known as the constant region and is the same within each class of antibody.<sup>130</sup>

Each tip of the “Y” of an IgG antibody contains a paratope (lock) that is specific to a particular epitope (key) on an antigen.<sup>131</sup> The specific association of antibodies and antigens is based on weak, non-specific molecular forces (hydrogen bonds, hydrophobic interactions, electrostatic forces, and Van der Waals forces) therefore, all antigen-antibody binding is reversible.<sup>127,132</sup>

Antibody-antigen binding complexes can be easily detected using a lateral flow immunoassay, which is a commonly employed method for the screening and detection of biomarkers.

#### 4.1.2 Lateral flow immunoassays

Lateral flow immunoassays or immunochromatographic assays are paper-based platforms for the detection of analytes in complex mixtures.<sup>133</sup> These devices have high sensitivity and selectivity and are designed for single point of care use, often with a simple on/off signal.<sup>134</sup> A typical lateral flow rapid test strip consists of four basic components<sup>134,135</sup> (Figure 4.2):

1. Sample pad – an absorbent pad that is placed into the test sample.
2. Conjugate pad – area where antibodies specific to the target antigen that have been conjugated to coloured particles, typically Au nanoparticles, are deposited.
3. Reaction membrane – typically a nitrocellulose membrane onto which capture antibodies for the target analyte are immobilised to create a test line. A control line is also present above the test line.
4. Wicking pad – a further absorbent pad that wicks away excess reagents and prevents backflow of the liquid.

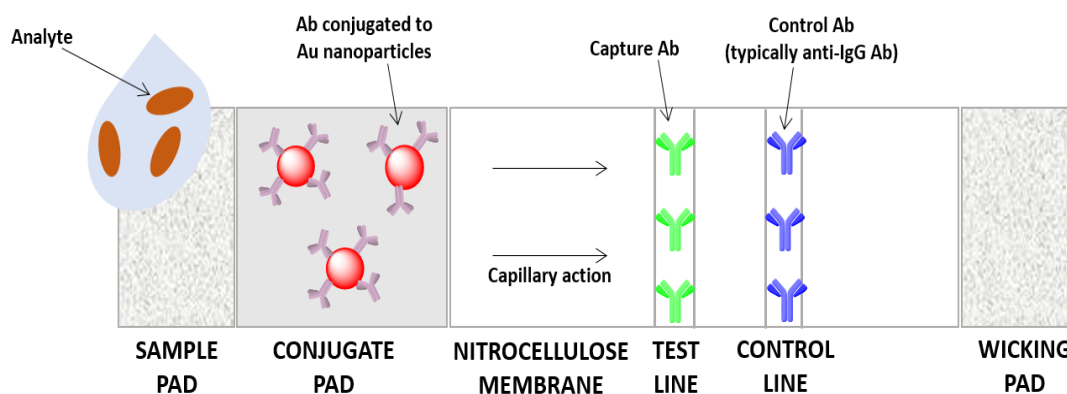


**Figure 4.2** Schematic illustration of the principle components that make up a basic lateral flow strip. The four basic components are (1) Sample pad, (2) Conjugate pad, (3) Nitrocellulose membrane, and (4) Wicking pad. Strips are then mounted on backing card.

Within the literature, these rapid tests have been used to screen for pathogens,<sup>136</sup> toxins in foodstuff,<sup>137,138</sup> water pollutants,<sup>139,140</sup> and animal diseases.<sup>141</sup> Although these strips are attractive biosensing tools for these applications due to their low cost and ease of use, they can suffer from limitations in terms of detection sensitivity and limited quantification capability.<sup>134</sup> To tackle these problems, methods have

developed to create SERS-based lateral flow assays for highly sensitive and rapid detection of target biomarkers. Blanco-Covian *et al.*<sup>142</sup> developed an antibody based SERRS-tag as a labelled probe on a lateral flow device for the ultrasensitive detection of pneumolysin. Their SERRS-based work achieved a limit of detection of 1 pg/mL that outperformed previous literature reports for pneumolysin detection with the same system: 0.6 ng/mL using an electrochemical immunosensor<sup>143</sup> and 5.5 pg/mL *via* a chemiluminescent immunoassay.<sup>144</sup> The ability of SERS-based lateral flow assay platforms to be multiplexed has also been shown by Wang *et al.*<sup>145</sup> This work achieved simultaneous detection of dual DNA biomarkers with much higher sensitivity than previously reported values using an aggregation-based colorimetric method. Coupling lateral flow immunoassays with SERS detection methods have been shown to give very sensitive analyte detection that can compete with current detection methods.

The area of lateral-flow immunoassays has been very well studied, with many more examples of these devices being coupled with SERS.<sup>146–148</sup> A growing area of research that is becoming an attractive alternative for point-of-care diagnosis are three-dimensional paper-based devices that use a combination of lateral and vertical flow.

#### *4.1.3 Microfluidic paper-based devices*

Microfluidic paper-based analytical devices ( $\mu$ PADs) are a relatively new class of point-of-care diagnostic tests that present a promising alternative to traditional laboratory methods and current RDTs (lateral flow strips) for diagnosing disease, particularly in resource-limited environments.  $\mu$ PADs are simple and portable platforms<sup>149</sup> that have low consumption levels of reagents and analytes, requiring only small microlitre volumes of target sample.<sup>150,151</sup> A further advantage of  $\mu$ PADs is that, unlike conventional microfluidic devices, there is no need for mechanical components, external pumps or controllers, as fluid movement through the device is *via* capillary action.<sup>149,152</sup>

Whitesides and co-workers first reported the simple method for patterning paper into hydrophilic channels bounded by hydrophobic barriers in 2007 for the detection



of glucose and proteins in urine.<sup>152</sup> This fundamental principle of creating fluidic channel networks continues to be applied within healthcare-related diagnostics,<sup>153,154</sup> and within other research fields such as environmental metal contamination,<sup>155,156</sup> and food and water screening methods to detect bacteria.<sup>157,158</sup> A schematic of a hydrophilic  $\mu$ PAD channel with its hydrophobic barriers is shown in Figure 4.3.

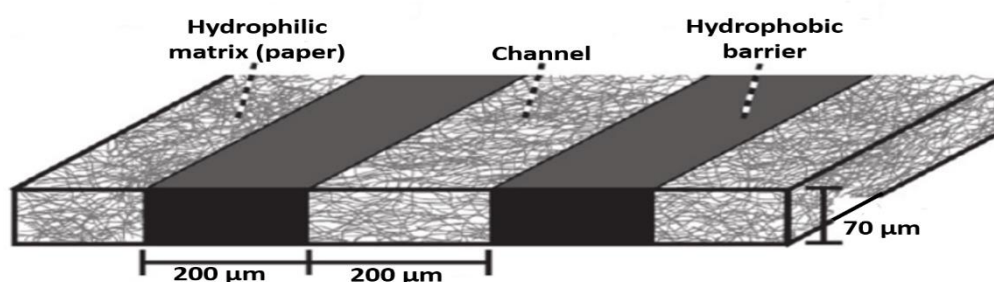


**Figure 4.3** A schematic of a paper-based microfluidic channel. The channel comprises a porous matrix of hydrophilic cellulose fibres (e.g. Whatman chromatography paper) that wick fluids along the length of the channel. The sides of the channel are bounded by hydrophobic barriers. The height of the channel is defined by the thickness of the paper and the resolution of the hydrophobic barriers are defined by the method of patterning employed.<sup>150</sup> Reproduced from Martinez, A.W., et al., *Diagnostics for the Developing World: Microfluidic Paper-Based Analytical Devices*. Analytical chemistry, 2010, **82**(1), 3-10 with permission of The Royal Society of Chemistry.

Several techniques have been reported over the years to fabricate  $\mu$ PADs such as photolithography,<sup>152,159,160</sup> inkjet printing,<sup>161–163</sup> wax printing,<sup>153,164,165</sup> and chemical vapour deposition.<sup>149</sup> Each technique has its own advantages and drawbacks, however, the device used within this project was fabricated *via* a wax printing method and so this technique will be discussed further.

The wax-printing fabrication process involves two simple core steps: (i) printing desired wax patterns on the surface of the paper, and (ii) melting the wax into the paper to form complete hydrophobic barriers.<sup>164</sup> This process is fast,<sup>164</sup> inexpensive,<sup>126</sup> and well-suited for producing large numbers of  $\mu$ PADs in a single batch.<sup>166</sup>

These devices have also been extended from simple single layer channels to 3D devices with more complex microfluidic paths, by stacking layers of patterned paper. They distribute fluids both vertically and horizontally and allow controlled mixing of different components on each layer. The first 3D  $\mu$ PADs were also reported by Whitesides and co-workers,<sup>159</sup> who stacked individual, photolithographically patterned 2D  $\mu$ PADs together using double-sided tape. Since then the use of 3D  $\mu$ PADs has grown and has highlighted their ability to detect an array of analytes in both singleplex and multiplex formats. Schonhorn *et al.*<sup>167</sup> reported the development and application of a 3D layered  $\mu$ PAD for the detection of a pregnancy biomarker, human chorionic gonadotropin, in buffer and urine. This singleplex sandwich immunoassay showed that the visible colour produced by the Au colloidal conjugates was proportional to the concentration of biomarker in a sample and results could be both qualitative (by eye) and quantitative (colourimetric image analysis). This same device has since been modified to allow multiplex detection of disease biomarkers.<sup>168</sup>

Typically, these  $\mu$ PADs use Au nanoparticles due to their strong colour and colourimetric analysis can be used to quantify the results. However, as with lateral flow immunoassays, research has been carried out into coupling these  $\mu$ PADs with SERS detection.

This chapter investigated the application of SERRS-based lateral-flow immunoassays and SERRS-based 3D  $\mu$ PADs for the sensitive detection of the unique *P. falciparum* biomarker, HRP-II. Comparison with current antigen detection limits was carried out to assess if point-of-care devices coupled with the SERRS detection could improve the sensitivity. SERRS limits of detection obtained from each platform were also compared, along with analysing the devices with a more common colorimetric technique.

## 4.2 Results and discussion

### 4.2.1 Au nanoparticle synthesis and characterisation

Citrate capped Au nanoparticles were synthesised *via* a standard method first devised by Turkevich in 1951<sup>2</sup> and later refined by Frens.<sup>10</sup> This involved the reduction of chloroauric acid (HAuCl<sub>4</sub>) in the presence of citrate and heat. As well as being the reducing agent, the citrate also acted as a stabilising agent, providing a negative surface layer that prevented aggregation of the nanoparticles due to electrostatic repulsion. The Au nanoparticles were characterised using extinction spectroscopy, dynamic light scattering (DLS), zeta measurements, and scanning electron microscopy (SEM) to evaluate their quality. The results from the extinction spectroscopy and SEM are shown in Figure 4.4.

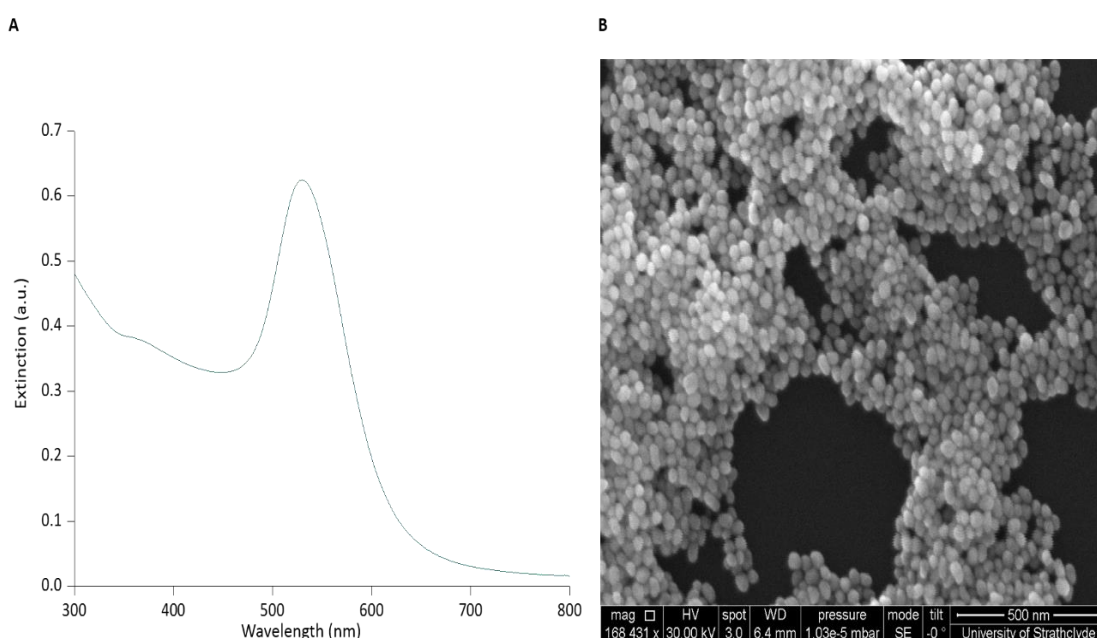


**Figure 4.4** (A) Extinction spectrum and (B) SEM image of citrate reduced Au nanoparticles (scale bar is 500 nm).

As observed in Figure 4.4(A), the Au nanoparticles had an LSPR at 529 nm, a typical value expected for Au colloid of this size.<sup>169</sup> The extinction spectrum also suggested that the nanoparticles were monodispersed, which was achieved by calculating the full width half maximum value (FWHM) of the LSPR peak. The smaller the LSPR FWHM value is, the more monodispersed the nanoparticles (<100 nm is typically

acceptable).<sup>170,171</sup> The FWHM of the LSPR in this case was 59 nm, indicating monodispersity.

The Au colloid was then analysed using DLS to determine the particle size and zeta potential of the particle surface. These measurements showed the nanoparticles to be  $52.7 \pm 0.7$  nm in diameter, with a zeta potential of  $-40.2 \pm 2.9$  mV. This demonstrated that the nanoparticles were stable as it has been reported that nanoparticles with a zeta potential lower than -25 mV have high degrees of stability.<sup>172</sup> The concentration of the nanoparticles was 0.1 nM. This was calculated using the Beer-Lambert law and a molar extinction coefficient of  $1.19 \times 10^{10} \text{ M}^{-1} \text{ cm}^{-1}$ .<sup>173</sup>

To further confirm the monodispersity and the size of the nanoparticles, SEM images were obtained by Dr Samuel Mabbott at the University of Strathclyde. The SEM image in Figure 4.4(B) indicated that the nanoparticles were spherical and had a size of  $49.7 \pm 4.4$  nm. Due to the successful synthesis of Au colloid, conjugation of antibodies to the nanoparticles was then carried out.

#### 4.2.2 Antibody conjugated Au nanoparticles

There are various conjugation methods that can be used to functionalise Au nanoparticles with antibodies (Figure 4.5).<sup>174</sup>

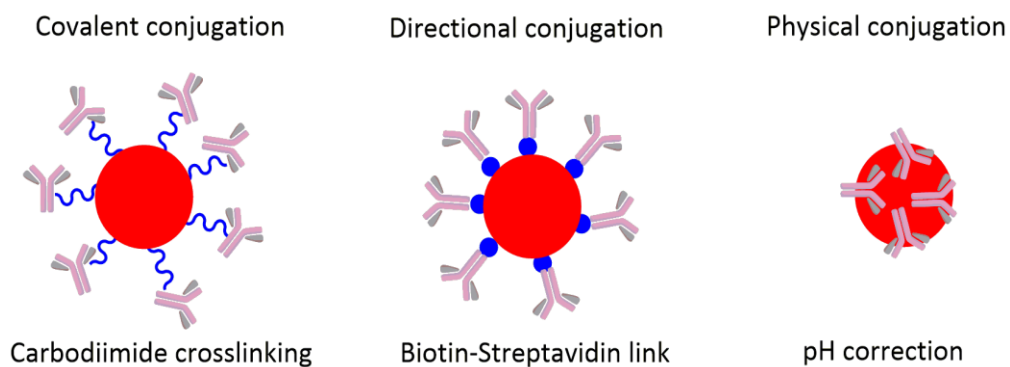


**Figure 4.5** Schematic diagram indicating how antibodies can be functionalised and orientated on a nanoparticle surface.

As shown in Figure 4.5, antibodies will orientate on the nanoparticle surface differently depending on what conjugation method is chosen. This will leave different

areas of the antibody exposed. Covalent conjugation most commonly makes use of carbodiimide crosslinking chemistry, allowing amine groups on the antibody to bind to the carboxylic acid groups on a carboxyl-polyethylene glycol-thiol (CT(PEG)<sub>n</sub>) molecule. Following this the antibody can be functionalised to the Au nanoparticles *via* the strong binding affinity between the Au surface and the thiol groups on the PEG molecule. This orientation allows the paratopes to be free to bind to an antigen, if the covalent bond doesn't involve binding to an amine in that region.<sup>130</sup> Directional conjugation uses streptavidin-coated nanoparticles that can form a strong bond to a biotinylated antibody. As the biotin is on the antibody Fc region, the streptavidin-biotin bond will leave paratopes free for binding.<sup>175</sup> Finally, physical adsorption involves altering the pH of the nanoparticle solution so that it is at or near to the isoelectric point of the antibody, allowing hydrophobic interactions to occur between the protein and the nanoparticle surface.<sup>174</sup> However, with pH correction methods, the orientation of the antibody on the surface is unknown, which may lead to paratopes being blocked and a subsequent decrease in antigen binding efficiency. In this work, covalent conjugation was utilised to attach HRP-II mouse monoclonal antibodies to spherical Au nanoparticles.

#### *4.2.2.1 MGITC functionalisation to Au nanoparticles*

A Raman reporter was needed in this work to produce a unique Raman fingerprint spectrum to indicate detection of the target analyte. The signal intensity of the reporter could then be correlated to the concentration of target detected. A good Raman reporter molecule should exhibit a strong and distinctive SERS signal, attach strongly to the nanoparticle surface, and ideally possess unique Raman peaks that would allow multiplexing with other reporters. The Raman reporter chosen for this research was malachite green isothiocyanate (MGITC). Au nanoparticles were functionalised with MGITC dye (final concentration of 100 nM) as the Raman reporter. Characterisation of the dye-coated Au was carried out using SERRS and extinction spectroscopy (Figure 4.6).

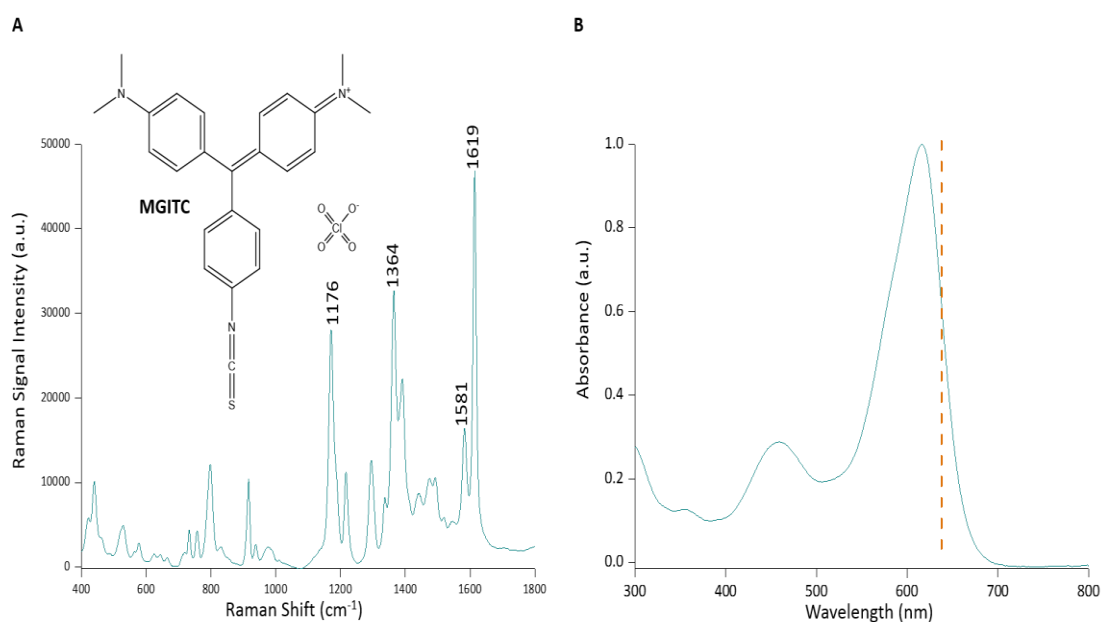


**Figure 4.6** (A) Structure (inset) and SERRS spectrum of MGITC, with the most prominent Raman peaks labelled. MGITC was attached to Au nanoparticles at a final concentration of 100 nM. (B) UV-visible absorption spectrum of MGITC. The dashed line indicates the 638 nm excitation laser line that was used for analysis. SERRS spectrum is the average of 3 spectra recorded with 638 nm laser excitation, 26.7 mW laser power, 1 s acquisition time. Stock MGITC (1 mM) was diluted 1 in 80 (10  $\mu$ L MGITC in 790  $\mu$ L dH<sub>2</sub>O). Spectrum was normalised to 1 for clarity.

An isothiocyanate group and large conjugated system within the dye structure allowed it to form strong thiol bonds with the Au for attachment and resulted in well resolved Raman peaks (Figure 4.6(A)). As shown in the MGITC absorbance spectra (Figure 4.6(B)) it had an absorbance maxima at  $\sim$ 617 nm which allowed a laser line to be chosen to give SERRS rather than SERS. An excitation wavelength at 633 nm was chosen for analysis of the lateral flow immunoassays and 638 nm for interrogation of 3D  $\mu$ PADs so that resonance enhancement of the dye signal could be obtained. The two laser excitation wavelengths varied slightly (by 5 nm) as two different Raman spectrometers were used.

#### 4.2.2.2 Carbodiimide crosslinking conjugation

Carbodiimide crosslinking conjugation was carried out using an off-nanoparticle approach as it allowed a simple one-pot reaction of the carbodiimide chemistry to occur before the nanoparticles, pre-functionalised with Raman reporter, were added. This involved first forming an amide bond between the carboxyl groups on CT(PEG)<sub>12</sub> and the amine groups on the antibody. This was then mixed with a dye-coated nanoparticle solution to allow terminal thiol groups on PEG to bind to the Au nanoparticle surface (Figure 4.7). Carbodiimide compounds provide a versatile method for crosslinking to carboxylic acids. The most commonly used is the water-soluble 1-ethyl-3-(3-dimethylaminopropyl) carbodiimide (EDC). It reacts with the carboxylic acid groups, such as those on CT(PEG)<sub>n</sub>, to form an O-acylisourea intermediate that is easily displaced by nucleophilic attack from primary amine groups within the reaction mixture. However, the O-acylisourea intermediate is unstable in aqueous conditions and failure to react with an amine results in hydrolysis and subsequent regeneration of the carboxyl with release of an N-unsubstituted urea. If this reverse process occurs, a decrease in the efficiency of the coupling follows. To prevent this from happening, the stability of the O-acylisourea intermediate is increased through the addition of water-soluble sulfo-N-hydroxysuccinimide (sNHS). EDC couples sNHS to the carboxyl group forming an amine-reactive sNHS ester that is considerably more stable than the initial intermediate and allows successful conjugation to primary amines.<sup>174,176</sup>

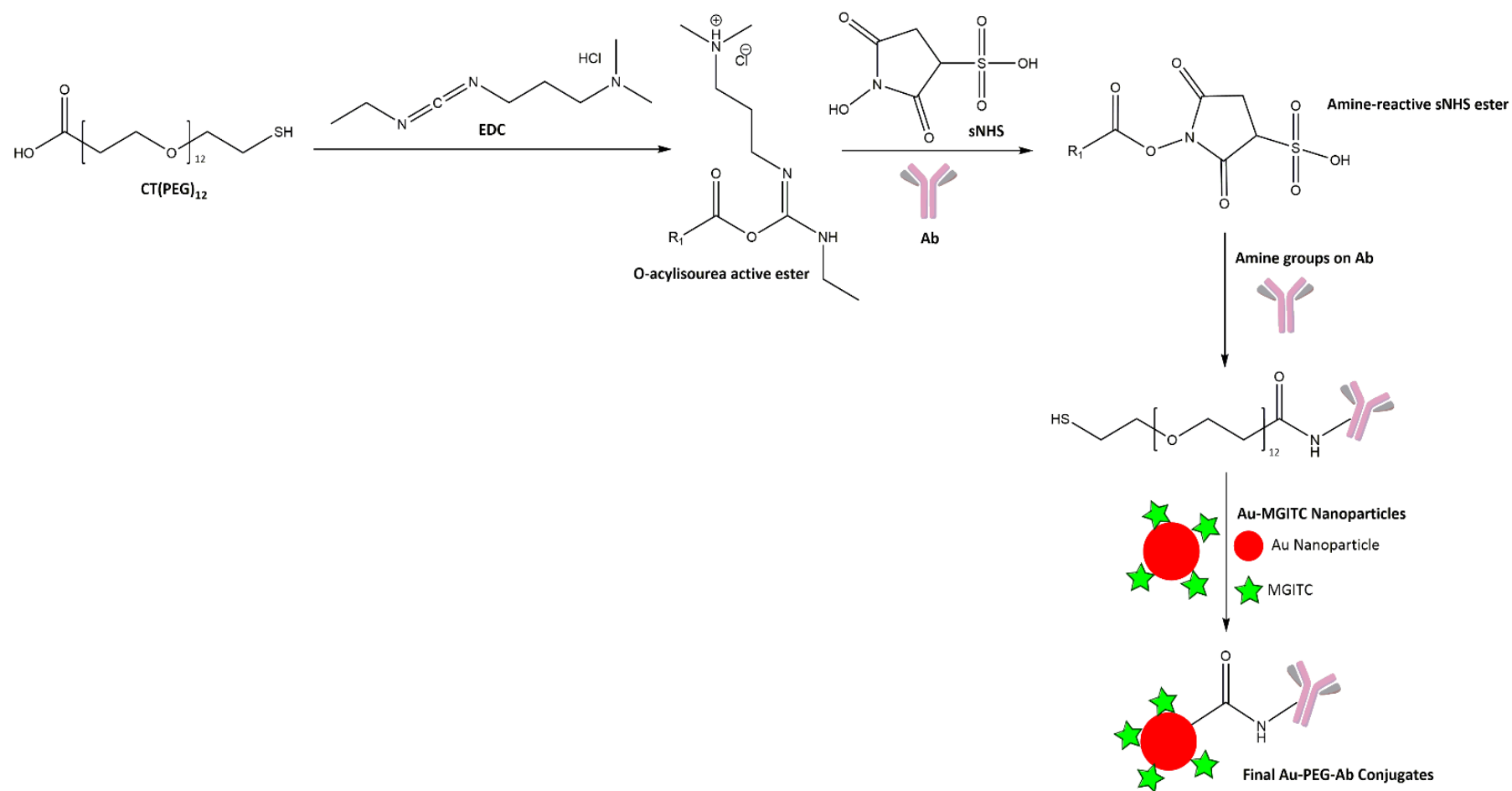


**Figure 4.7** Schematic representation of the off-nanoparticle carbodiimide crosslinking chemistry. The process creates an amide bond between the carboxylic acid groups on the PEG and amine groups on the antibody. This is then added to a solution of MGITC-coated Au nanoparticles to allow the terminal thiol groups of the PEG to bind to the Au nanoparticle surface.



CT(PEG)<sub>12</sub> was first mixed in excess (final concentration 40  $\mu$ M) with EDC (1 mg/mL), before being added to a sNHS (1 mg/mL) / monoclonal mouse HRP-II (malaria) antibody (final concentration 10  $\mu$ g/mL) mixture and left to shake overnight. The PEG concentration was calculated to give theoretical monolayer coverage on the Au nanoparticles at the later stage of the conjugation. Following formation of the amide bond between the PEG carboxyl groups and antibody amines, this mixture was added 1:1 to MGITC-Au nanoparticles (0.1 nM) to give a final antibody concentration of 5  $\mu$ g/mL. This was left to incubate on a shaker for 2 hours to allow binding of the Ab-PEG to the Au. A centrifugation step was carried out to remove any unreacted Ab-PEG and any MGITC that may have been displaced by the PEG. The conjugate pellet was then reconstituted in 10 mM PB + 0.1 % bovine serum albumin (BSA) to the desired concentration for either the lateral flow assay or 3D  $\mu$ PAD.

Characterisation of the Au-PEG-Ab conjugates was then carried out using extinction spectroscopy, DLS, gel electrophoresis, and lateral flow. The extinction spectra (Figure 4.8(A)) showed a red-shift in LSPR with each layer that was added to the Au nanoparticles, moving from 529 nm for bare Au to 534 nm for the final Au-PEG-Ab conjugates, indicating an increase in size and therefore successful conjugation to the nanoparticle surface. Furthermore, the final conjugate extinction spectrum did not show any additional peaks in the higher wavenumber region that may indicate particle aggregation. This observation suggested that the Au nanoparticles were stable after the addition of the PEG-Ab layer. DLS measurements also showed successful conjugation (Table 4.1), with the nanoparticles increasing in size from the bare Au to the final conjugate mixture, along with a more positive zeta potential for the Au-PEG-Ab layers compared to the bare Au nanoparticles (-36.60 vs. -40.20 mV, respectively) implying Ab was attached.

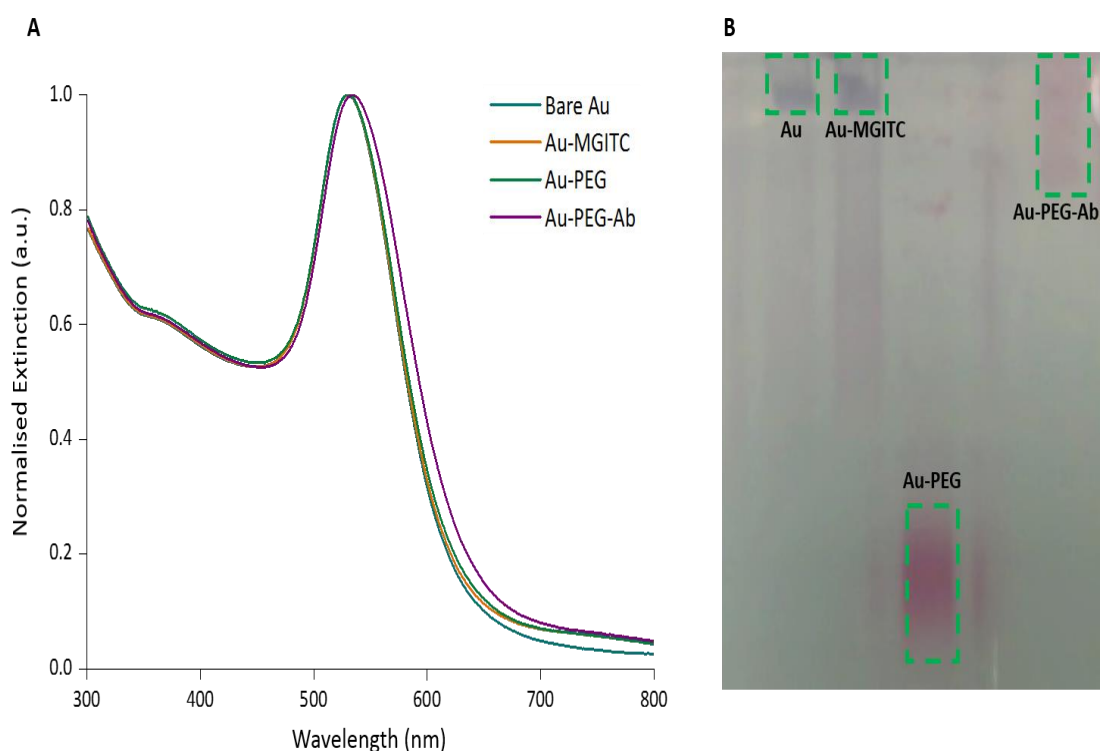


**Figure 4.8** (A) Extinction spectra of bare Au (blue), Au-MGITC (orange), Au-PEG (green), and Au-PEG-Ab (purple). 80  $\mu\text{L}$  of was diluted in 720  $\mu\text{L}$  of dH<sub>2</sub>O for analysis. Spectra were normalised to one for clarity and ease of comparison. (B) Image of gel showing the distance travelled by Au, Au-MGITC, Au-PEG, and Au-PEG-Ab conjugates.

**Table 4.1** Table showing the LSPR, average size, and average zeta potential measurements for bare Au, Au-MGITC, Au-PEG, and Au-PEG-Ab conjugates.

| Sample           | LSPR (nm) | Average Size (nm) | Average Zeta (mV) |
|------------------|-----------|-------------------|-------------------|
| <b>Bare Au</b>   | 529       | 52.7 $\pm$ 0.7    | -40.2 $\pm$ 3.0   |
| <b>Au-MGITC</b>  | 529       | 57.9 $\pm$ 1.0    | -36.0 $\pm$ 0.5   |
| <b>Au-PEG</b>    | 530       | 60.7 $\pm$ 0.5    | -43.7 $\pm$ 1.5   |
| <b>Au-PEG-Ab</b> | 534       | 91.4 $\pm$ 2.9    | -35.6 $\pm$ 1.9   |

Due to the increase in size observed moving from each conjugation layer (Au to Au-PEG to Au-PEG-Ab), these samples could also be separated using gel electrophoresis. Larger samples would be expected to travel slower through the gel compared to smaller samples that can travel faster through the porous gel matrix. Figure 4.8(B)

illustrates how each sample behaved in the agarose gel, depending on the coating present. Both bare Au and Au-MGITC aggregated in the well (dark purple colour) due to the loading buffer as the nanoparticle surface was not protected. Whereas the Au-PEG (used as control for Ab binding) moved much further through the gel due to its smaller size compared to the Au-PEG-Ab which travelled a shorter distance. This result gave a strong indication that the antibody had bound to the nanoparticles.

A final method carried out to confirm successful antibody conjugation was a simple lateral flow spot test. A solution of HRP-II antigen (0.5  $\mu$ L, 100  $\mu$ g/mL) was spotted onto the nitrocellulose strip, along with anti-mouse IgG (0.5  $\mu$ L). Concentrated conjugate mixture (10  $\mu$ L) was added to running buffer and the dried strips dipped into this. Figure 4.9(A) illustrated that the conjugates only bound when the specific HRP-II antigen was spotted (compared to when none was spotted). The excess conjugate was then captured by the anti-IgG control on both strips. Binding of antibody conjugates to the HRP-II antigen and at the control spots was clearly evident as red spots. Interrogation of the bound HRP-II-antibody conjugates with a 633 nm laser produced the characteristic SERRS spectrum of MGITC (Figure 4.9(B)) highlighting that the conjugates would give a strong signal following binding to their target.

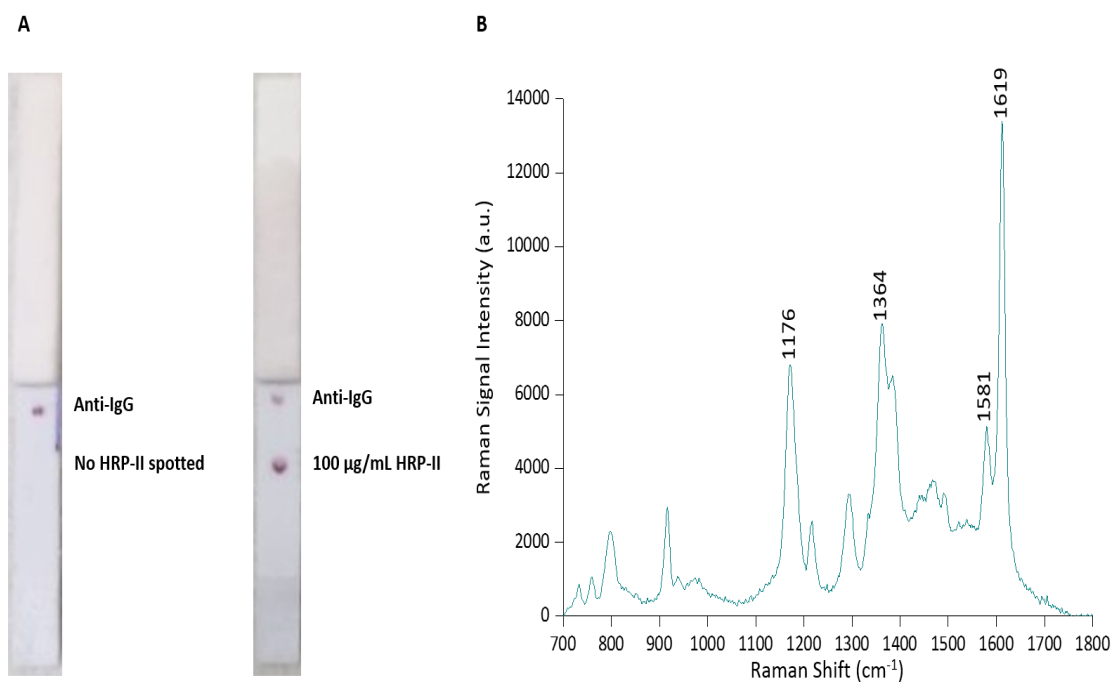


**Figure 4.9** (A) Images of lateral flow strips. When no HRP-II antigen was spotted, no binding of the Au-PEG-Ab conjugates occurred. However, when 100 µg/mL of antigen was spotted on the strip, binding between the HRP-II and the malaria HRP-II monoclonal Ab on the conjugates occurred and a clear spot was observed. Anti-mouse IgG antibody was used as a control line in both strips. (B) SERS spectrum of MGITC recorded from the 100 µg/mL HRP-II spot on the lateral flow strip highlighting successful conjugation of the Raman reporter molecule and the detection Ab onto the Au nanoparticles. The most prominent Raman peaks of MGITC are also highlighted. SERS spectrum is the average of 5 replicate spectra from the 100 µg/mL HRP-II spot. Spectra were collected with a 633 nm laser excitation, 4 mW laser power, and 3 s acquisition time. Spectra were baseline corrected and averaged using Matlab R2013a software.

The characterisation steps completed for the antibody-conjugated-nanoparticles gave a strong indication that antibody had been successfully bound to the Au and that the MGITC Raman reporter could still produce a strong SERS signal. From the extinction spectrum, the conjugates showed no aggregation and were stored in buffer with BSA for added stability. For both diagnostic devices studied in this work, the same conjugates were used as SERS tags, with the final concentration deposited being the only variation between the two.

#### 4.2.3 Development of a lateral flow immunoassay for HRP-II detection

HRP-II specific antibody functionalised SERRS tags were tested for the detection and quantification of HRP-II in a lateral flow immunoassay by SERRS and *via* a more traditional image analysis technique. The principle of the SERRS-based lateral flow assay used in this work was based on a sandwich immunoassay (Figure 4.10).

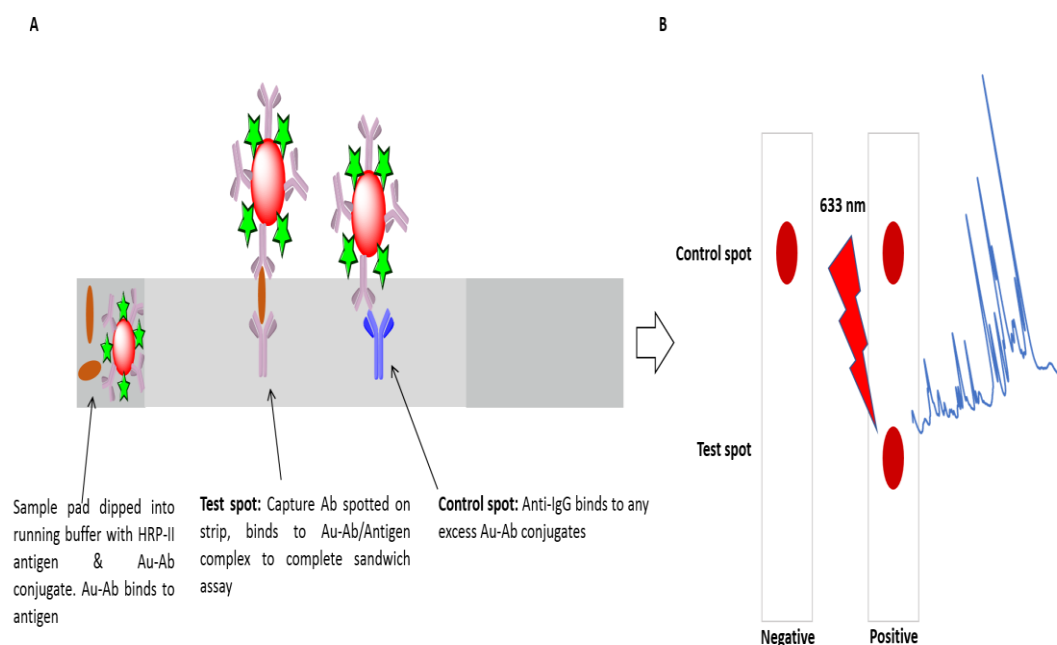


**Figure 4.10** (A) Schematic illustration of the SERRS based sandwich lateral flow immunoassay (B) Qualitative analysis of the strip, where only one red spot is observed in the control zone when no HRP-II is present (negative) and two spots appear in the presence of HRP-II (positive). SERRS analysis of the test spot with 633 nm laser excitation produces characteristic MGITC dye spectrum and allows quantitative analysis.

HRP-II (malaria) mouse monoclonal antibody (capture antibody) and anti-mouse IgG antibody were immobilised on the strip as test and control spots, respectively (Figure 4.10(A)). In this work the capture antibody used was the same as the detection antibody conjugated to the SERRS tags as it was recommended for both positions and was able to self-pair.<sup>177</sup> Antigen (at a calculated final concentration), Ab-conjugated-Au-MGITC SERRS tags, and the running buffer were added to the sample wells and gently shaken for 15 minutes before the lateral flow strips were added. Due to capillary action, the sample mixture migrated along the strip before being

immobilised by the capture antibody at the test spot. Any excess of the SERRS tag continued along the membrane before being captured by the anti-mouse IgG antibody. The accumulation of the Au-Ab conjugates in either the test or control spots produced the characteristic dark red colour, with the colour intensity at the test area being related to the concentration of the target analyte. Two spots appeared in the presence of HRP-II indicating a positive test, whereas, only one spot was observed in the control zone when no antigen was present (Figure 4.10(B)). To record a SERRS response from the immunoassay, the test spots were analysed using a confocal Raman system equipped with a 633 nm laser line excitation. The characteristic spectrum of MGITC dye could then be monitored and the Raman peak at  $1619\text{ cm}^{-1}$  was used for SERRS quantitation.

However, before quantitative analysis could take place the concentration of both the capture antibody that was spotted on the strips and the Au-Ab conjugates used had to be determined. Concentrations were chosen based on those that gave the strongest SERRS response but also gave minimal non-specific binding when the blank controls were run.

#### *4.2.3.1 Immunoassay design and SERRS detection*

The nitrocellulose membrane is a very important part of the test system with various capillary flow times being available. This is the time required for a liquid to move along and completely fill a strip of defined length. For this work, a Millipore Hi-Flow Plus membrane was used with a quoted capillary flow time of  $180 \pm 45\text{ sec}/4\text{ cm}$ .<sup>178</sup> This was chosen as it was a slow flow rate which should provide increased sensitivity, particularly when analysing targets at lower concentrations.

Two capture antibody concentrations were considered,  $100\text{ }\mu\text{g/mL}$  and  $300\text{ }\mu\text{g/mL}$ , for the lateral flow immunoassay. To assess these concentrations both were spotted on assembled lateral flow strips ( $0.8\text{ }\mu\text{L}$ ) left to dry and then placed in running buffer containing Au-Ab conjugate and buffer blank (to act as a control when no antigen is present). The same concentrations were spotted on a further 2 strips and run in a

mixture containing target antigen (100 ng/mL final concentration), Au-Ab conjugate and running buffer, to observe binding in the sandwich assay (Figure 4.11).

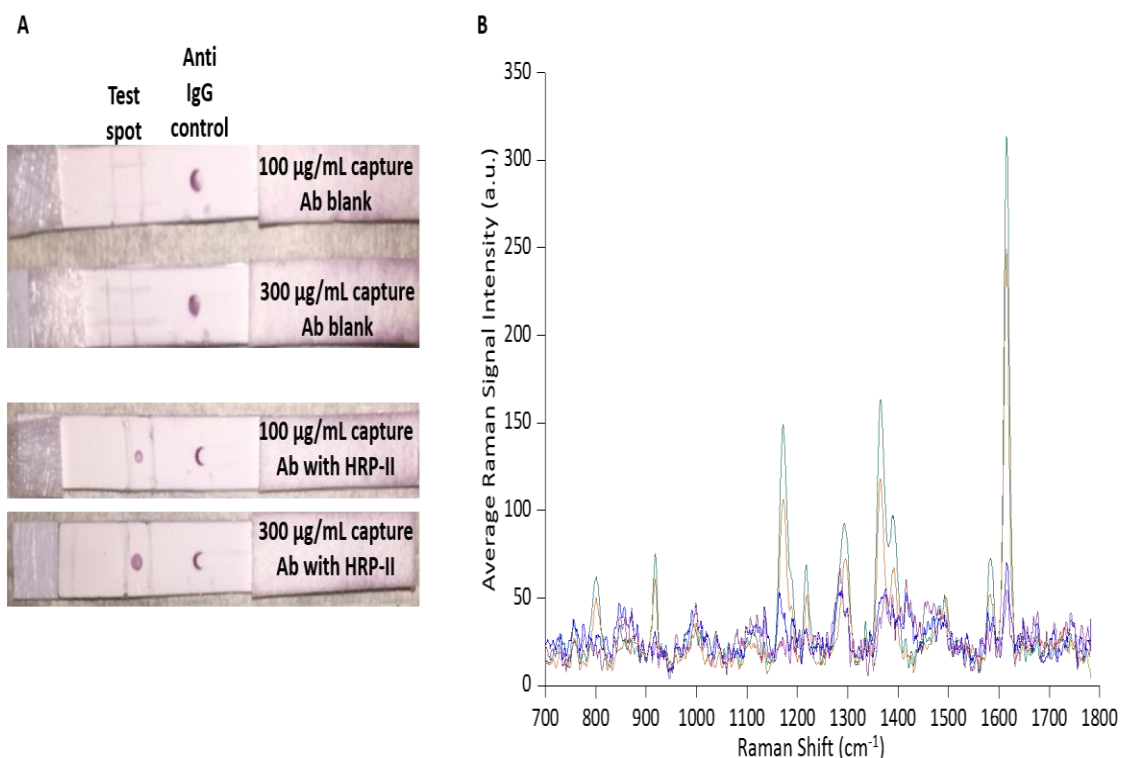


**Figure 4.11** Determining capture Ab concentration (A) Images of the lateral flow strips that have been treated with either 100 µg/mL or 300 µg/mL of capture Ab. The top 2 strips were run as blanks to assess any non-specific binding when target antigen was not present. From the images, no clear spot was visualised in either blank. 100 ng/mL HRP-II was also added, and 2 different strips run with the 2 capture Ab concentrations. A much darker spot formed with the 300 µg/mL capture Ab strip indicating greater binding of the conjugates. Anti-IgG was spotted above the capture Ab in each strip to act as a positive control. (B) Average SERRS spectra from the 4 test spots shown in image (A). Conjugate-antigen-capture Ab spot gave the most intense SERRS signal. A slight SERRS response was observed in both blank controls but the intensity was similar in both and much less intense than the positive signals. 100 ng/mL HRP-II + 300 µg/mL capture Ab (cyan), 100 ng/mL HRP-II + 100 µg/mL capture Ab (orange), Blank + 300 µg/mL capture Ab (blue), and Blank + 100 µg/mL capture Ab (purple). Spectra are the average of 50 spectra from each spot, recorded with a 633 nm laser excitation, 0.8 mW laser power, and 6 s acquisition. Spectra were baseline corrected and averaged using Matlab R2013a.

No visual non-specific binding was observed for either capture Ab concentration and a more intense spot resulted with the 300 µg/mL when the strips were run in a sample containing antigen, indicating increased conjugate binding with increased capture Ab. This was confirmed with SERRS analysis of each spot, which showed the most intense SERRS signal for the HRP-II bound to 300 µg/mL capture spot. Although no coloured spot was observed for the blank controls, a slight SERRS signal was recorded for each. This was similar in intensity for both capture Ab concentrations and because of this and the increased signal in the positive sample, 300 µg/mL was chosen as the capture Ab concentration going forward

A second condition that was studied was the concentration of the Au-Ab conjugate applied. Following synthesis, the conjugates were diluted to 0.7 nM and 0.4 nM and run on 2 strips with HRP-II (final concentration 100 ng/mL) and 300 µg/mL capture antibody (Figure 4.12).

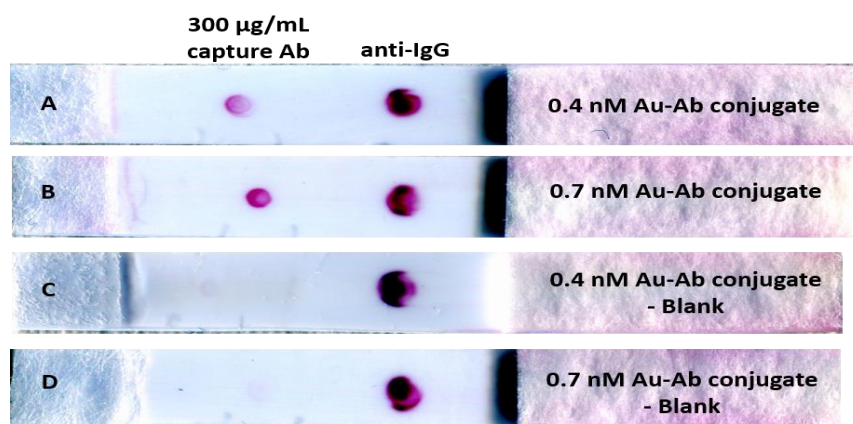


**Figure 4.12** Determining Au-Ab conjugate concentration. (A) Lower concentration of 0.4 nM was run along with HRP-II (final concentration 100 ng/mL) and 300 µg/mL capture antibody. (B) Higher conjugate concentration, 0.7 nM, was run under the same conditions as (A). As expected the higher concentration resulted in increased binding and a brighter spot. (C) 0.4 nM conjugate was run in a blank (no HRP-II) and showed only a slight spot in the capture area. (D) 0.7 nM conjugate was also run in a blank and as with the 0.4 nM only a slight spot was observed. This showed that no significant non-specific binding of the conjugate was occurring on the capture spot at either concentration. Anti-IgG was spotted as a positive control on each lateral flow strip.



As was expected, the higher conjugate concentration gave a more intense spot colour, indicating a greater amount of binding in the sandwich assay. When a blank control, with no antigen present, was run in the presence of both 0.4 nM and 0.7 nM conjugates only a faint spot was observed on each capture spot indicating that at either concentration, no obvious non-specific binding was occurring. Consequently, the higher Au-Ab conjugate concentration of 0.7 nM was chosen for use in the lateral flow sandwich immunoassay as it would result in a more intense SERRS response. With these conditions set, quantitative analysis of the target HRP-II antigen could be carried out.

#### *4.2.3.2 Quantitative analysis of HRP-II using SERRS*

Initial analysis was carried out using SERRS mapping, with a 633 nm laser excitation line, to gain information from the whole test spot. Heat maps of the signal-to-baseline intensity for the peak at  $1619\text{ cm}^{-1}$  for MGITC were generated and allowed a visual observation of the distribution of the antibody-conjugates on the strip (Figure 4.13). When a high concentration of HRP-II antigen was present ( $1\text{ }\mu\text{g/mL}$ ) a very bright spot was observed, and the Raman spectrum taken from a selected image pixel showed a very intense MGITC signal. Whereas when no HRP-II was added (blank), little signal from the Raman reporter was detected. These initial results were promising as they showed that only slight non-specific binding of the Au-Ab conjugates was occurring when HRP-II was absent. From analysis of the  $1\text{ }\mu\text{g/mL}$  HRP-II heat intensity map (Figure 4.13(A)) it was also clear that binding of the Au-Ab-antigen complex to the capture Ab (spotted on the nitrocellulose) was not homogenous. Some pixels appeared much brighter (white) within the spot indicating more sandwich conjugate had formed in these areas where others were darker (orange) highlighting a decrease in signal-to-baseline intensity of  $1619\text{ cm}^{-1}$  peak.

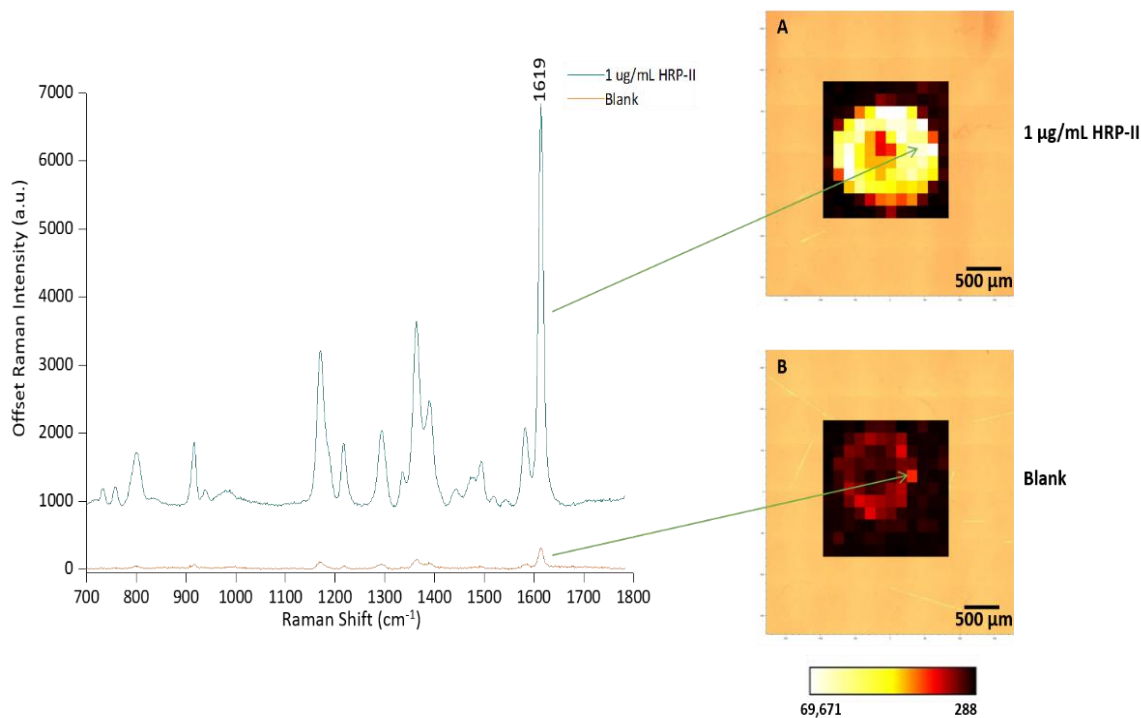


**Figure 4.13** SERRS mapping of test spots. Images are heat intensity maps generated by the signal-to-baseline intensity of the  $1619\text{ cm}^{-1}$  MGITC peak at each pixel. (A) Heat intensity map when  $1\text{ }\mu\text{g/mL}$  HRP-II antigen was present. The arrow points to the pixel on the image where the intense Raman spectrum (blue) originated from. (B) Heat intensity map when no HRP-II was present ( $0\text{ }\mu\text{g/mL}$ , blank). Arrow indicates the pixel where the Raman spectrum (orange) was taken from. Both maps had the same upper and lower intensity limits applied. All SERRS maps were recorded with a  $633\text{ nm}$  laser,  $5\times$  objective,  $0.8\text{ mW}$  laser power, acquisition time  $4\text{ s}$ , and  $150\text{ }\mu\text{m}$  step-size.

Although this method of spot analysis produced easy to interpret heat intensity maps, it took between 10 – 15 minutes to complete each map using a relatively large step-size which meant it was not suitable for high-throughput analysis of lateral flow assays. To make the spot analysis quicker and to gain the most relevant information from the sample under interrogation, single point spectra were collected. Seven HRP-II final concentrations were studied along with a blank control (250, 100, 50, 25, 20, 10, 5, and  $0\text{ ng/mL}$ ), with 20 point spectra being collected from each test spot and taking only  $\sim 3$  minutes per strip to complete. Each concentration was then also studied in triplicate to give a total of 60 spectra for each concentration under investigation. These were then averaged to give a final spectrum for each sample.

Figure 4.14(A) shows images of the lateral flow immunoassay strips in the presence of different concentrations of HRP-II (0 – 250 ng/mL). The presence of the target antigen was confirmed *via* the colour change at the test spot, where capture antibody had been spotted. It was observed that the colour became more intense at higher antigen concentrations as more sandwich conjugate formed. Consequently, at the higher concentrations (250 – 25 ng/mL) the presence of HRP-II could be identified by the naked eye. At concentrations below 25 ng/mL the positive detection of target antigen became more subjective by eye and it was at these concentrations where the use of quantitative SERRS became most important. Also, in all of the lateral flow strips, the control spot showed a reliably uniform colour intensity, regardless of the HRP-II concentration present. The final averaged Raman spectrum for each target concentration studied is shown in Figure 4.14(B). These spectra showed a very clear decrease in Raman signal intensity as the concentration of HRP-II present decreased. Even at the lower antigen concentrations, that were difficult to observe by eye, a strong SERRS signal was recorded allowing differentiation from the blank. This trend was studied further by plotting the  $1619\text{ cm}^{-1}$  peak height against HRP-II concentration (Figure 4.14(C)).

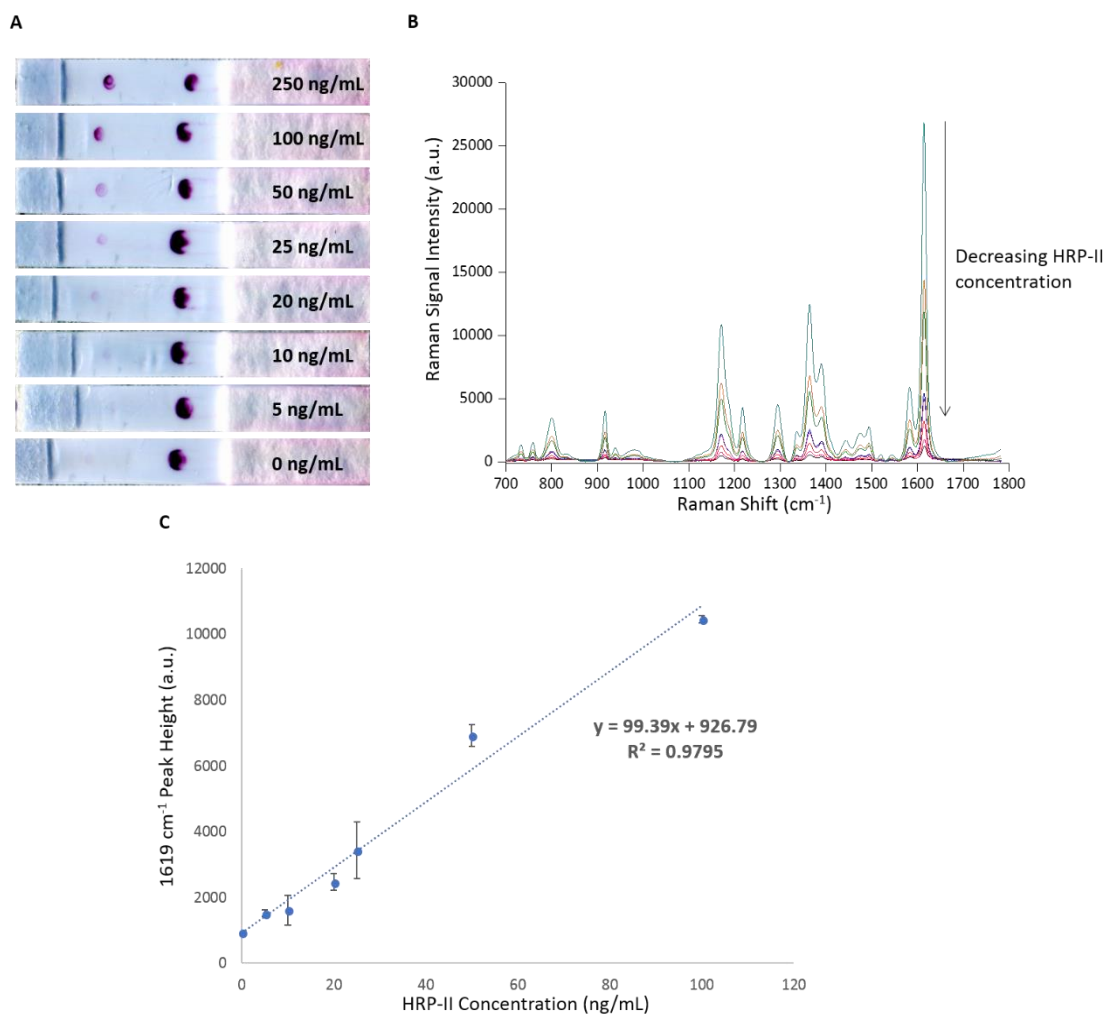


**Figure 4.14** SERRS quantitative analysis of HRP-II detection. (A) Images of one of the lateral flow sandwich assay replicates for HRP-II detection for each antigen concentration. Final antigen concentrations are labelled on each strip, with a decrease in test spot colour intensity as the concentration of HRP-II present decreased. At the lower antigen concentrations (10, 5, 0 ng/mL) the spots were not so visually clear. The control anti-IgG spots were the same intensity for each sample. (B) Average Raman spectrum for each antigen concentration studied: 250 (cyan), 100 (orange), 50 (green), 25 (purple), 20 (blue), 10 (red), 5 (pink), and 0 ng/mL (black). A decreasing trend in Raman signal intensity with decreasing HRP-II concentration was observed. (C) Intensity of 1619 cm<sup>-1</sup> peak height vs. final HRP-II concentrations. The spectra shown are the average of 20 measurements of 3 replicates (60 in total) for each concentration. Errors bars are the standard deviation of the measurements taken. The equation of the line is also shown. Spectra were collected using a 633 nm laser excitation, 0.8 mW laser power, 9 s acquisition time, 5x objective. Spectra had cosmic ray removal and noise filtering algorithms applied to them in Wire 4.2 software, before they were baseline corrected and averaged using Matlab R2013a. 1619 cm<sup>-1</sup> peak heights were calculated using the signal-to-baseline.

Figure 4.14(C) showed a very good linear correlation between Raman peak height and HRP-II concentration with relatively small standard deviations, indicating that the SERRS signals that were obtained between replicates had good analytical reproducibility. This calibration curve was used to calculate a theoretical limit of detection (LoD) for HRP-II using this SERRS-based lateral flow sandwich assay. The LoD was calculated to be 3 times the standard deviation of the blank, divided by the gradient of the straight line (the equation of the straight line is shown in Figure 4.14(C)). This method gave a theoretical HRP-II LoD of 65.3 pg/mL.

Using technical results presented in a World Health Organisation (WHO) report on malaria diagnosis,<sup>179</sup> the antigen concentrations detectable by the lateral flow assay could be converted to an estimated number of parasites per  $\mu\text{L}$ . Clinical ranges of parasitemia can vary depending upon the *Plasmodium* infection. Some patients may appear symptomatic at parasite densities of 100 – 200/ $\mu\text{L}$  (0.002 % parasitemia), while hyperparasitemia in severe non-*falciparum* cases can reach 100,000 parasites/ $\mu\text{L}$  (burden of  $\sim 2\%$ ), and up to 250,000 parasites/ $\mu\text{L}$  (overall burden of 5 %) in severe *P. falciparum* cases.<sup>180</sup> So for a patient sample infected with *P. falciparum* at a total of 200 parasites/ $\mu\text{L}$ , the mean HRP-II antigen concentration was reported to be 15.3 ng/mL. Using these numbers, the lowest detected concentration of HRP-II in this SERRS-based sandwich assay (5 ng/mL) equated to  $\sim 65$  parasites/ $\mu\text{L}$  and the theoretical LoD (65.3 pg/mL) gave less than 1 parasite/ $\mu\text{L}$ . The ‘gold standard’ for malaria diagnosis and quantification of parasitemia is a blood smear. A skilled technician may be able to detect densities as low as 5 – 10 parasites/ $\mu\text{L}$  blood, however, under general field conditions it is realistically closer to 100 parasite/ $\mu\text{L}$ .<sup>67</sup> This lateral flow immunoassay coupled with SERRS detection was able to match the sensitivity of typical in-field light-microscopy diagnosis detecting  $\sim 65$  parasites/ $\mu\text{L}$ , at the lowest HRP-II concentration of 5 ng/mL, compared to its  $\sim 100$  parasites/ $\mu\text{L}$ . With regards to the theoretical LoD of the assay it was shown to surpass current achievable light-microscopy limits. However, it is perhaps unlikely that under in-field conditions with clinically relevant biological matrices this theoretical HRP-II detection concentration would be achieved. Nevertheless, this assay highlights the sensitivity

that can be gained by coupling these frequently used lateral flow devices with a SERRS-based detection output.

#### 4.2.3.3 Colourimetric analysis to quantify HRP-II

The sensitivity of this SERRS based lateral flow immunoassay was compared to the theoretical LoD value that could be achieved based on colourimetry readings of the test spots. To measure these values, the lateral flow strips were first scanned using a flatbed scanner onto a computer. ImageJ software was then used to quantify the signal of the Green channel, from the RGB values of the test spots, as it was the most sensitive to the colour produced by the colloidal gold. RGB measurements indicate how much of the Red, Green, and Blue is in the channel you have measured. The signal can then be normalised by subtracting it from the maximum signal that can be obtained (this is 255 for each channel). A calibration curve of normalised signal intensity against HRP-II concentration can then be plotted (Figure 4.15).

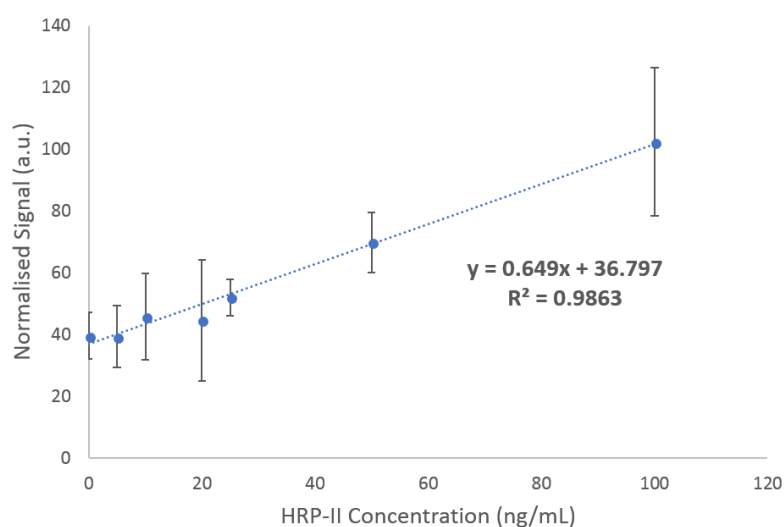


**Figure 4.15** Colourimetric analysis of test spots on the lateral flow immunoassay. A calibration curve has been plotted of the normalised signal intensity from the Green channel vs. HRP-II concentration. The error bars shown are the standard deviation of the 3 replicate lateral flow measurements for each concentration analysed. The equation of the line is also shown.

Analysis of this lateral flow sandwich assay *via* colourimetry measurements produced a calibration curve with good linearity between the normalised signal responses and the corresponding HRP-II concentrations, however, there were very large standard deviations between replicate measurements. One of the main causes of this replicate variation may have been the variability in test spot size. To measure the RGB value of a spot a defined area for the ImageJ software to analyse must be set and kept constant for all measurements. In this immunoassay design the capture Ab is spotted directly onto the nitrocellulose lateral flow strip and left to dry. Once this reagent has been spotted there is no control over how it spreads and dries on the strip, which can create a non-homogenous capture area. This means the binding of the antigen-Ab-Au conjugate when it flows over will not give a uniform spot colour and when analysing a defined area in the software there may be large areas where there is no colour from the Au colloid. This lack of conjugate binding homogeneity was also observed when the test spots were Raman mapped (Figure 4.13(A)). Because of the larger standard deviations, the theoretical LoD for the colourimetry measurements was calculated to be 34.7 ng/mL (~454 parasites/ $\mu$ L), much higher than that calculated for the SERRS-based detection (65.3 pg/mL vs. 34.7 ng/mL) and, therefore, this method would not be able to compete with the current standard detection.

In this analysis the colourimetric quantification method was not as sensitive as using SERRS, however, with better control over the capture Ab spot homogeneity it would be possible to lower the standard deviations between replicates. Also, if a greater signal response from the Green channel could be generated for each concentration analysed, a steeper calibration line with a larger slope may be achievable and, in-turn, the sensitivity of the optical measurement would be increased. This could be achieved by increasing the final concentration of the Ab-conjugated SERRS tags in solution, although this could also lead to an increase in non-specific binding within the blank.

#### *4.2.3.4 Issues with lateral flow immunoassay*

Although SERRS-based analysis of the lateral flow sandwich assays showed low measurement variability between replicates and had a good linear relationship

between the Raman peak height and HRP-II concentration, they are currently not able to compete with already available lateral flow RDTs. One of the main causes of this is the way the capture antibody and the anti IgG control were applied to the nitrocellulose strip. For reproducibility the application of reagents onto the membrane requires a high level of consistency<sup>178</sup> that is typically achieved by using a reagent dispensing system to spray a controlled amount of known concentration onto the strip to give a homogenous test and control line.<sup>136,142</sup> The issues with spotting on the reagents were discussed in section 4.2.3.3 above.

To be applied as an RDT with SERRS as the detection method, it would be preferable if the lateral flow analysis could be carried out on a portable Raman system that could be run in-field. This work was carried out using a large benchtop Renishaw InVia confocal Raman microscope and so is not practical for the point-of-care diagnosis that is targeted with these immunoassays. To address this issue a 3D- $\mu$ PAD that could be coupled with a handheld, portable Raman spectrometer to detect HRP-II was investigated.

#### *4.2.4 3D- $\mu$ PAD for HRP-II detection*

An alternative to the traditional lateral flow immunoassays are  $\mu$ PADs. In this work, a 3D  $\mu$ PAD was coupled with SERRS to study its potential to detect clinically relevant concentrations of HRP-II. The layered components of the device used were designed and printed by Professor Charles Mace's group at Tufts University.

##### *4.2.4.1 Running and optimisation of the 3D device*

The paper-based device architecture was developed using wax printing to create black hydrophobic barriers on each layer and, once assembled, the hydrophilic zones (white areas) created a network of lateral and vertical channels that controlled the wicking of fluids through the device (Figure 4.16). Devices were manufactured using a combination of nylon membrane for the capture layer (pore size  $\sim 0.45 \mu\text{m}$ ) and chromatography paper for the other layers (pore size  $\sim 25 \mu\text{m}$ ). Nylon membrane was chosen over nitrocellulose, used in typical lateral flow immunoassays, as nitrocellulose is more brittle and could be damaged during the wax printing



process.<sup>167</sup> Adhesive film was used to assemble the layers with removable adhesive applied to the incubation layer, so that the top 3 layers could be easily removed to reveal the capture layer. Double-sided permanent film was applied to all other layers to aid in the overall structural integrity.

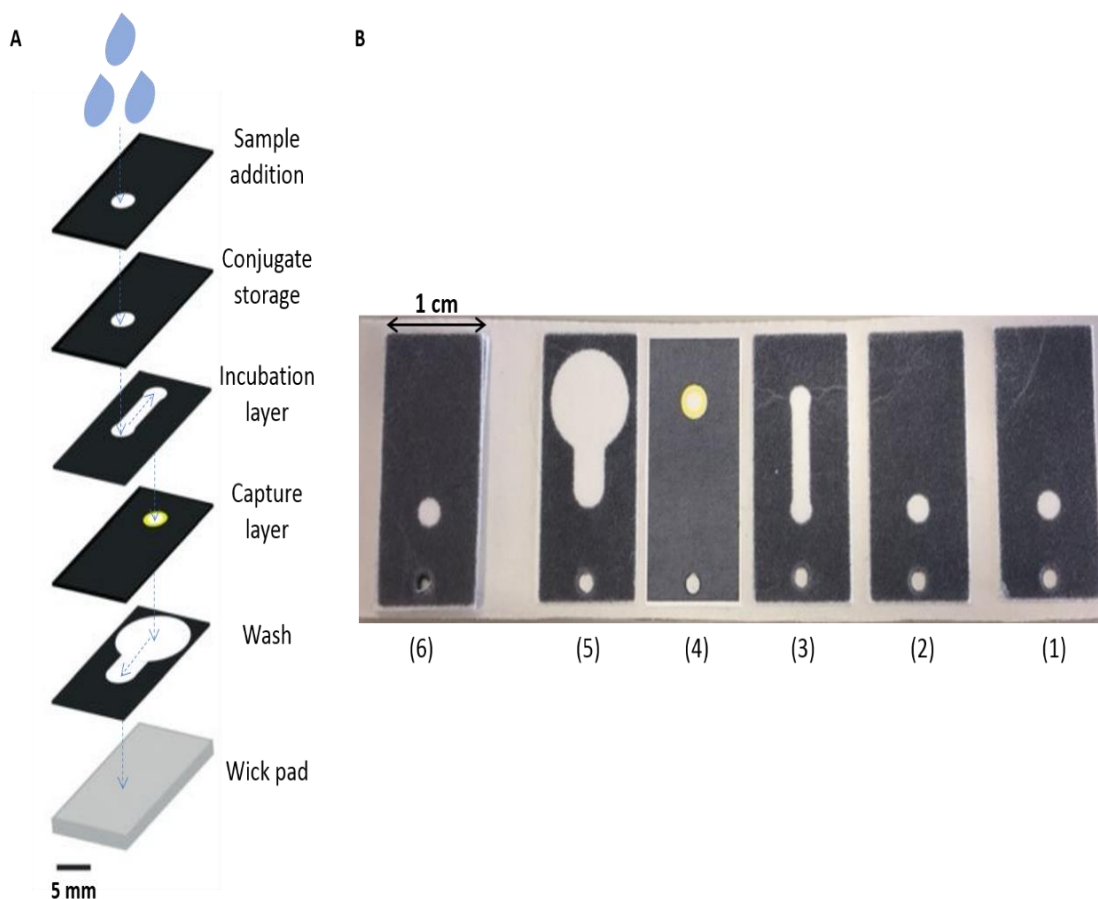


**Figure 4.16** (A) Schematic of a 3D-patterned paper device for singleplex immunoassays. Black areas, created by wax printing, are hydrophobic barriers and the white hydrophilic areas create the fluid channels. Blue dashed arrows highlight the movement of samples and washes as they are applied to the top sample addition layer. A yellow ring of wax was applied around the capture zone on the capture layer to help visualise the red colour of the Au colloid. A thicker sheet was also used on the bottom layer to act as a sink to wick away any excess liquid during the running of the device.<sup>166</sup> (B) Images of each individual layer of the 3D-device. (1) Sample addition, (2) conjugate storage, (3) Incubation layer, (4) Capture layer, (5) Wash, and (6) Fully assembled device, approximately 1 cm in width. Figure 4.16(A) reproduced from Schonhorn, J., A device architecture for three-dimensional, patterned paper immunoassays, *Lab on a chip*, 2014, **14**, 4653-4658, with permission of The Royal Society of Chemistry.

Initially experiments were carried out to identify the conditions that would maximise signals from positive HRP-II samples and reduce any signal arising from non-specific binding on the capture layer when the device was challenged with negative samples. Two main conditions were varied to study this: (i) Concentration and volume of capture Ab used, (ii) Concentration of conjugate Ab used. Only the conjugate layer and capture layer were treated before the device was assembled and used.

When deciding on a concentration of capture antibody, previous literature that have applied this device, or a form of, was considered. Schonhorn *et al.*<sup>165</sup> highlighted the application of this device to detect a biomarker related to pregnancy, using a capture antibody concentration of 1 mg/mL (5  $\mu$ L) and Deraney *et al.*<sup>181</sup> reported a multiplexed version where capture antibody concentrations were either 1 or 2 mg/mL (1  $\mu$ L). These concentrations were used as a guide and for the application here, 100  $\mu$ g/mL and 500  $\mu$ g/mL of capture antibody were considered. 2  $\mu$ L of each concentration were spotted on the capture layer and left to dry, before being blocked with blocking buffer (3  $\mu$ L). Once dried and assembled, Au-Ab conjugate in a buffer blank were run through each device to assess any non-specific binding occurring (Figure 4.17). From this experiment it was found that using the higher antibody concentration on the capture layer did not increase the non-specific binding and it was concluded that using this higher concentration, at a low volume, should lead to good binding when target antigen was present.

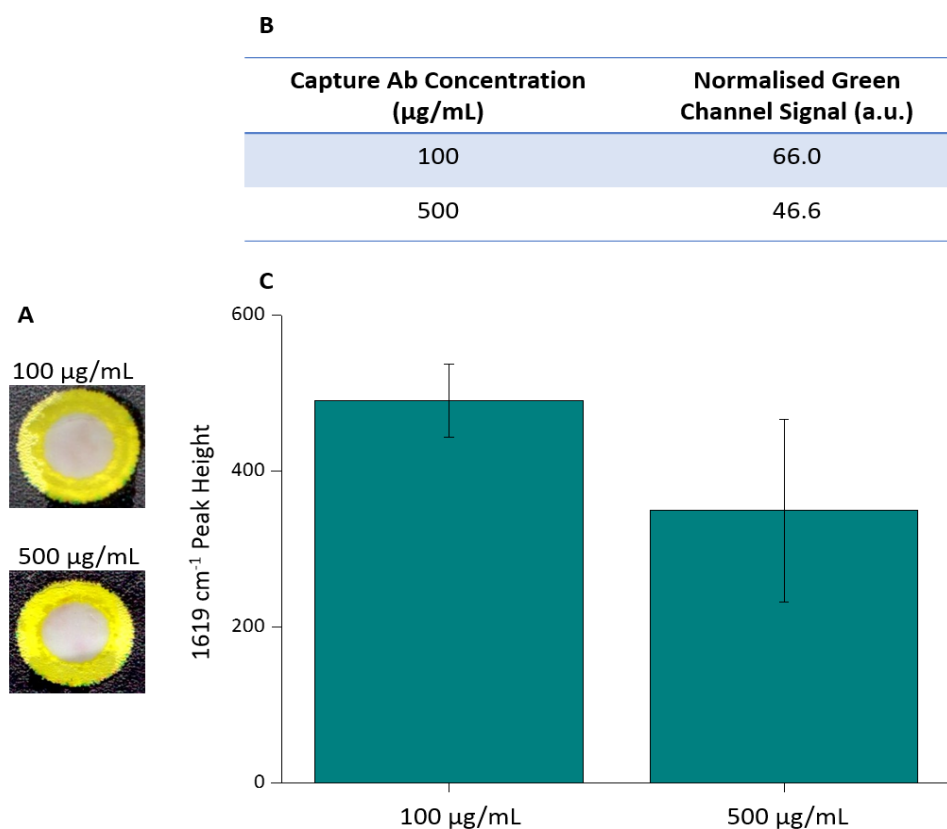


**Figure 4.17** Investigation to determine capture antibody concentration to be applied. (A) Scanned image of capture layer following flow through of Au-Ab conjugate in blank buffer. (B) Images of capture layers were analysed to give RGB values. Shown are the normalised signals from the Green channel of each concentration. (C) Average  $1619\text{ cm}^{-1}$  peak height from the SERRS of both capture layers. Error bars show the standard deviation of the SERRS measurements at  $1619\text{ cm}^{-1}$  for both concentrations. These results show some non-specific binding occurring at both concentrations although it is slightly lower with the  $500\text{ }\mu\text{g}/\text{mL}$  capture antibody.  $1619\text{ cm}^{-1}$  peak heights are the average of 20 spectra collected with  $638\text{ nm}$  laser excitation,  $26.7\text{ mW}$  laser power,  $0.1\text{ s}$  acquisition time.

The chosen concentration of Au-Ab conjugate was also important as it had to be concentrated enough to give a distinct red colour when bound to HRP-II on the capture layer. However, too much conjugate may have overloaded the device and stuck to the capture layer even when no antigen was present, leading to false positives. The conjugate concentration used for lateral flow immunoassays was studied ( $\sim 0.7\text{ nM}$ ) along with a lower concentration ( $\sim 0.4\text{ nM}$ ). Conjugate storage layers were treated with  $10\%$  BSA ( $3\text{ }\mu\text{L}$ ), left to dry, followed by the application of  $5\text{ }\mu\text{L}$  Au-Ab conjugate at both concentrations. Once dried the devices were assembled

and a buffer blank ran through (30  $\mu\text{L}$ ) followed by two washes (2x20  $\mu\text{L}$ ). At the end of the runs the capture layers were exposed, and it was found that with the higher conjugate concentration a considerable amount had bound to the capture layer, whereas with the lower one relatively little colour was present due to Au nanoparticles (Figure 4.18). From this, a Au-Ab conjugate concentration of 0.4 nM was chosen for future experiments with the device.

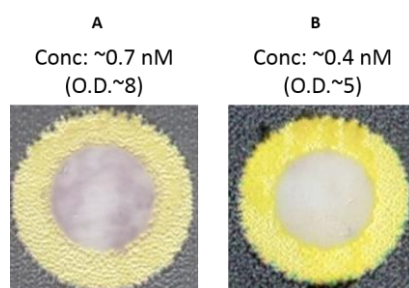


**Figure 4.18** Scanned images of the capture layers with different Au-Ab conjugate concentrations. (A) Conjugate concentration of 0.7 nM (Optical density, O.D.,  $\sim 8$ ) was used and resulted in significant binding to the capture layer when a buffer blank was run through. (B) Conjugate concentration of 0.4 nM (O.D.  $\sim 5$ ) gave very little binding in the capture layer when a buffer blank was run. This was the Au-Ab conjugate concentration chosen going forward with further experiments.

With these parameters chosen and shown to be contributing minimal signal from non-specific binding when negative samples were run, this 3D- $\mu\text{PAD}$  could be used to quantify HRP-II using SERRS and colourimetry measurements.

#### 4.2.4.2 SERRS quantitative analysis of the capture layer

Once the concentration and volume of capture Ab and Au-Ab conjugate had been determined to give the best performance of the assay, the LoD was tested using 8 concentrations of target analyte prepared by serial dilution in the range of 100 – 0.75 ng/mL in sample buffer. Each concentration was tested in triplicate along with a buffer blank, also run in triplicate. Unlike the lateral flow immunoassay that was analysed using a confocal Raman microscope, a handheld CBEx spectrometer from Snowy Range Instruments was used to analyse the results on the capture layer (Figure 4.19). This used a 638 nm laser excitation wavelength and so SERRS enhancement was still achieved using this handheld, portable spectrometer.

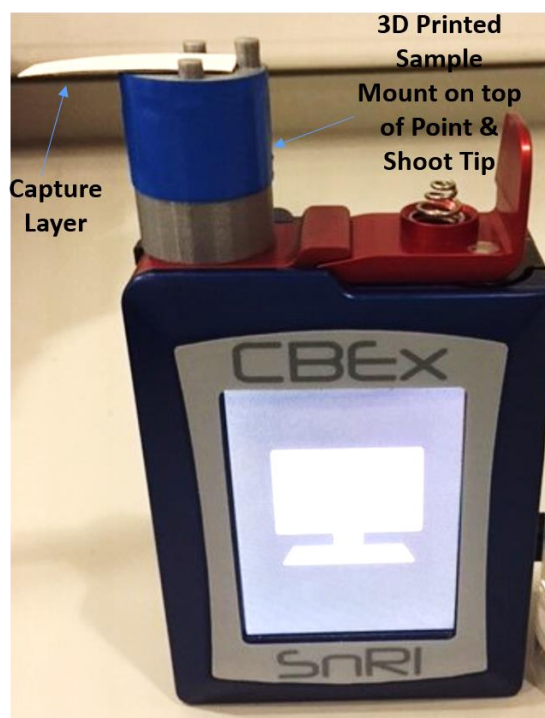


**Figure 4.19** Image of the handheld CBEx 638 nm spectrometer from Snowy Range Instruments used to analyse the results on the capture layer of the 3D  $\mu$ PAD. A 3D printed sample mount was placed on top of the point and shoot adapter, so the capture layer could be placed on top. This mount had a precise hole that matched the size of the capture layer spot so only this was interrogated by the 638 nm laser. Three plastic pins on top of the mount held the capture layer in place while it was analysed.

CBEx instruments have an orbital raster scanning (ORS) feature that was also used when analysing the capture layer read-outs. The ORS technology enables accurate and precise measurement of heterogeneous materials by keeping the beam tightly focussed while increasing its size with a large patterned laser excitation.<sup>182</sup> Raman information was then obtained over the whole capture layer spot area without losing spectral resolution. Using this feature, 20 spectra were collected in triplicate for each HRP-II concentration and the blanks. These were then averaged to give a final SERRS spectrum for each and a calibration curve created by plotting the  $1619\text{ cm}^{-1}$  peak height against HRP-II concentration (Figure 4.20).

Visual inspection of the capture layer showed that, particularly at the higher HRP-II concentrations (100 – 12.5 ng/mL), the spots had a mottled appearance and were

not homogeneous with respect to the distribution of the Au-Ab conjugate red colour (Figure 4.20(A)). Therefore, the ORS feature was used to gain an average spectrum from the whole spot. Also, a positive visual identification of HRP-II detection was difficult/not possible below 12.5 ng/mL. However, with SERRS, positive discrimination of the lowest concentrations from the blank was made. From the calibration curve, the theoretical LoD was calculated to be 1.68 ng/mL which converted to ~22 parasites/ $\mu$ L (~0.00044 % parasitemia). This detection limit of infection density was lower than what is typically achievable by a technician analysing a blood smear by light microscopy (~100 parasites/ $\mu$ L, 0.002 % parasitemia). The possibility of being able to reliably detect lower-density parasitemia with this SERRS-3D- $\mu$ PAD could also allow positive malaria identification in asymptomatic individuals.

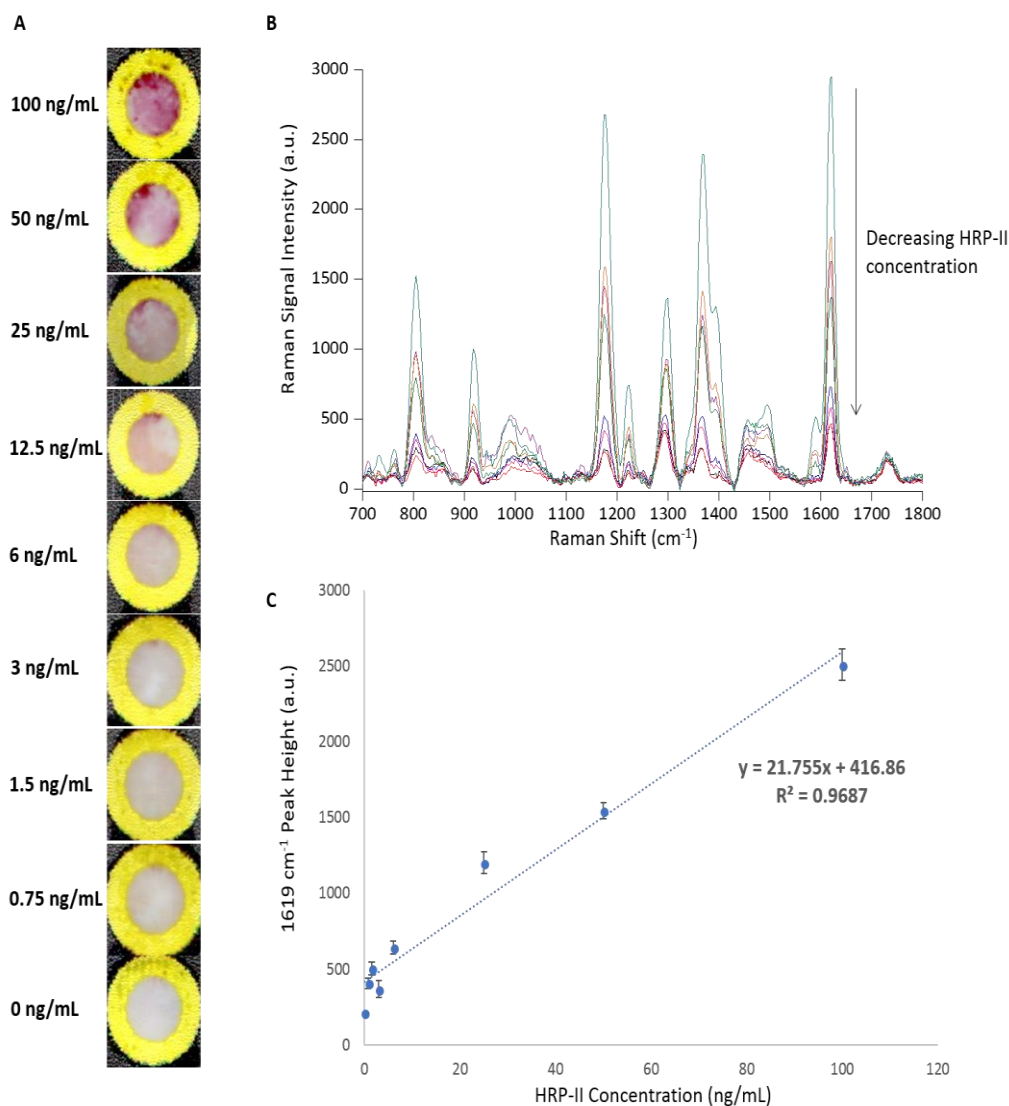


**Figure 4.20** Results of concentration study using 3D devices. (A) Scanned images of the capture layer for one of the replicates at each target antigen concentration. A gradual decrease in the red colour from the Au nanoparticles was observed going from the highest concentration (100 ng/mL) to the lowest (0.75 ng/mL). (B) Average Raman spectrum for each antigen concentration analysed: 100 (cyan), 50 (orange), 25 (green), 12.5 (purple), 6 (blue), 3 (red), 1.5 (pink), and 0.75 ng/mL (black). A decreasing trend in Raman signal intensity with decreasing HRP-II concentration was observed. (C) Intensity of 1619 cm<sup>-1</sup> peak height vs. final HRP-II concentration. The spectra are the average of 20 measurements of 3 replicates (60 in total) for each concentration. Error bars are the standard deviations of the replicate measurements. The equation of the line is also shown. Spectra were collected using a 638 nm laser excitation, 26.7 mW laser power, 0.1 s acquisition time. Spectra were baseline corrected and averaged using Matlab R2013a. 1619 cm<sup>-1</sup> peak heights were calculated using signal-to-baseline.

In these experiments the capture layers were analysed by SERRS as soon as the top layers were removed, however, it was noted that after 10 – 15 minutes of the capture layer being revealed the colour of the capture spot had changed from red to a darker purple colour indicating that the Au nanoparticles were beginning to aggregate on the surface as the spot dried (Figure 4.21). Aggregation of nanoparticles as they dry on a surface is known to occur<sup>183</sup> so care must be taken with this device to analyse the capture layer as soon as it has been revealed to give reproducible SERRS spectra between replicates.

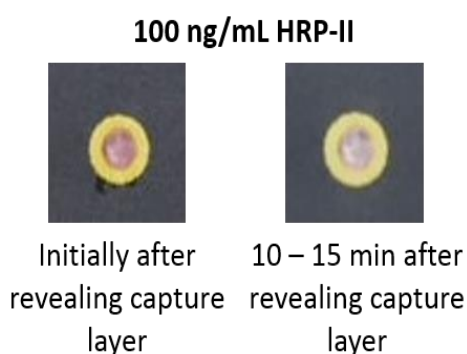


**Figure 4.21** Images of the same capture layer for 100 ng/mL HRP-II sample, taken ~15 minutes apart. When the capture layer was first revealed by peeling off the top layers, the capture spot appeared red in colour typical of Au nanoparticles. However, after 10 – 15 minutes of being exposed, the nanoparticles appeared to have aggregated as they dried, turning a dark purple colour.

Coupling this  $\mu$ PAD with SERRS detection gave low, nanogram per millilitre detection limits for HRP-II that fell in the lower range of parasite density that can be detected *via* a blood smear. These capture layers were also quantified using colourimetric methods, used in section 4.2.3.3, to evaluate if the portable, handheld Raman spectrometer brought a level of sensitivity that could not be achieved using these colour analysis techniques.

#### 4.2.4.3 Colourimetric analysis of the capture layer

As with the lateral flow immunoassay, the capture layers were scanned, and ImageJ software was used to analyse the RGB values for each capture layer spot. The



normalised signal from the Green channel was then plotted against HRP-II concentration to generate a calibration curve (Figure 4.22).

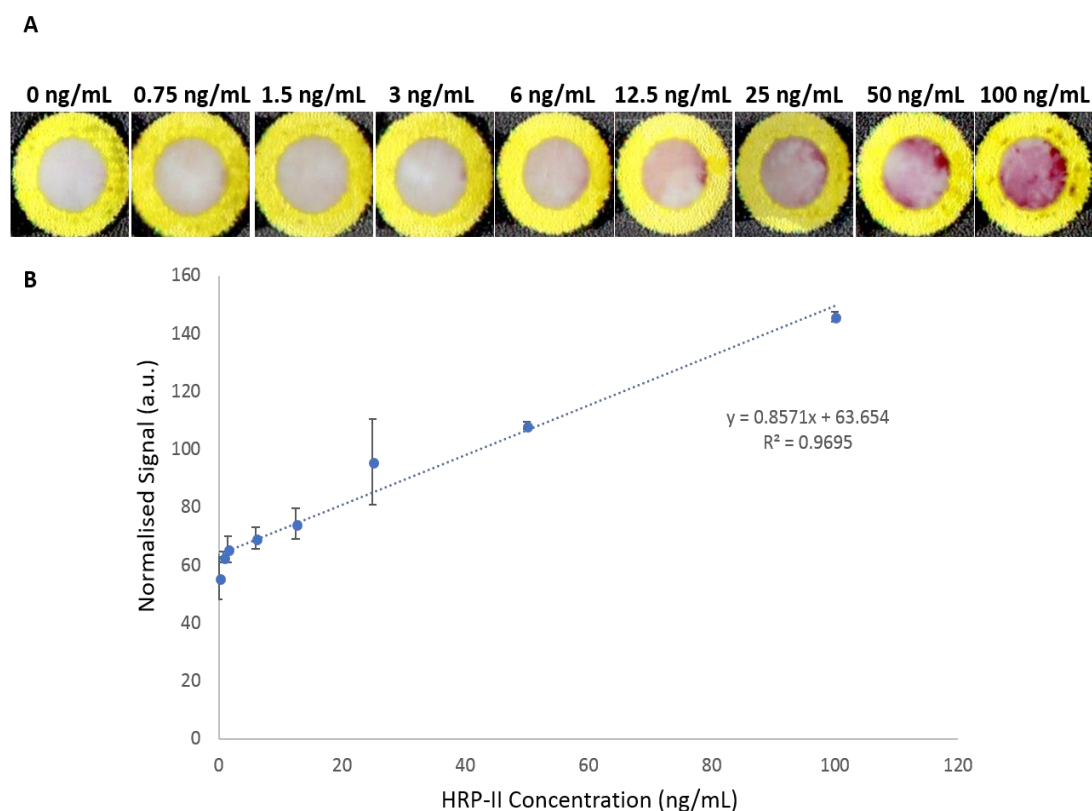


**Figure 4.22** Colourimetric analysis results. (A) Scanned images of the capture layer for one of the replicates at each target antigen concentration. Within ImageJ software an area was set to read the RGB value of the whole capture layer spot and give an average value for each spot. This was done for all 3 replicates. (B) Calibration curve of normalised signal vs. HRP-II concentration. The reading for each HRP-II concentration and blank are the average of 3 replicates. Error bars are the standard deviations of the replicate measurements. The equation of the straight line is also shown.

Colourimetric analysis showed good linearity between normalised Green channel signal and HRP-II concentration, giving a theoretical LoD of 25.5 ng/mL (~333 parasites/ $\mu$ L). However, this was much higher than that achieved using SERRS (1.68 ng/mL) and was over 3x higher than the 100 parasites/ $\mu$ L detectable by conventional methods. Under the experimental conditions used in this work, colourimetric analysis was not as sensitive as SERRS for the detection of low HRP-II concentrations.

#### 4.2.4.4 3D- $\mu$ PAD selectivity

The selectivity of the 3D-paper device was investigated by performing the assay with a different biomolecule to ensure that binding of Au-Ab conjugates and subsequent signal from the Raman reporter was only present when HRP-II was added. C-reactive protein (CRP), an important inflammation biomarker, was chosen as the negative control antigen. Although CRP would likely be present within the blood, sometimes more so during an infection, the detection and capture antibody used within this sandwich assay are specific to HRP-II and so should only bind to any HRP-II that was present within a blood sample. This was run through a device alongside HRP-II, both at concentrations of 25 ng/mL, and analysed using the handheld 638 nm CBEx Raman spectrometer taking an average of 20 spectra for each. The results are shown in Figure 4.23.

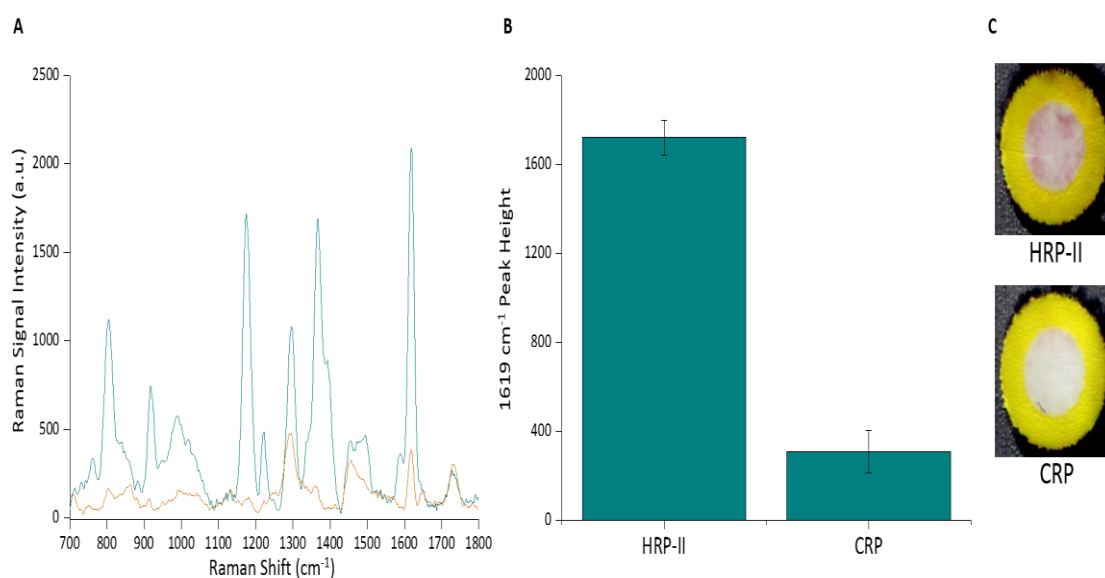


**Figure 4.23** Selectivity results of the 3D-device. (A) Average Raman spectrum for 25 ng/mL of each antigen that was run through the device: HRP-II (cyan) and CRP (orange). (B) Average 1619 cm<sup>-1</sup> peak height for each antigen. (C) Scanned images of each capture layer for both antigens. Although from the images of the capture layer it appeared to show no binding of Au-Ab conjugate when CRP was run through the device, the average SERS spectrum and 1619 cm<sup>-1</sup> peak height did show some non-specific binding of CRP on the capture zone. The spectra are the average of 20 spectra taken from each capture layer using the ORS feature. Error bars show the standard deviation of the 1619 cm<sup>-1</sup> peak height measurements for the 20 spectra taken for each sample. Spectra were obtained using 638 nm laser excitation, 26.7 mW laser power, 0.1 s acquisition time. Spectra were baseline corrected and averaged using Matlab R2013a. 1619 cm<sup>-1</sup> peak heights were calculated using signal-to-baseline.

As observed above, when HRP-II was run through the device, the Au-Ab conjugates bound to the capture layer and an intense SERRS response was detected from the spot. In contrast, when CRP was run on a device no red spot was seen on the capture layer showing no significant binding of the Au-Ab conjugates, however, when the result was interrogated with 638 nm laser excitation a SERRS response was recorded. The Raman signal intensity from this was much lower than that recorded when HRP-II was present, and this difference was observed by plotting the average peak height of the  $1619\text{ cm}^{-1}$  peak for both samples. Non-specific binding of the Au-Ab conjugates appeared to have been taking place in the negative antigen control run, resulting in a slight SERRS response. As SERRS is a very sensitive detection technique, only a small amount of sample needs to be present to give a SERRS response, as shown here in the negative control. With further optimisation of parameters such as the blocking of the capture layer, the number of washes, and perhaps pre-treatment of the incubation layer this specificity could be improved. Despite this, these results showed that overall the device was selective for HRP-II under these conditions.

#### *4.2.4.5 HRP-II detection in a biologically relevant matrix*

These results highlighted the ability of this 3D- $\mu$ PAD to detect samples of antigens in aqueous buffer successfully with a low theoretical LoD when coupled with SERRS. In addition to this, it was important to demonstrate device performance when clinically relevant sample matrices were present, such as whole human blood. To achieve this using whole blood, a GR Vivid™ Plasma Separation Membrane was added to the top of the sample addition layer. When a blood sample is spotted on top, the highly asymmetric structure of this membrane allows the cellular components of blood to become trapped in the larger pores while plasma flows down into the smaller pores, allowing the analysis of the blood plasma. In addition, the protein concentration of any clinical biomarkers that are present within the blood is not reduced, making it an ideal material for diagnostic purposes.<sup>184</sup>

Whole human blood (10  $\mu$ L) was spiked with HRP-II (1000 ng/mL, 2  $\mu$ L) and 8  $\mu$ L PB added to give a final concentration of 100 ng/mL antigen. CRP was also spiked into blood at the same concentration to be used as a negative control. These were spotted

on top of the plasma separation membrane that had been attached to the top layer of the device and allowed to migrate through the layers. Washes were added on top to facilitate the flow (50  $\mu\text{L}$  0.1 % Tween-20 in PB). At the end of the run the capture zone was revealed and the spot analysed as before (Figure 4.24). In this instance when the capture layers were exposed, a further wash was spotted on top (20  $\mu\text{L}$ ) to help clean the spot of any RBCs that may have flowed through and were adding to the red colour of the spot.

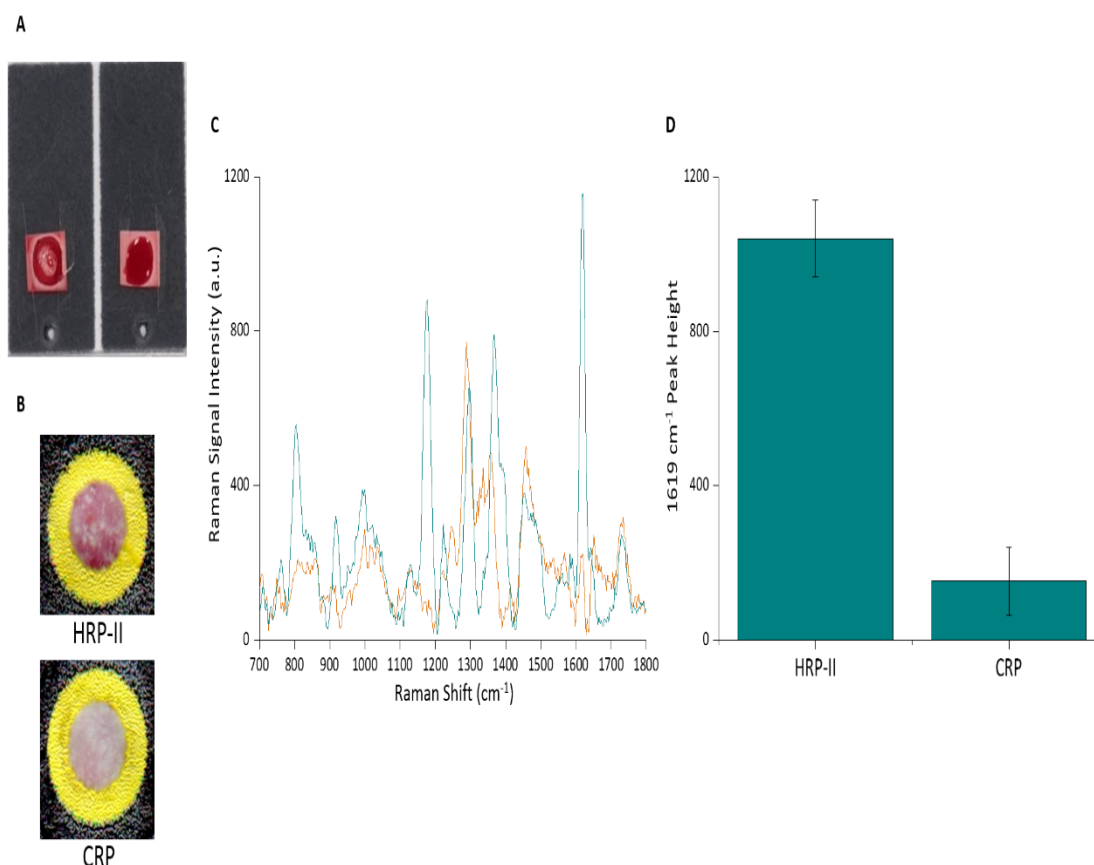


**Figure 4.24** Antigen detection in whole human blood (A) Image of device being run with GR Vivid Plasma Separation Membrane. The blood spiked with antigen was spotted on top and allowed to flow through the membrane and separate out and then through the device as before. (B) Scanned images of the capture layer when HRP-II and CRP were spiked into the blood at final concentrations of 100 ng/mL (C) Average SERRS spectra for both capture layers: HRP-II (cyan) and CRP (orange). (D) Bar chart of the average 1619  $\text{cm}^{-1}$  peak height for both antigens detected in blood. The spectra are the average of 20 spectra taken from each capture layer using ORS feature. Error bars show the standard deviation of the 1619  $\text{cm}^{-1}$  peak height measurements for the 20 spectra taken for each sample. Spectra were obtained using 638 nm laser excitation, 26.7 mW laser power, 0.1 s acquisition time. Spectra were baseline corrected and averaged using Matlab R2013a. 1619  $\text{cm}^{-1}$  peak heights were calculated using signal-to-baseline.

Visual inspection of both capture layers showed significantly more conjugate binding when HRP-II was present, however, some non-specific binding occurred in the negative control (when CRP was run through). The SERRS response also confirmed this with signal attributable to the Raman reporter, MGITC, detected from both spots. Although the  $1619\text{ cm}^{-1}$  peak height, that had been used throughout to track SERRS signal, was much more intense in the positive HRP-II antigen sample. The SERRS spectrum, particularly for the CRP spot, was noisier with a slight background. This may have been attributable to some blood components not being trapped in the plasma separation membrane and interfering with the SERRS response on the capture layer.

These initial results with a higher HRP-II concentration highlighted that this device was capable of detecting antigen in whole blood both visually and with SERRS. Further work to bring the limit to within current detection ranges of other techniques would require a much cleaner separation of the blood components from the antigen so that there was less interference on the capture layer. In this instance the plasma separation membrane was attached onto the top layer of the assembled device with sticky tape, however, if this could be fixed to create maximum contact with the top layer it may stop blood leaching through the device and causing interference on the capture zone. Overall, this work has demonstrated the potential use of a 3D- $\mu$ PAD coupled with SERRS to detect low levels of *P. falciparum* specific HRP-II antigen. As it was coupled to a handheld, portable Raman spectrometer it could be easily employed in point-of-care settings and wouldn't require an operator as highly skilled as those needed to analyse blood smears with light microscopy.

### 4.3 Concluding Remarks

SERRS has been used to enhance the detection capabilities of RDTs for the malaria *P. falciparum* specific antigen, HRP-II. The technique was applied to two different RDT platforms with varying success. A traditional lateral flow immunoassay was studied using a sandwich assay design to detect target antigen through binding to Au-Ab conjugates and capture Ab that had been spotted onto the nitrocellulose strip. Positive identification resulted in a dark red spot that was then interrogated with a 633 nm laser excitation to gain a SERRS response. This method of analysis gave good quantifiable detection levels of HRP-II, down to 5 ng/mL, and a theoretical LoD of 65.3 pg/mL. These concentrations translated to ~65 and <1 parasite/ $\mu$ L, respectively. Both were below the standard detection range of 100 parasites/ $\mu$ L that is achieved through blood smear analysis. Although the theoretical LoD was very low, in practice it is unlikely this concentration would be detectable. SERRS analysis of the lateral flow immunoassays was carried out on a confocal Raman microscope that would have provided much greater sensitivity, allowing the calculation of such a low theoretical LoD, and is not suitable for in-field/point-of-care diagnostics that is the target of RDTs. Problems were also encountered with the reproducibility of the test and control spots as there was no control of the dispersion and drying of the capture Ab/anti-IgG once it had been spotted. This led to very heterogeneous spots of different sizes between replicate samples.

To move towards a more robust RDT coupled with SERRS, a 3D- $\mu$ PAD was studied. This gave a higher degree of reproducibility between sample replicates and as it had a defined capture spot size, due to the hydrophilic/hydrophobic barrier, it could be easily analysed with a portable, handheld CBEx Raman spectrometer. With this device a theoretical LoD of 1.68 ng/mL (~22 parasites/ $\mu$ L) was calculated. This detection limit surpasses the average of 100 parasites/ $\mu$ L from a blood smear and is close to the parasitemia levels that a skilled technician can detect (5 – 10 parasites/ $\mu$ L). HRP-II detection in a biologically relevant matrix, i.e. whole human blood, was also demonstrated with this 3D device. 100 ng/mL final concentration of antigen spiked into blood was detectable on the capture layer with SERRS. Although a large amount

of non-specific binding occurred in the negative sample, this initial experiment demonstrated the potential of this simple paper-based diagnostic test to be used with clinically relevant samples at a point-of-care/in-field setting.

To assess if coupling these devices with SERRS detection added sensitivity to the techniques, results were also quantified with a traditional colourimetric measurement. Issues were encountered when using this technique on the lateral flow test spots. Due to varying sizes and spot inhomogeneity, large standard deviations within replicate samples were observed resulting in a higher theoretical LoD of 34.7 ng/mL (~454 parasites/ $\mu$ L). However, future work could gain more control over the capture Ab area by spraying it on in a controlled line and it is therefore possible that this LoD could be improved. Replicate sample reproducibility was found to be much better for RGB measurements taken from 3D- $\mu$ PAD capture layers, however, a much higher theoretical LoD was calculated, 25.5 ng/mL (~333 parasites/ $\mu$ L), compared to that gained using SERRS (1.68 ng/mL). This demonstrates the increase in detection sensitivity that was achieved in this work by coupling the RDTs with SERRS.

Detection limits calculated for the 3D- $\mu$ PAD coupled with SERRS were shown to be in the lower range of what is detectable by a trained technician studying a blood smear with light microscopy. As these devices are made from paper-based materials, they are cheaper to manufacture, only require a small sample volume, and results can be run by someone with minimal training. The time taken from a sample, such as blood shown above, being spotted on the sample addition layer to a quantitative answer being recorded was ~15-20 minutes which competes closely with standard RDT's that are quoted as giving results within 15 minutes.<sup>185</sup> 3D- $\mu$ PAD also have the potential to be easily applied to detect other disease specific biomarkers. Overall, these results highlight the potential to improve the detection ability of RDTs for *P. falciparum* HRP-II by coupling them with a portable, handheld Raman spectrometer.

## 5 Experimental

---

### 5.1 Materials

#### 5.1.1 Chemicals

Mouse monoclonal antibody was purchased from BBI Solutions. Recombinant *P. falciparum* HRP-II antigen was purchased from CTKBiotech. CT(PEG)<sub>12</sub> and MGITC were purchased from ThermoFischer. All other chemicals were purchased from Sigma Aldrich unless otherwise stated.

#### 5.1.2 Buffer Preparation

##### 5.1.2.1 PBS

A 10 mM PBS solution was prepared by dissolving 8 g of NaCl, 0.2 g KCl, 1.44 g Na<sub>2</sub>HPO<sub>4</sub>, and 0.24 g KH<sub>2</sub>PO<sub>4</sub> in 800 mL of dH<sub>2</sub>O. This was then adjusted to pH 7.2 with 1 M HCl before adding enough dH<sub>2</sub>O to give a final volume of 1 L.

##### 5.1.2.2 PB

A 10 mM solution of PB buffer was prepared by dissolving 34.4 mg of PB powder in 20 mL of dH<sub>2</sub>O. This gave a working PB buffer solution with pH 7.2.

##### 5.1.2.3 HEPES buffer

A 100 mM stock solution of HEPES buffer was prepared by dissolving 2.38 g of HEPES powder in 50 mL of dH<sub>2</sub>O. This was adjusted to pH 7.2 with 1 M NaOH before adding enough volume of dH<sub>2</sub>O to give 100 mL of 100 mM HEPES buffer. 10 mM HEPES buffer was then prepared by taking 10 mL of the 100 mM stock HEPES buffer and diluting this in 90 mL of dH<sub>2</sub>O, giving a total volume of 100 mL.

### 5.2 Instrumentation

#### 5.2.1 Extinction spectroscopy

All UV-vis spectroscopy was carried out on an Agilent Cary 60 UV-visible spectrophotometer. A baseline measurement of the sample solvent was carried out before the samples were analysed. The range of wavelengths scanned was 200 – 800 nm.



### 5.2.2 DLS and zeta potential

Malvern Zetasizer Nano ZS was used to carry out all nanoparticle sizing and zeta potential measurements.

### 5.2.3 SEM measurements

Samples were analysed using a Sirion 200 Shottky field emission electron microscope operating at an accelerating voltage of 30 kV and a magnification of 500 nm. All SEM measurements were carried out by Dr. Samuel Mabbott.

### 5.2.4 IR measurements

IR measurements of solid sHz and hemin chloride were carried out using an ATR-IR instrument with Microlab PC software. Ethanol was used to clean the ATR crystal before each measurement and a background measurement was taken before the solid sample spectrum was taken.

## 5.3 Tissue work

### 5.3.1 Infections and tissue preparation

Procedures on mice were approved following local ethical review by the University of Glasgow Animal Procedures and Ethics Committee and were performed in strict accordance with the UK Home Office Animals (Scientific Procedures) Act 1986 (project licence no. P2F28B003). Two female, BALB/c mice (Harlan, Bicester, UK; 6–8 weeks old) were infected with asynchronous *P. berghei* ANKA, and euthanised when peripheral blood parasitemia reached 5%. Spleens were removed from these and from two uninfected control mice and embedded in tissue freezing medium (Tissue-Tek O. C.T.).<sup>114</sup> This freezing medium was used to preserve the tissue structure. Frozen tissue blocks were then positioned in a cryostat chamber at  $-22\text{ }^{\circ}\text{C}$ , cut into sections with a thickness of  $10\text{ }\mu\text{m}$  and placed on poly-L-lysine glass slides with Tissue-Tek O.C.T. Ten tissue sections were taken from the infected spleens, along with a further ten from the uninfected spleens. Four tissue sections from the infected spleens and four from the control, were also taken and placed on poly-L-lysine  $\text{CaF}_2$  slides. Tissue sections were stored at  $-20\text{ }^{\circ}\text{C}$  prior to analysis. Spleen tissue was chosen as it is a key tissue for the sequestration of the parasite.

### 5.3.2 *Poly-L-lysine coating of Raman-grade CaF<sub>2</sub> slides*

Raman grade CaF<sub>2</sub> slides were purchased from Crystran<sup>186</sup> to enable analysis of tissue sections using a 785 nm laser excitation. These slides were coated with poly-L-lysine using the following protocol.

Slides were washed in 100 % ethanol, then washed with dH<sub>2</sub>O before being left to dry. Once dry, the slides were placed in a solution of poly-L-lysine (molecular weight 70 000 – 150 000, 0.01 %) for five minutes. They were then removed, washed three times with dH<sub>2</sub>O and left to dry.

### 5.3.3 *Synthetic hemozoin preparation*

75 mg of hemin chloride was dissolved in 3 mL of 0.5 M NaOH and then neutralised with 1.5 mL 1 M HCl. 10 mL 3.9 M sodium acetate (pH 5) was then added and the solution was stirred in a water bath at 60 °C for 3 hours. The solution was then diluted in 40 mL of dH<sub>2</sub>O and filtered through a Buchner funnel. The residue was washed with dH<sub>2</sub>O to remove any excess salts, before being resuspended in dH<sub>2</sub>O and freeze dried overnight to yield a powder. This was carried out to allow an estimate of the weight of synthetic hemozoin produced. The final product was resuspended, at a concentration of 2.5 mg/mL, in PBS (10 mM, pH 7.2) and stored at -20 °C. Before use, the thawed aliquots were sonicated for 5 minutes to break up the larger particles.

The product was characterised using UV-vis spectroscopy by diluting the stock sHz (8 µL of sHz with 792 µL of dH<sub>2</sub>O). IR spectra of solid sHz, before it was resuspended in PBS, and solid hemin chloride were also recorded to observe the additional peaks seen within sHz spectrum.

### 5.3.4 *Reference spectra*

An aliquot of sHz was defrosted and a 10 mg/mL Hb solution prepared with PBS (10 mM, pH 7.2). 100 µL of each solution were spotted on glass coverslips and left to dry overnight before analysis. Reference spectra were then collected using a x20 objective, 30 s acquisition time, and a 532 nm laser excitation (0.1 mW).

100  $\mu\text{L}$  of sHz and Hb were also spotted on Raman grade  $\text{CaF}_2$  slides and left to dry. Spectra were then collected using x20 objective, 6 s acquisition time, and a 785 nm laser excitation (190 mW).

### 5.3.5 Raman mapping

Tissue sections were left to thaw at room temperature, washed once with PBS (10 mM, pH 7.2) and finally rinsed in  $\text{dH}_2\text{O}$ . Raman mapping was performed using a Renishaw inVia Raman spectrometer equipped with 532 nm laser excitation (1 mW) and an 1800  $\text{l mm}^{-1}$  grating. Raman images of uninfected and infected malaria tissue were recorded using a  $\times 50$  objective ( $\text{NA} = 0.75$ ) with an integration time of 3 s per spectrum, a step size of 1  $\mu\text{m}$ , and in the spectral range of 680 – 2330  $\text{cm}^{-1}$ .

For Raman mapping with a 785 nm excitation wavelength, the same Renishaw inVia Raman spectrometer was used, equipped with a 1200  $\text{l mm}^{-1}$  grating and a laser excitation power of 190 mW. Raman images of the tissue samples were recorded using a  $\times 50$  objective ( $\text{NA} = 0.75$ ) with an integration time of 5 s per spectrum, a step size of 1  $\mu\text{m}$ , and in the spectral range of 734 – 1765  $\text{cm}^{-1}$ .

### 5.3.6 PCA Analysis

PCA was applied to highlight any spectral separation between the control and infected data sets using Matlab software version R2013a (The MathWorks, Natick, MA, USA). Multiple maps for both tissue types were combined and averaged to give 43 final spectra for both the control and infected tissue data sets. The data set was then mean centred and normalised prior to PCA being applied. Principal component one (PC1) was then plotted against principal component two (PC2). The loadings plots were also plotted to determine correlation. All analysis within Matlab software was performed using custom scripts.

### 5.3.7 Prussian blue staining of tissue

Control and infected tissue sections on glass slides were stained with Prussian blue staining method.<sup>187</sup> Tissue sections were washed once with PBS (10 mM, pH 7.2) and finally rinsed in  $\text{dH}_2\text{O}$ . The slides were then immediately transferred into the working solution, avoiding the tissue drying. The slides were then left to stand in the working

solution at room temperature for 30 minutes. Following this, they were rinsed in dH<sub>2</sub>O and then placed in nuclear-fast red solution to incubate at room temperature for 5 minutes. At the end of this incubation, slides were washed in dH<sub>2</sub>O. Finally, once allowed to dry, a small drop of mounting solution was added to the corner of the glass slide and a coverslip placed on top of the stained tissue. Tissue slides could then be inspected using a standard laboratory light microscope.

**5% potassium ferrocyanide** – 25 mg potassium ferrocyanide was dissolved in 500 mL dH<sub>2</sub>O and mixed well.

**5% hydrochloric acid** – 25 mL concentrated hydrochloric acid was added to 475 mL dH<sub>2</sub>O and mixed well.

**Working solution** – 25 mL 5 % potassium ferrocyanide was added to 25 mL 5 % hydrochloric acid solution to make the working solution for the Prussian blue stain. This was made fresh on the day of use and discarded after.

### 5.3.8 *Animal model*

Procedures on mice were approved following local ethical review by the University of Glasgow Animal Procedures and Ethics Committee and were performed in strict accordance with the UK Home Office Animals (Scientific Procedures) Act 1986 (project licence no. P2F28B003). *P. falciparum* parasites in blood were purified to give a high parasitemia of between 60 – 70 %. Three NSG mice were injected, *via* intravenous tail injection, with these infected RBCs. While two NSG mice were used as controls and received uninfected RBCs. Once injected, these infected RBCs circulated the mouse bodily rapidly and entered the spleen and liver where they sequestered. Mice were then anaesthetised individually, and depilatory cream was applied to the torso to remove the hair and allow imaging of the spleen and liver. The mice were placed under the spectrometer probe. Spectra were collected from three different areas of each organ. After these Raman spectra had been collected the mice were culled and the spleen and liver harvested. *Ex-vivo* Raman spectra were then taken from three different areas of the spleen and liver.

Raman measurements were performed using an in-house built system equipped with a 785 nm laser. *In-vivo* and *ex-vivo* spectra were recorded with a 1 s acquisition time, 0.45 mW laser power, and in the spectral range 300 – 2023  $\text{cm}^{-1}$ .

## **5.4 Lateral flow assay and 3D-paper-based microfluidic device**

### *5.4.1 Synthesis of Au nanoparticles*

All glassware was soaked in aqua regia for 1 -2 hours and then rinsed thoroughly with  $\text{dH}_2\text{O}$  before use.

50 nm Au nanoparticles were synthesised by adding sodium tetrachloroaurate (60.5 mg) to  $\text{dH}_2\text{O}$  (500 mL) which was heated until boiling in a 3-necked round bottom flask (1 L). Upon boiling sodium citrate (57.5 mg) was added and the boiling maintained for 15 minutes before being allowed to cool to room temperature. Constant stirring was maintained throughout using a glass linked stirrer. The resulting Au nanoparticles were characterised using extinction spectroscopy and DLS by diluting 400  $\mu\text{L}$  of Au nanoparticles in 400  $\mu\text{L}$   $\text{dH}_2\text{O}$ . To minimise issues that arise from batch to batch variation, experiments were performed using the same batch of colloid.

### *5.4.2 SEM preparation*

Samples for SEM were prepared by spotting 10  $\mu\text{L}$  of Au nanoparticles onto a silica wafer and left to dry overnight.

### *5.4.3 Antibody conjugated Au nanoparticles*

#### *5.4.3.1 MGITC functionalisation to Au nanoparticles*

10  $\mu\text{L}$  MGITC ( $1 \times 10^{-5}$  M stock) was added to 990  $\mu\text{L}$  Au nanoparticles. This solution was left to shake for 30 minutes and then centrifuged at 5000 rpm for 20 minutes. The supernatant was removed, and the pellet resuspended in 1 mL  $\text{dH}_2\text{O}$ . The resulting MGITC-Au nanoparticles were then characterised using extinction spectroscopy and DLS by diluting 80  $\mu\text{L}$  in 720  $\mu\text{L}$  of  $\text{dH}_2\text{O}$ .

#### 5.4.3.2 Carbodiimide crosslinking conjugation

1 mg/mL solutions of EDC and sNHS were prepared in HEPES buffer (10 mM, pH 7.2). 74  $\mu\text{L}$  EDC and 40  $\mu\text{L}$  CT(PEG)<sub>12</sub> (1 mM in dH<sub>2</sub>O) were mixed together to activate the carboxyl groups on the PEG molecule. At the same time, 20  $\mu\text{L}$  mouse monoclonal Ab (0.5 mg/mL) was mixed with 217  $\mu\text{L}$  sNHS. The EDC/PEG mixture was then added to the Ab/sNHS and the final volume made up to 1 mL with HEPES buffer (649  $\mu\text{L}$ ). A blank solution was also made by substituting 20  $\mu\text{L}$  mouse monoclonal Ab with 20  $\mu\text{L}$  HEPES buffer. The solutions were left to shake overnight.

The following day, this solution was added to 1 mL MGITC-Au nanoparticles, left to shake for 2 hours and then centrifuged at 5000 rpm for 20 min. The supernatant was removed, and the final Ab conjugated colloid solution was resuspended in PB buffer (10 mM, pH 7.2 + 0.1 % BSA). Conjugates were then characterised using extinction spectroscopy, DLS, gel electrophoresis, and a lateral flow immunoassay. For extinction spectroscopy and DLS measurements, 400  $\mu\text{L}$  of sample was diluted in 400  $\mu\text{L}$  dH<sub>2</sub>O.

#### 5.4.3.3 Gel electrophoresis

A 1 % agarose gel was prepared by dissolving 1 g of agarose in 100 mL TBE buffer by applying heat and then leaving the gel to cool and set. Bare Au, MGITC-Au, PEG-Au (conjugate blank), and Ab-PEG-Au nanoparticles were centrifuged, and the supernatant removed to concentrate the samples. 20  $\mu\text{L}$  of each sample was mixed with 5  $\mu\text{L}$  of paraffin. 20  $\mu\text{L}$  of each paraffin mixed sample was then transferred to wells created in the agarose gel. A voltage of 165 V was applied to the gel and left to run for 40 minutes. The samples were pre-mixed with paraffin as this helped them settle within the wells of the gel.

#### 5.4.3.4 Lateral flow immunoassay

HRP-II (100  $\mu\text{g}/\text{mL}$ , 0.5  $\mu\text{L}$ ) and anti-IgG control (0.5  $\mu\text{L}$ ) were spotted onto the nitrocellulose strip (8  $\mu\text{m}$  pore size), one above the other, and left to dry. 90  $\mu\text{L}$  running buffer (10 mM PB + 1 % BSA + 0.05 % Tween-20) and 10  $\mu\text{L}$  Ab-PEG-Au conjugate were added to a well on the running plate. Once dry, the strip was placed

in the well which initiated flow. 100  $\mu\text{L}$  running buffer was used as a wash once the running buffer/conjugate mixture had been fully absorbed by the strip.

SERS analysis of the lateral flow test spots was carried out on a Renishaw inVia Raman spectrometer equipped with 633 nm laser excitation (4 mW), a  $\times 5$  objective and a 3 s acquisition time.

#### *5.4.4 Fabrication and running of lateral flow immunoassay*

HiFlow Plus 180 2mil membranes, cellulose fiber sample pads, and glass fiber diagnostic pads were purchased from Merck Millipore. To fabricate the strip the conjugate and absorbent pads were attached to both ends of the membrane with an overlap between them. The complete strip was then cut into individual strips ( $\sim 5$  mm in width).

A running buffer composed of 1 % BSA + 0.05 % Tween-20 in PB was used for all lateral flow experiments. 300  $\mu\text{g}/\text{mL}$  mouse monoclonal HRP-II capture antibody (0.8  $\mu\text{L}$ ) was spotted onto the HiFlow nitrocellulose membrane, with an anti-IgG control spotted above (0.8  $\mu\text{L}$ ) and left to dry. 80  $\mu\text{L}$  of running buffer, 10  $\mu\text{L}$  Au-Ab conjugates (0.7 nM), and 10  $\mu\text{L}$  of target HRP-II antigen or blank were placed in a plate well and placed on a plate shaker for 15 minutes. The lateral flow strips were then placed in the wells and the running buffer mixture allowed to run along the strip. Once all the sample in the well had been absorbed, a further aliquot of running buffer was added to the well as a wash (100  $\mu\text{L}$ ). Once dried the strips were analysed *via* SERRS and colourimetry measurements.

##### *5.4.4.1 SERRS quantification*

Raman mapping of the test spots was performed using a Renishaw inVia Raman spectrometer equipped with 633 nm laser excitation (0.8 mW) and an 1800  $\text{l mm}^{-1}$  grating. Raman images of uninfected and infected malaria tissue were recorded using a  $\times 5$  objective with an integration time of 4 s per spectrum, a step size of 150  $\mu\text{m}$ , and in the spectral range of 680 – 1780  $\text{cm}^{-1}$ .

Single point spectra of the test spots were also collected using a Renishaw inVia Raman spectrometer with a 633 nm laser excitation (0.8 mW) and a  $\times 5$  objective.

Samples were run in triplicate, with 20 spectra collected from each using a 9 s acquisition time

#### *5.4.4.2 Colourimetric quantification*

The lateral flow strips were scanned with an 8-bit EPSON V370 Flatbed scanner using a resolution of 1200 dpi. ImageJ software was then used to generate the RGB response from each test spot. The signal of the Green channel was quantified as it was the most sensitive to the colour produced by the gold colloid. A normalised signal was calculated for each response by subtracting it from the maximum RGB value of 255. Normalised signals for each replicate concentration were then averaged and a calibration curve built.

#### *5.4.5 Fabrication and running of the 3D- $\mu$ PAD*

Devices were manufactured using a combination of nylon membrane for the capture layer (pore size  $\sim 0.45 \mu\text{m}$ ) and chromatography paper for the other layers (pore size  $\sim 25 \mu\text{m}$ ). The conjugate storage layer and the capture layer were pre-treated before assembly and running of the device.

*Conjugate layer treatment:* 10 % BSA in PB (3  $\mu\text{L}$ ) was applied to this layer and allowed to dry at room temperature (R.T.). Following this, the Au-Ab conjugate was applied at a concentration of 0.4 nM (5  $\mu\text{L}$ ). This was left to dry at R.T.

*Capture layer treatment:* Mouse monoclonal HRP-II capture antibody (0.5 mg/mL, 2  $\mu\text{L}$ ) was applied and left to dry at R.T. Once dried, 3  $\mu\text{L}$  of blocking buffer was then applied and again left to dry at R.T.

Following treatment of these layers, the device was assembled and ready to be used. Serial dilution of the target HRP-II antigen was carried out in sample diluent to give a working range of 100 – 0.75 ng/mL. To initiate an assay, 30  $\mu\text{L}$  of target antigen or blank was applied to the top sample addition layer of the device. After the sample was completely absorbed into the top layer of the device, 40  $\mu\text{L}$  of wash buffer was added to drive the flow of fluid through the device and reduce non-specific binding at the capture layer. All assays were completed 15 – 20 minutes after the addition of the sample.



To determine the results of the paper-based immunoassay the three layers above the capture layer were then peeled back. This allowed the results of the assay to be interpreted by SERRS or by an electronic reader.

*Blocking buffer: 1 % skimmed milk + 5 % sucrose + 0.1 % Tween-20 in PB.*

*Sample diluent: 1 % BSA + 0.1 % Tween-20 in PB.*

*Wash buffer: 0.1 % Tween-20 in PB.*

#### *5.4.5.1 SERRS quantification*

SERRS analysis of the capture zones was carried out on a portable, handheld CBEx spectrometer from Snowy Range Instruments, equipped with a 638 nm excitation laser. Individual capture layers were mounted on top of the point and shoot tip using a 3D-printed holder. Spectra were collected using the orbital raster scanning feature of the CBEx instruments to gain a representative measurement of the entire capture area. A laser power of 26.7 mW, and 0.1 s acquisition time were also used.

#### *5.4.5.2 Colourimetric quantification*

The capture layers were scanned with an 8-bit EPSON V370 Flatbed scanner using a resolution of 1200 dpi. ImageJ software was then used to generate the RGB response from each capture zone, as with the lateral flow test spots. The normalised signal was calculated for each concentration by subtracting it from the maximum RGB value of 255. Normalised signals for each replicate concentration were then averaged and a calibration curve built.

#### *5.4.5.3 3D- $\mu$ PAD selectivity*

25 ng/mL HRP-II and 25 ng/mL CRP, both diluted in sample diluent, were applied to separate devices to test the selectivity of the assay in this format. The layers were treated, and the device initiated as described above. Both capture layers were then analysed with SERRS using the handheld CBEx spectrometer as before. Only one replicate for each antigen was carried out, with the results shown being an average of 20 spectra taken from each capture layer.

#### 5.4.5.4 HRP-II detection in biologically relevant matrix

The ability of the device to detect target antigen in a biologically relevant matrix was also tested. To achieve this GR Vivid™ Plasma Separation Membrane was added to the top of the sample addition layer.

Whole human blood was obtained through a finger prick test. A 10  $\mu\text{L}$  aliquot was then spiked with HRP-II (1000 ng/mL, 2  $\mu\text{L}$ ) and 8  $\mu\text{L}$  PB added to give a final concentration of 100 ng/mL antigen. CRP was also spiked into blood at the same concentration to be used as a negative control. 20  $\mu\text{L}$  of the spiked blood sample was then applied to the plasma separation membrane that had been attached to the top layer of the device and allowed to absorb through the layers. Washes were then added to facilitate the flow (50  $\mu\text{L}$  0.1 % Tween-20 in PB). At the end of the run the capture zone was revealed and a further wash (20  $\mu\text{L}$ ) was applied directly onto the capture zone to clean the spot of any RBCs that may have flowed through and were adding to the red colour of the spot. Both capture layers, for the target and negative control, were analysed by SERRS using the handheld CBEx spectrometer as described above.

## 6 Conclusions

---

This work has demonstrated the use of label-free Raman spectroscopic imaging and SERRS for the detection of malaria parasite infection. Initial work was carried out as a proof-of-concept to highlight the ability of Raman imaging to differentiate malaria parasite infected tissue from non-infected samples. By applying a combination of PCA along with a 532 nm laser excitation, to give resonance Raman information mainly from heme-based tissue components, and a 785 nm excitation to focus on non-resonant biological components, very clear discrimination of *P. berghei* infected tissue sections from the non-infected was achieved. Chemometric analysis of the resonance enhancement data displayed an overall increase in heme-based Raman vibrations within the infected tissue which correlated with the accumulation of Hz within the spleen. The presence of key Hz peaks ( $\sim 1370$ ,  $1529$ ,  $1588$ , and  $1628\text{ cm}^{-1}$ ) that also matched closely with the Hz reference spectrum confirmed detection of this insoluble malaria pigment. It was also concluded that with an increase in Hz content, observed at higher levels of infection, there were corresponding changes to Hb and other lipid/nucleic acid vibrations. Other non-resonant biological components were found to be contributing to the separation of the infected samples from the non-infected, including protein tyrosine, amide III bands of proteins. Separation due to lipids however, was not thought to be occurring due to the lack of the prominent lipid peak at  $\sim 1448\text{ cm}^{-1}$ . However, as a 532 nm laser excitation was applied here, resonance effects from exciting in the region of the Q-absorption bands of Hb and Hz led to signals from these heme-based components dominating the spectra and contributions from other biological components being much smaller.

Moving away from a resonant laser excitation allowed complementary biological information to be gained from the tissue sections. From PCA of tissue data recorded with a 785 nm laser excitation, two key peaks assigned to proteins phenylalanine ( $1004\text{ cm}^{-1}$ ) and collagen ( $1448\text{ cm}^{-1}$ ) appeared to be altered within the *P. berghei* infected tissue compared with the control. Other biological components including amide III, multiple  $\text{CH}_3\text{CH}_2$  twisting modes of proteins, and phospholipids were found

to be important in describing the alteration of spleen tissue in the infected state. This analysis highlighted that *P. berghei* malaria infection within the spleen had altered the concentration and/or the composition of these assigned biomolecules, relative to the non-infected control samples. This analysis also concluded that *P. berghei* infection led to a decrease in the total amount of some biomolecules within the mouse spleen when compared to the control, mainly  $\sim 1255\text{ cm}^{-1}$  (amide III and  $\text{CH}_2$  lipids),  $1104\text{ cm}^{-1}$  (phenylalanine), and  $1128\text{ cm}^{-1}$  (phospholipids and Hb vibrations,  $\nu_5$ ). The changes seen in the infected tissue relative to the non-infected, with analysis at 532 nm and 785 nm, were also reflected within the intensity ratio maps and empirical analysis.

From the small *in-vivo* and *ex-vivo* data sets collected using the in-house built portable Raman spectrometer, key biological components including amide I and III proteins, collagen, phenylalanine, and fatty acids were detected from whole intact mice spleens and livers. Although no statistically relevant separation in the PCA model was observed, this experiment highlighted the capability of Raman spectroscopy to detect biological signals from *in-vivo* models.

To date, the application of Raman spectroscopy within malaria diagnosis has focussed heavily on the detection of hemozoin within erythrocytes by exploiting the huge resonant enhancements from Hz bands.<sup>75–78,188</sup> Hobro *et al.*<sup>189</sup> also applied Raman spectroscopy to study the biochemical changes that occur within macrophages following Hz uptake but work had not gone further to investigate its detection within tissue. This work applies the technique of Raman spectroscopy to a challenging area of malaria diagnosis and highlights its possibility as a detection tool for tissue burden. To be applied as a method to detect tissue burden *in-vivo*, considerations about the maximum penetration depth capability into tissue and the ability to penetrate through obscuring barriers, i.e. through the skull into the microvasculature of the brain, must be made and are not capable with the standard Raman techniques studied in this work. Further work must look at moving towards a SORS set-up to collect enough relevant biological information, at depth, from the large sample

volume of whole organs to allow clear differentiation of infected from non-infected samples *in-vivo*.

Further studies in this work to evaluate the ability of SERRS to enhance the detection capabilities of RDTs for the malaria *P. falciparum* specific antigen, HRP-II, showed overall success. When applied to the traditional lateral flow immunoassay, good quantifiable detection levels of HRP-II, down to 5 ng/mL, and a theoretical LoD of 65.3 pg/mL were achieved with SERRS. These concentrations translated to ~65 and <1 parasite/ $\mu$ L, respectively. Both were below the standard detection range of 100 parasites/ $\mu$ L that is achieved through blood smear analysis. However, as this analysis was carried out on a large benchtop confocal Raman microscope it would not be suitable for in-field/point-of-care diagnostics that is the target of RDTs.

To develop a more robust RDT that had the capability to be applied in-field, a 3D- $\mu$ PAD coupled with detection on a portable, handheld CBEx Raman spectrometer was studied. This device gave a theoretical LoD of 1.68 ng/mL (~22 parasites/ $\mu$ L) which surpassed the average of 100 parasites/ $\mu$ L from a blood smear and was close to the parasitemia levels that a skilled technician can detect (5 – 10 parasites/ $\mu$ L). Detection of HRP-II antigen, at a final concentration of 100 ng/mL, was also shown to be possible from whole human blood samples using this 3D- $\mu$ PAD coupled with SERRS. Although a large amount of non-specific binding occurred in the negative sample, this initial experiment demonstrated the potential of this simple paper-based diagnostic test to be used with clinically relevant samples at a point-of-care setting.

Finally, to show the added detection sensitivity gained by coupling the devices with SERRS, results were also quantified with a traditional colourimetric measurement. Large standard deviations were encountered when analysing the lateral flow immunoassays with this technique and resulted in a much higher theoretical LoD of 34.7 ng/mL (~454 parasites/ $\mu$ L) compared to that calculated using SERRS. Reproducibility was better for the analysed 3D- $\mu$ PAD capture zones, however, again a much higher theoretical LoD was calculated, 25.5 ng/mL (~333 parasites/ $\mu$ L), compared to that gained using SERRS (1.68 ng/mL). This demonstrated the increase

in detection sensitivity that was achieved in this work by coupling the RDTs with SERRS.

The use of lateral flow immunochromatographic RDTs for malaria diagnosis is well established and many reviews have been published which compare the performance of these tests to detect both *P. falciparum* specific and *non-falciparum* species antigens.<sup>64,68,73,190</sup> However, the application of  $\mu$ PADs for biomarker quantification and disease detection is an emerging field with great potential to be applied in resource-challenged settings. Examples of the applications of these paper-based devices have included the detection of infectious human norovirus<sup>191</sup> and measuring enzymatic markers of liver function.<sup>153</sup> Recently, Deraney *et al.*<sup>168</sup> demonstrated the analytical performance of singleplex and multiplex paper-based assays to detect malaria HRP-II, malaria  $p$ LDH, and dengue NS1 type 2 biomarkers. This work showed success in detection of these biomarkers by applying colourimetric analysis to the detection zones, with an LoD for singleplex HRP-II of 20.3 ng/mL ( $\sim$ 265 parasites/ $\mu$ L) that was comparable to the HRP-II colourimetric LoD achieved here (25.5 ng/mL). However, the work shown here goes further by successfully demonstrating how the coupling of these paper-based devices with SERRS detection can greatly improve device sensitivity by achieving an LoD of 1.68 ng/mL ( $\sim$ 22 parasites/ $\mu$ L) for HRP-II. To move this work forward the singleplex detection of HRP-II within whole blood samples must be optimised. Improvement of the attachment of the plasma separation membrane to the top layer of the device may lead to more efficient capturing of the cellular components of the blood and reduce interference on the detection zone. SERRS multiplex detection of *P. falciparum* and *non-falciparum* malaria antigens should also be investigated as this would lead to a further advantage over traditional lateral flow immunochromatographic assays that typically can only detect single antigens. This would require a paper device with multiple channels and separate detection zones for each target analyte, such as that demonstrated by Deraney *et al.*<sup>168</sup>

Overall, this work demonstrated the versatility that Raman spectroscopy and its surface enhanced analogues possess for use in biological applications and disease

detection. Differentiation of parasite infected tissue from non-infected was possible by using a combination of Raman and resonance Raman enhancement. Whereas, low limits of detection of a malaria specific biomarker, compared to current detection methods, was achievable by using SERRS. With the development and continuing improvement in sensitivity of portable Raman spectrometers,<sup>192</sup> this opens up the possibility of Raman spectroscopy to be applied in-field and at the point-of-care to detect antigens specific to infection within blood or to gain biochemical information from millimetre tissue depths *in-vivo* and determine tissue burden.

## 7 References

---

- (1) Rosi, N. L.; Mirkin, C. A. *Chem. Rev.* **2005**, *105* (4), 1547.
- (2) Turkevich, J.; Stevenson, P. C.; Hillier, J. *Discuss. Faraday. Soc.* **1951**, *11*, 55.
- (3) Lee, P. C.; Meisel, D. *J. Phys. Chem.* **1982**, *86*, 3391.
- (4) Mandal, M.; Kundu, S.; Ghosh, S. K.; Panigrahi, S.; Sau, T. K.; Yusuf, S. M.; Pal, T. *J. Colloid Interface Sci.* **2005**, *286*, 187.
- (5) Bigall, N. C.; Härtling, T.; Klose, M.; Simon, P.; Eng, L. M.; Eychmüller, A. *Nano Lett.* **2008**, *8*, 4588.
- (6) Freestone, I.; Meeks, N.; Sax, M.; Higgitt, C. *Gold Bull.* **2007**, *40*, 270.
- (7) González-solís, J. L.; Luévano-colmenero, G. H.; Moreno, L. De. *Laser Ther.* **2013**, *22*, 37.
- (8) Sepúlveda, B.; Angelomé, P. C.; Lechuga, L. M.; Liz-Marzán, L. M. *Nano Today* **2009**, *4*, 244.
- (9) Gracie, K.; Correa, E.; Mabbott, S.; Dougan, J. A.; Graham, D.; Goodacre, R.; Faulds, K. *Chem. Sci.* **2014**, *5* (3), 1030.
- (10) Frens, G. *Nat. Phys. Sci.* **1973**, *241*, 20.
- (11) Lee, N. S.; Morris, M. D.; Sheng, R. S.; Schopfer, L. M. *J. Am. Chem. Soc.* **1986**, *108*, 6179.
- (12) Shirtcliffe, N.; Nickel, U.; Schneider, S. *J. Colloid Interface Sci.* **1999**, *211* (1), 122.
- (13) Arruebo, M.; Valladares, M.; González-Fernández, Á. *J. Nanomater.* **2009**, *2009*.
- (14) Hammond, J. L.; Bhalla, N.; Rafiee, S. D.; Estrela, P. *Biosensors* **2014**, *4* (2), 172.
- (15) Hu, M.; Chen, J.; Li, Z.-Y.; Au, L.; Hartland, G. V.; Li, X.; Marquez, M.; Xia, Y. *Chem. Soc. Rev.* **2006**, *35* (11), 1084.
- (16) Mie, G. *Ann. Phys.* **1908**, *330*, 377.
- (17) Ghosh, S. K.; Pal, T. *Chem. Rev.* **2007**, *107* (11), 4797.
- (18) Orendorff, C. J.; Sau, T. K.; Murphy, C. J. *Small* **2006**, *2* (5), 636.
- (19) Liu, W.-T. *J. Biosci. Bioeng.* **2006**, *102*, 1.
- (20) Oldenburg, S. J.; Genick, C. C.; Clark, K. A.; Schultz, D. A. *Anal. Biochem.* **2002**, *309* (1), 109.



- (21) Xu, W.; Xue, X.; Li, T.; Zeng, H.; Liu, X. *Angew. Chemie - Int. Ed.* **2009**, *48* (37), 6849.
- (22) Reynolds, R. A.; Mirkin, C. A.; Letsinger, R. L. *J. Am. Chem. Soc.* **2000**, *122*, 3795.
- (23) Nietzold, C.; Lisdat, F. *Analyst* **2012**, *137*, 2821.
- (24) Smekal, A. *Naturwissenschaften* **1923**, *11* (43), 873.
- (25) Raman, C. V.; Krishnan, K. S. *Nature* **1928**, *121*, 501.
- (26) Smith, E.; Dent, G. *Modern Raman Spectroscopy—A Practical Approach*; John Wiley & Sons, Ltd: Chichester, UK, 2005.
- (27) Kneipp, K.; Kneipp, H.; Itzkan, I.; Dasari, R. R.; Feld, M. S. *J. Phys. Condens. Matter* **2002**, *14*, R597.
- (28) Larkin, P. J. In *Infrared and Raman Spectroscopy: principles and spectral interpretation*; Elsevier Inc., 2011; pp 7–25.
- (29) Rostron, P.; Gaber, S.; Gaber, D. *Int. J. Eng. Tech. Res.* **2016**, *6*, 50.
- (30) Ferraro, J. R.; Nakamoto, K.; Brown, C. W. *Introductory Raman Spectroscopy: Second Edition*; 2003.
- (31) Butler, H. J.; Ashton, L.; Bird, B.; Cinque, G.; Curtis, K.; Esmonde-white, K.; Fullwood, N. J.; Gardner, B.; Martin-, P. L.; Walsh, M. J.; Mcainsh, M. R.; Stone, N.; Martin, F. L.; Butler, H. J.; Martin-hirsch, P. L. *Nat. Protoc.* **2016**, *11* (4), 1.
- (32) Robert, B. *Photosynth. Res.* **2009**, *101*, 147.
- (33) Fleischmann, M.; Hendra, P. J.; McQuillan, A. J. *Chem. Phys. Lett.* **1974**, *26* (2), 163.
- (34) Jeanmaire, D. L.; Van Duyne, R. P. *J. Electroanal. Chem.* **1977**, *84* (1), 1.
- (35) Albrecht, M. G.; Creighton, J. A. *J. Am. Chem. Soc.* **1977**, *99* (15), 5215.
- (36) Smith, W. E. *Chem. Soc. Rev.* **2008**, *37* (5), 955.
- (37) Faulds, K.; Hernandez-Santana, A.; Smith, W. E. *Spectrosc. Prop. Inorg. Organomet. Compd.* **2010**, *41*, 1.
- (38) McNay, G.; Eustace, D.; Smith, W. E.; Faulds, K.; Graham, D. *Appl. Spectrosc.* **2011**, *65* (8), 825.
- (39) Faulds, K.; Barbagallo, R. P.; Keer, J. T.; Smith, W. E.; Graham, D. *Analyst* **2004**, *129* (7), 567.
- (40) Sirimuthu, N. M. S.; Syme, C. D.; Cooper, J. M. *Anal. Chem.* **2010**, *82* (17), 7369.

- (41) Frame, L.; Brewer, J.; Lee, R.; Faulds, K.; Graham, D. *Analyst* **2018**, *143*, 157.
- (42) Gendrin, C.; Roggo, Y.; Collet, C. *J. Pharm. Biomed. Anal.* **2008**, *48* (3), 533.
- (43) Larmour, I. A.; Faulds, K.; Graham, D. *Anal. Methods* **2010**, *2* (9), 1230.
- (44) McAughtrie, S.; Lau, K.; Faulds, K.; Graham, D. *Chem. Sci.* **2013**, *4* (9), 3566.
- (45) World Health Organisation. *World Malaria Report 2017*; 2017.
- (46) Winzeler, E. A. *Nature* **2008**, *455*, 751.
- (47) Kantele, A.; Jokiranta, T. S. *Clin. Infect. Dis.* **2011**, *52* (11), 1356.
- (48) NHS, N. H. S. Malaria NHS-UK <https://www.nhs.uk/Conditions/Malaria/> (accessed Nov 20, 2017).
- (49) CDC - Centers for Disease Control and Prevention. CDC - Malaria <https://www.cdc.gov/malaria/about/disease.html> (accessed Nov 20, 2017).
- (50) Vaughan, A. M.; Aly, A. S. I.; Kappe, S. H. I. *Cell Host Microbe* **2008**, *4* (3), 209.
- (51) Klein, E. Y. *Int. J. Antimicrob. Agents* **2013**, *41* (4), 311.
- (52) Jain, P.; Chakma, B.; Patra, S.; Goswami, P. *Biomed Res. Int.* **2014**, *2014*, 1.
- (53) Moody, A. *Clin. Microbiol. Rev.* **2002**, *15* (1), 66.
- (54) Rifai, N.; Gillette, M. A.; Carr, S. A. *Nat. Biotechnol.* **2006**, *24*, 971.
- (55) Frosch, T.; Koncarevic, S.; Becker, K.; Popp, J. *Analyst* **2009**, *134* (6), 1126.
- (56) Frosch, T.; Koncarevic, S.; Zedler, L.; Schmitt, M.; Schenzel, K.; Becker, K.; Popp, J. *J. Phys. Chem. B* **2007**, *111*, 11047.
- (57) David, P.; Jr, J. S. In *Biopolymers Online*; Wiley-VCH Verlag & Co. KGaA, 2005; pp 129–137.
- (58) Coronado, L. M.; Nadovich, C. T.; Spadafora, C. *Biochim. Biophys. Acta* **2014**, *1840* (6), 2032.
- (59) Inyushin, M.; Kucheryaviih, Y.; Kucheryaviih, L.; Rojas, L.; Khmelinskii, I.; Makarov, V. *Sci. Rep.* **2016**, *6* (May), 26212.
- (60) Slater, A.; Swiggard, W.; Orton, B.; Flitter, W.; Goldberg, D.; Cerami, A.; Henderson, G. *Proc. Natl. Acad. Sci.* **1991**, *88*, 325.
- (61) Boura, M.; Frita, R.; Góis, A.; Carvalho, T.; Hänscheid, T. *Trends Parasitol.* **2013**, *29* (10), 469.
- (62) Pagola, S.; Stephens, P. W.; Bohle, D. S.; Kosar, a D.; Madsen, S. K. *Nature* **2000**, *404* (6775), 307.
- (63) Parra, M. E.; Evans, C. B.; Taylor, D. W. *J. Clin. Microbiol.* **1991**, *29*, 1629.
- (64) Murray, C. K.; Gasser, R. A.; Magill, A. J.; Miller, R. S. *Clin. Microbiol. Rev.*

**2008**, 21 (1), 97.

- (65) Verma, P.; Biswas, S.; Mohan, T.; Ali, S.; Rao, D. N. *Indian J Med Res.* **2013**, 138 (6), 977.
- (66) Mathema, V. B.; Na-Bangchang, K. *Asian Pac. J. Trop. Med.* **2015**, 8 (4), 253.
- (67) WHO. *New Perspectives: Malaria Diagnosis: Report of a Joint WHO/USAID Informal Consultation*; 2000.
- (68) Wongsrichanalai, C.; Barcus, M. J.; Muth, S.; Sutamihardja, A.; Wernsdorfer, W. H. *Am. J. Trop. Med. Hyg.* **2007**, 77, 119.
- (69) Tangpukdee, N.; Duangdee, C.; Wilairatana, P.; Krudsood, S. *Korean J. Parasitol.* **2009**, 47, 93.
- (70) Payne, D. *Bull. World Health Organ.* **1988**, 66, 621.
- (71) Cho, S.; Kim, S.; Kim, Y.; Park, Y. *Trends Biotechnol.* **2012**, 30 (2), 71.
- (72) CDC - Centers for Disease Control and Prevention. CDC - Malaria Diagnosis [https://www.cdc.gov/malaria/diagnosis\\_treatment/diagnosis.html](https://www.cdc.gov/malaria/diagnosis_treatment/diagnosis.html) (accessed Nov 22, 2017).
- (73) World Health Organisation. *Malaria Rapid Diagnostic Test Performance*; 2011; Vol. 3.
- (74) Wood, B. R.; Langford, S. J.; Cooke, B. M.; Glenister, F. K.; Lim, J.; McNaughton, D. *FEBS Lett.* **2003**, 554 (3), 247.
- (75) Ong, C. W.; Shen, Z. X.; Ang, K. K. H.; Kara, U. A. K.; Tang, S. H. *Appl. Spectrosc.* **1999**, 53 (9), 1097.
- (76) Wood, B. R.; Hermelink, A.; Lasch, P.; Bambery, K. R.; Webster, G. T.; Khiavi, M. A.; Cooke, B. M.; Deed, S.; Naumann, D.; McNaughton, D. *Analyst* **2009**, 134 (6), 1119.
- (77) Hobro, A. J.; Konishi, A.; Coban, C.; Smith, N. I. *Analyst* **2013**, 138 (14), 3927.
- (78) Ong, C. W.; Shen, Z. X.; Ang, K. K. H.; Kara, U. A. K.; Tang, S. H. *Appl. Spectrosc.* **2002**, 56 (9), 1126.
- (79) Chen, K.; Yuen, C.; Aniwah, Y.; Preiser, P.; Liu, Q. *Nat. Publ. Gr.* **2016**, 6, 1.
- (80) Ferrer, M.; Martin-Jaular, L.; De Niz, M.; Khan, S. M.; Janse, C. J.; Calvo, M.; Heussler, V.; Del Portillo, H. a. *Parasitol. Int.* **2014**, 63 (1), 195.
- (81) Del Portillo, H. A.; Ferrer, M.; Brugat, T.; Martin-Jaular, L.; Langhorne, J.; Lacerda, M. V. G. *Cell. Microbiol.* **2012**, 14 (3), 343.
- (82) Engwerda, C. R.; Beattie, L.; Amante, F. H. *Trends Parasitol.* **2005**, 21 (2), 75.
- (83) Autino, B.; Corbett, Y.; Castelli, F.; Taramelli, D. *Mediterr. J. Hematol. Infect. Dis.* **2012**, 4 (1), 1.

- (84) Aird, W. C.; Mosnier, L. O.; Fairhurst, R. M. *Blood* **2014**, *123* (2), 163.
- (85) Khoury, D. S.; Cromer, D.; Best, S. E.; James, K. R.; Kim, P. S.; Engwerda, C. R.; Haque, A.; Davenport, M. P. *Infect. Immun.* **2014**, *82* (1), 212.
- (86) Walther, M.; Cunnington, A. J.; Bretscher, M. T. *J. Infect.* **2014**, *67* (3), 220.
- (87) David, P. H.; Hommel, M.; Miller, L. H.; Udeinya, I. J.; Oligino, L. D. *Proc. Natl. Acad. Sci.* **1983**, *80* (16), 5075.
- (88) Medana, I. M.; Day, N. P. J.; Roberts, R.; Sachanonta, N.; Turley, H.; Pongponratn, E.; Hien, T. T.; White, N. J.; Turner, G. D. H. *Histopathology* **2010**, *57* (2), 282.
- (89) Franke-Fayard, B.; Janse, C. J.; Cunha-Rodrigues, M.; Ramesar, J.; Buscher, P.; Que, I.; Lowik, C.; Voshol, P. J.; den Boer, M. A. M.; van Duinen, S. G.; Febbraio, M.; Mota, M. M.; Waters, A. P. *Proc. Natl. Acad. Sci.* **2005**, *102* (32), 11468.
- (90) Silamut, K.; Phu, N. H.; Whitty, C.; Turner, G. D. H.; Louwrier, K.; Mai, N. T. H.; Simpson, J. A.; Hien, T. T.; White, N. J. *Am. J. Pathol.* **1999**, *155* (2), 395.
- (91) Taylor, T. E.; Fu, W. J.; Carr, R. A.; Whitten, R. O.; Mueller, J. G.; Fosiko, N. G.; Lewallen, S.; Liomba, N. G.; Molyne. *Nat. Me* **2004**, *10*, 143.
- (92) Franke-Fayard, B.; Fonager, J.; Braks, A.; Khan, S. M.; Janse, C. J. *PLoS Pathog.* **2010**, *6* (9), 1.
- (93) Movasaghi, Z.; Rehman, S.; Rehman, I. U. *Appl. Spectrosc. Rev.* **2007**, *42* (5), 493.
- (94) de Juan, A.; Piqueras, S.; Maeder, M.; Hancewicz, T.; Duponchel, L.; Tauler, R. In *Infrared and Raman Spectroscopic Imaging*; Reiner Salzer, Heinz W. Siesler: Weinheim, 2014; pp 65–106.
- (95) Kochan, K.; Marzec, K. M.; Chruszcz-Lipska, K.; Jaształ, A.; Maslak, E.; Musiolik, H.; Chłopicki, S.; Baranska, M. *Analyst* **2013**, *138* (14), 3885.
- (96) Teh, S. K.; Zheng, W.; Ho, K. Y.; Teh, M.; Yeoh, K. G.; Huang, Z. *Br. J. Cancer* **2008**, *98* (2), 457.
- (97) Krafft, C.; Codrich, D.; Pelizzo, G.; Sergio, V. *Analyst* **2008**, *133* (3), 361.
- (98) Haka, A. S.; Shafer-Peltier, K. E.; Fitzmaurice, M.; Crowe, J.; Dasari, R. R.; Feld, M. S. *Proc. Natl. Acad. Sci. U. S. A.* **2005**, *102* (35), 12371.
- (99) Feng, S.; Lin, J.; Cheng, M.; Li, Y. Z.; Chen, G.; Huang, Z.; Yu, Y.; Chen, R.; Zeng, H. *Appl. Spectrosc.* **2009**, *63* (10), 1089.
- (100) Huang, Z.; Li, Z.; Chen, R.; Chen, G.; Lin, D.; Xi, G.; Chen, Y.; Lin, H.; Lei, J. *J. Phys. Conf. Ser.* **2011**, *277* (1), 1.
- (101) Cinta Pinzaru, S.; Andronie, L. M.; Domsa, I.; Cozar, O.; Astilean, S. *J. Raman*

- Spectrosc.* **2008**, *39*, 331.
- (102) Schlücker, S.; Küstner, B.; Punge, A.; Bonfig, R.; Marx, A.; Ströbel, P. *J. Raman Spectrosc.* **2006**, *37* (7), 719.
- (103) Matousek, P.; Stone, N. *Analyst* **2009**, *134* (6), 1058.
- (104) Stone, N.; Matousek, P. *Cancer Res.* **2008**, *68* (11), 4424.
- (105) Keller, M. D.; Majumder, S. K.; Mahadevan-Jansen, A. *Opt. Lett.* **2009**, *34* (7), 926.
- (106) Nicolson, F.; Jamieson, L. E.; Mabbott, S.; Shand, N. C.; Graham, D.; Faulds, K. *J. Raman Spectrosc.* **2017**, *48* (12), 1828.
- (107) Kerr, L. T.; Byrne, H. J.; Hennelly, B. M. *Anal. Methods* **2015**, *7* (12), 5041.
- (108) Smith, A. M.; Mancini, M. C.; Nie, S. *Nat. Nanotechnol.* **2009**, *4* (11), 710.
- (109) Matousek, P.; Stone, N. *Chem. Soc. Rev.* **2016**, *45* (7), 1794.
- (110) Spiro, T. G.; Strekas, T. C. *Proc. Nat. Acad. Sci. USA* **1972**, *69* (9), 2622.
- (111) Spiro, T. G.; Strekas, T. C. *J. Am. Chem. Soc.* **1974**, *96* (2), 338.
- (112) Polakovs, M.; Mironova-Ulmane, N.; Kurjane, N.; Reinholds, E.; Grube, M. *Proc. SPIE* **2008**, *7142*, 1.
- (113) Dayer, M. R.; Moosavi-Movahedi, A. A.; Dayer, M. S. *Protein Pept. Lett.* **2010**, *17*, 473.
- (114) Tissue-Tek O.C.T Compound and Cryomolds <http://www.sakura.eu/Our-products/item/11/Cryotomy/48/Tissue-Tek-OCT-Compound-and-Cryomolds> (accessed Sep 15, 2017).
- (115) Huang, W. M.; Gibson, S. J.; Facer, P.; Gu, J.; Polak, J. M. *Histochemistry* **1983**, *77* (2), 275.
- (116) Huang, Z.; McWilliams, A.; Lui, H.; McLean, D. I.; Lam, S.; Zeng, H. *Int. J. cancer* **2003**, *107* (6), 1047.
- (117) Egan, T. J.; Rossa, D. C.; Adamsb, P. A. *FEBS Lett.* **1994**, *352*, 54.
- (118) Egan, T. J.; Mavuso, W. W.; Ncokazi, K. K. *Biochemistry* **2001**, *40* (1), 204.
- (119) Rusciano, G.; De Luca, A. C.; Pesce, G.; Sasso, A. *Sensors* **2008**, *8* (12), 7818.
- (120) Parekh, F. K.; Davison, B. B.; Gamboa, D.; Hernandez, J.; Branch, O. H. *Am. J. Trop. Med. Hyg.* **2010**, *83* (5), 973.
- (121) Frita, R.; Carapau, D.; Mota, M. M.; Hänscheid, T. *Malar. Res. Treat.* **2012**, *2012*, 1.
- (122) Asiala, S. M.; Shand, N. C.; Faulds, K.; Graham, D. *ACS Appl. Mater. Interfaces* **2017**, *9* (30), 25488.

- (123) Feng, G.; Ochoa, M.; Maher, J. R.; Awad, H. A.; Berger, A. J. *J. Biophotonics* **2017**, *10* (8), 990.
- (124) Buckley, K.; Kerns, J. G.; Gikas, P. D.; Birch, H. L.; Vinton, J.; Keen, R.; Parker, A. W.; Matousek, P.; Goodship, A. E. *IBMS Bonekey* **2014**, *11* (October), 1.
- (125) Sharma, B.; Ma, K.; Glucksberg, M. R.; Van Duyne, R. P. *J. Am. Chem. Soc.* **2013**, *135* (46), 17290.
- (126) Cate, D. M.; Adkins, J. A.; Mettakoonpitak, J.; Henry, C. S. *Anal. Chem.* **2015**, *87* (1), 19.
- (127) Mutneja, M.; Mohan, C.; Long, K. D.; Das, C. *An Introduction to Antibodies and Their Applications*; EMD Millipore.
- (128) Immunoglobulin IgG Class <https://www.thermofisher.com/uk/en/home/life-science/antibodies/antibodies-learning-center/antibodies-resource-library/antibody-methods/immunoglobulin-igg-class.html> (accessed Feb 11, 2018).
- (129) Antibody Structure <http://absoluteantibody.com/antibody-resources/antibody-overview/antibody-structure/> (accessed Feb 2, 2018).
- (130) Hermanson, G. T. In *Bioconjugate Techniques (Third edition)*; 2013; pp 951–957.
- (131) Antibody Structure <http://www.elisa-antibody.com/elisa-antibody/elisa-antibody-structure> (accessed Jan 25, 2018).
- (132) Sela-Culang, I.; Kunik, V.; Ofra, Y. *Front. Immunol.* **2013**, *4* (OCT), 1.
- (133) Koczula, K. M.; Gallotta, A. *Essays Biochem.* **2016**, *60* (1), 111.
- (134) Posthuma-Trumpie, G. A.; Korf, J.; Van Amerongen, A. *Anal. Bioanal. Chem.* **2009**, *393* (2), 569.
- (135) Cytodiagnosics. Lateral Flow Immunoassays <http://www.cytodiagnosics.com/store/pc/Lateral-Flow-Immunoassays-d6.htm> (accessed Apr 29, 2018).
- (136) Morales-Narváez, E.; Naghdi, T.; Zor, E.; Merkoçi, A. *Anal. Chem.* **2015**, *87* (16), 8573.
- (137) Sharma, S. K.; Eblen, B. S.; Bull, R. L.; Donald, H.; Whiting, R. C.; Burr, D. H. *Appl. Environ. Microbiol.* **2005**, *71* (7), 3935.
- (138) Kolosova, A. Y.; Saeger, S. De. *Anal. Bioanal. Chem.* **2007**, *389*, 2103.
- (139) Liu, Y.; Wu, A.; Hu, J.; Lin, M.; Wen, M.; Zhang, X.; Xu, C.; Hu, X.; Zhong, J.; Jiao, L.; Xie, Y.; Zhang, C.; Yu, X.; Liang, Y.; Liu, X. *Anal. Biochem.* **2015**, *483* (1), 7.
- (140) Kuang, H.; Xing, C.; Hao, C.; Liu, L.; Wang, L.; Xu, C. *Sensors* **2013**, *13* (4), 4214.

- (141) Kim, Y. K.; Lim, S. I.; Cho, I. S.; Cheong, K. M.; Lee, E. J.; Lee, S. O.; Kim, J. B.; Kim, J. H.; Jeong, D. S.; An, B. H.; An, D. J. *J. Virol. Methods* **2015**, *225*, 4.
- (142) Blanco-Covián, L.; Montes-García, V.; Girard, A.; Fernández-Abedul, M. T.; Perez-Juste, J.; Pastoriza-Santos, I.; Faulds, K.; Graham, D.; Blanco-López, M. C. *Nanoscale* **2017**, *9*, 2051.
- (143) Fanjul-Bolado, P.; González-García, M. B.; Costa-García, A. *Talanta* **2004**, *64* (2), 452.
- (144) Cima-Cabal, M. D.; Méndez, F. J.; Vázquez, F.; García-Suárez, M. del M.; de los Toyos, J. R. *J. Immunoass. Immunochem.* **2001**, *22* (2), 99.
- (145) Wang, X.; Choi, N.; Cheng, Z.; Ko, J.; Chen, L.; Choo, J. *Anal. Chem.* **2017**, *89* (2), 1163.
- (146) Hwang, J.; Lee, S.; Choo, J. *Nanoscale* **2016**, *83* (22), 6778.
- (147) Rong, Z.; Xiao, R.; Xing, S.; Xiong, G.; Yu, Z.; Wang, L.; Jia, X.; Wang, K.; Cong, Y.; Wang, S. *Analyst* **2018**, *143*, 2115.
- (148) Liu, H. Bin; Du, X. J.; Zang, Y. X.; Li, P.; Wang, S. *J. Agric. Food Chem.* **2017**, *65* (47), 10290.
- (149) Lam, T.; Devadhasan, J. P.; Howse, R.; Kim, J. *Sci. Rep.* **2017**, *7* (1), 1.
- (150) Lisowski, P.; Zarzycki, P. K. *Chromatographia* **2013**, *76* (19–20), 1201.
- (151) Martinez, A. W.; Phillips, S. T.; Whitesides, G. M.; Carrilho, E. *Anal. Chem.* **2010**, *82* (1), 3.
- (152) Martinez, A. W.; Phillips, S. T.; Butte, M. J.; Whitesides, G. M. *Angew. Chemie - Int. Ed.* **2007**, *46* (8), 1318.
- (153) Vella, S. J.; Beattie, P.; Cademartiri, R.; Laromaine, A.; Martinez, A. W.; Phillips, S. T.; Mirica, K. A.; Whitesides, G. M. *Anal. Chem.* **2012**, *84* (6), 2883.
- (154) Zhou, M.; Yang, M.; Zhou, F. *Biosens. Bioelectron.* **2014**, *55*, 39.
- (155) Mentele, M. M.; Cunningham, J.; Koehler, K.; Volckens, J.; Henry, C. S. *Anal. Chem.* **2012**, *84* (10), 4474.
- (156) Rattanarat, P.; Dungchai, W.; Cate, D.; Volckens, J.; Chailapakul, O.; Henry, C. S. *Anal. Chem.* **2014**, *86* (7), 3555.
- (157) Jokerst, J. C.; Adkins, J. A.; Bisha, B.; Mentele, M. M.; Goodridge, L. D.; Henry, C. S. *Anal. Chem.* **2012**, *84* (6), 2900.
- (158) Burnham, S.; Hu, J.; Anany, H.; Brovko, L.; Deiss, F.; Derda, R.; Griffiths, M. W. *Anal. Bioanal. Chem.* **2014**, *406* (23), 5685.
- (159) Martinez, A. W.; Phillips, S. T.; Whitesides, G. M. *Proc. Natl. Acad. Sci.* **2008**, *105* (50), 19606.

- (160) Klasner, S. A.; Price, A. K.; Hoeman, K. W.; Wilson, R. S.; Bell, K. J.; Culbertson, C. T. *Anal. Bioanal. Chem.* **2010**, 397 (5), 1821.
- (161) Abe, K.; Suzuki, K.; Citterio, D. *Anal. Chem.* **2008**, 80 (18), 6928.
- (162) Li, X.; Tian, J.; Garnier, G.; Shen, W. *Colloids Surfaces B Biointerfaces* **2010**, 76 (2), 564.
- (163) Delaney, J. L.; Hogan, C. F.; Tian, J.; Shen, W. *Anal. Chem.* **2011**, 83 (4), 1300.
- (164) Carrilho, E.; Martinez, A. W.; Whitesides, G. M. *Anal. Chem.* **2009**, 81 (16), 7091.
- (165) Schonhorn, J. E.; Fernandes, S. C.; Rajaratnam, A.; Deraney, R. N.; Rolland, J. P.; Mace, C. R. *Lab Chip* **2014**, 14 (24), 4653.
- (166) Xia, Y.; Si, J.; Li, Z. *Biosens. Bioelectron.* **2016**, 77, 774.
- (167) Schonhorn, J. E.; Fernandes, S. C.; Rajaratnam, A.; Deraney, R. N.; Rolland, J. P.; Mace, C. R. *Lab Chip* **2014**, 14 (24), 4653.
- (168) Deraney, R. N.; Mace, C. R.; Rolland, J. P.; Schonhorn, J. E. *Anal. Chem.* **2016**, 88 (12), 6161.
- (169) Haiss, W.; Thanh, N. T. K.; Aveyard, J.; Fernig, D. G. *Anal. Chem.* **2007**, 79, 4215.
- (170) Bhui, D. K.; Bar, H.; Sarkar, P.; Sahoo, G. P.; De, S. P.; Misra, A. *J. Mol. Liq.* **2009**, 145 (1), 33.
- (171) Pandey, S.; Mewada, A.; Thakur, M.; Shinde, S.; Shah, R.; Oza, G.; Sharon, M. *J. Nanosci.* **2013**, 2013 (1), 1.
- (172) Nanocomposix. *Zeta Potential Analysis of Nanoparticles*; 2012.
- (173) Haiss, W.; Thanh, N. T. K.; Aveyard, J.; Fernig, D. G. *Anal. Chem.* **2007**, 79, 1.
- (174) Suri, S.; Ruan, G.; Winter, J.; Schmidt, C. E. In *Bioconjugate Techniques (Third edition)*; 2013; pp 360–388.
- (175) Tryptophan, M. In *Bioconjugate Techniques (Third edition)*; 2013; pp 465–505.
- (176) Thermo Fisher Scientific Inc. *Crosslinking Technical Handbook*; 2012.
- (177) BBI - HRP2 (Malaria) mouse monoclonal antibody  
<https://www.bbisolutions.com/en/hrp2-malaria-mouse-monoclonal-antibody-1.html> (accessed May 3, 2018).
- (178) EMD Merck Millipore. *Rapid Lateral Flow Test Strips: Considerations for Product Development*; 2013.
- (179) WHO. *Parasitological confirmation of malaria diagnosis*; 2009.



- (180) Garcia, L. *Determination of Parasitemia*; 2001.
- (181) Deraney, R. N.; Mace, C. R.; Rolland, J. P.; Schonhorn, J. E. *Anal. Chem.* **2016**, *88* (12), 6161.
- (182) Snowy Range Instruments. Orbital Raster Scanning <http://www.wysri.com/cbex/> (accessed May 13, 2018).
- (183) Michen, B.; Geers, C.; Vanhecke, D.; Endes, C.; Rothen-Rutishauser, B.; Balog, S.; Petri-Fink, A. *Sci. Rep.* **2015**, *5*.
- (184) Vivid Plasma Separation Membrane <https://shop.pall.com/us/en/medical/advanced-materials/diagnostics/vivid-plasma-separation-membrane-zidgri78lls> (accessed May 14, 2018).
- (185) World Health Organization. *How to use a rapid diagnostic test (RDT): A guide for training at a village and clinic level*; 2009.
- (186) Crystran. Raman Substrate Materials <https://www.crystran.co.uk/raman-substrate-materials> (accessed Mar 1, 2018).
- (187) Prussian Blue Stain [http://www.ihcworld.com/\\_protocols/special\\_stains/prussian\\_blue.htm](http://www.ihcworld.com/_protocols/special_stains/prussian_blue.htm) (accessed Apr 15, 2018).
- (188) Wood, B.; Bailo, E.; Khiavi, M.; Tilley, L. *Nano Lett.* **2011**, *11*, 1868.
- (189) Hobro, A. J.; Pavillon, N.; Fujita, K.; Ozkan, M.; Coban, C.; Smith, N. I. *Analyst* **2015**, *140*, 2350.
- (190) Dzakah, E. E.; Kang, K.; Ni, C.; Tang, S.; Wang, J.; Wang, J. *Malar. J.* **2014**, *13* (1), 272.
- (191) Han, K. N.; Choi, J. S.; Kwon, J. *Sci. Rep.* **2016**, *6* (February), 1.
- (192) Mosier-Boss, P. A.; Putnam, M. D. *Anal. Chem. Insights* **2013**, *8* (1), 83.
- (193) Wood, B. R.; Langford, S. J.; Cooke, B. M.; Lim, J.; Glenister, F. K.; Duriska, M.; Unthank, J. K.; Mcnaughton, D. *J. Am. Chem. Soc.* **2004**, *126* (30), 9233.

## Appendices

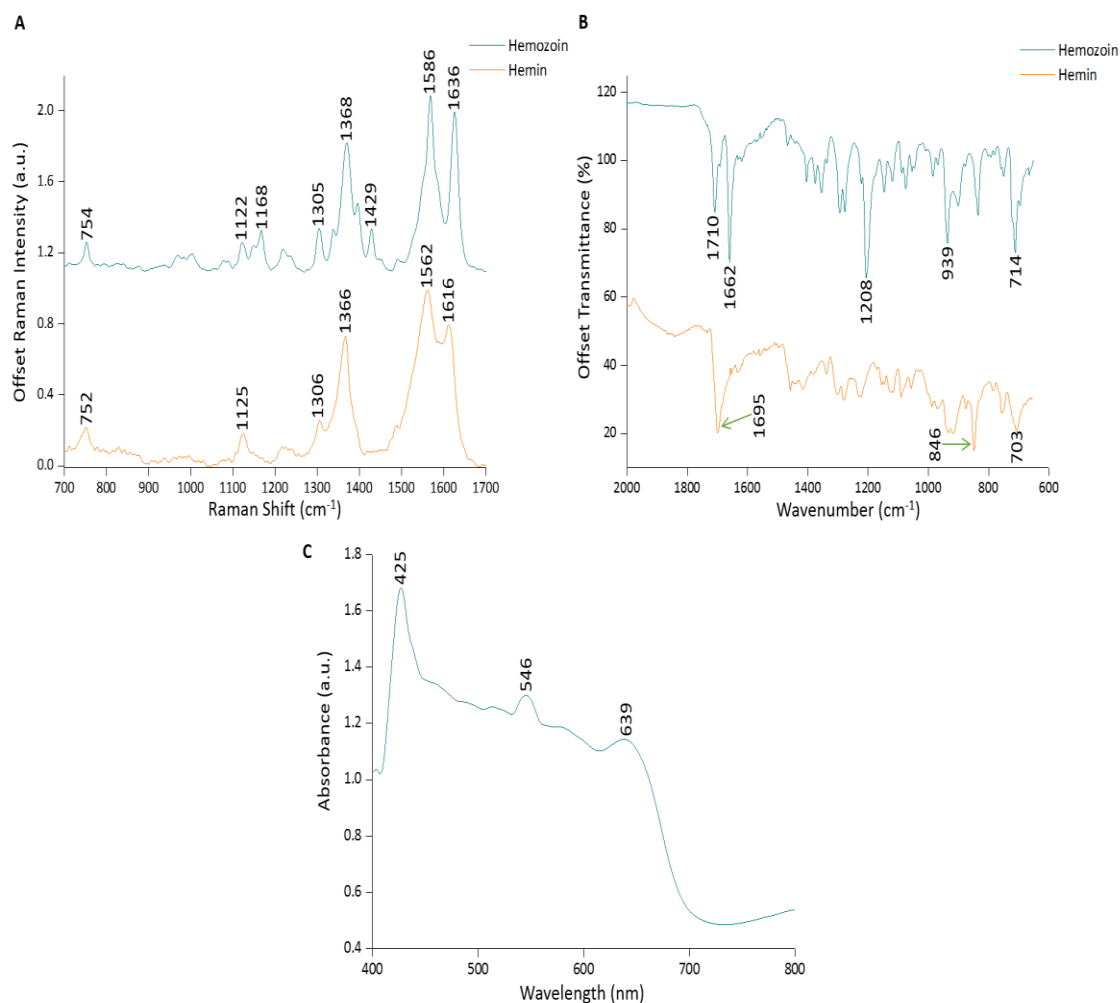
---

**Appendix I:** Characterisation of synthesised  $\beta$ -hematin crystals.

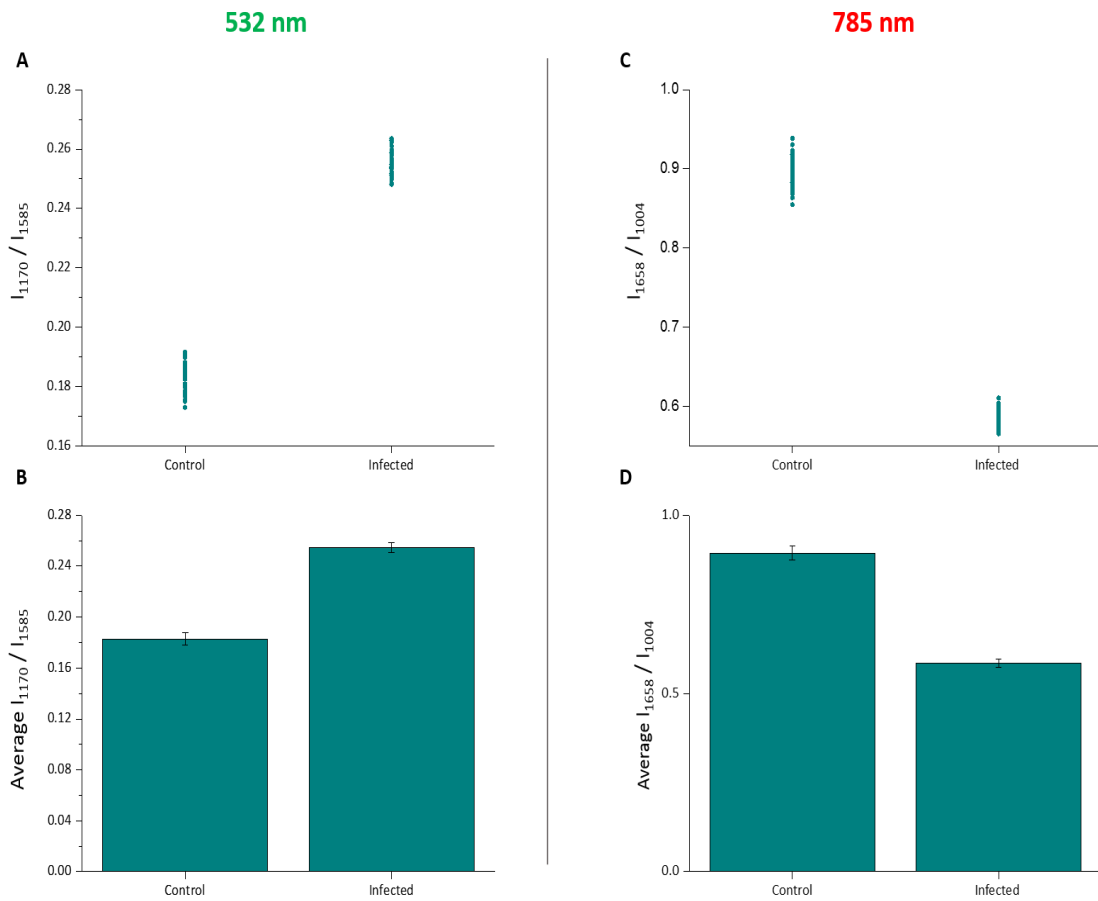
**Appendix II:** Empirical analysis using different Raman peaks for each wavelength.

**Appendix III:** Comparison of core structures of Hb and Hz.

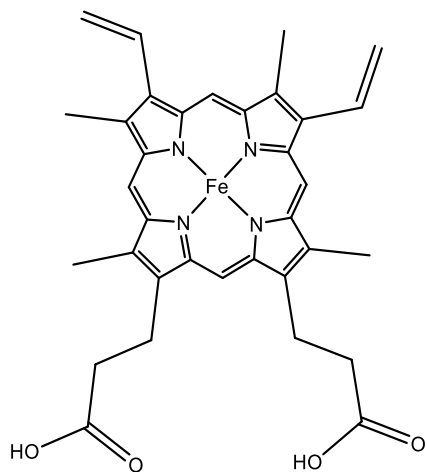
**Appendix IV:** Average *in-vivo* raw spectra of Mouse 2 liver and spleen.



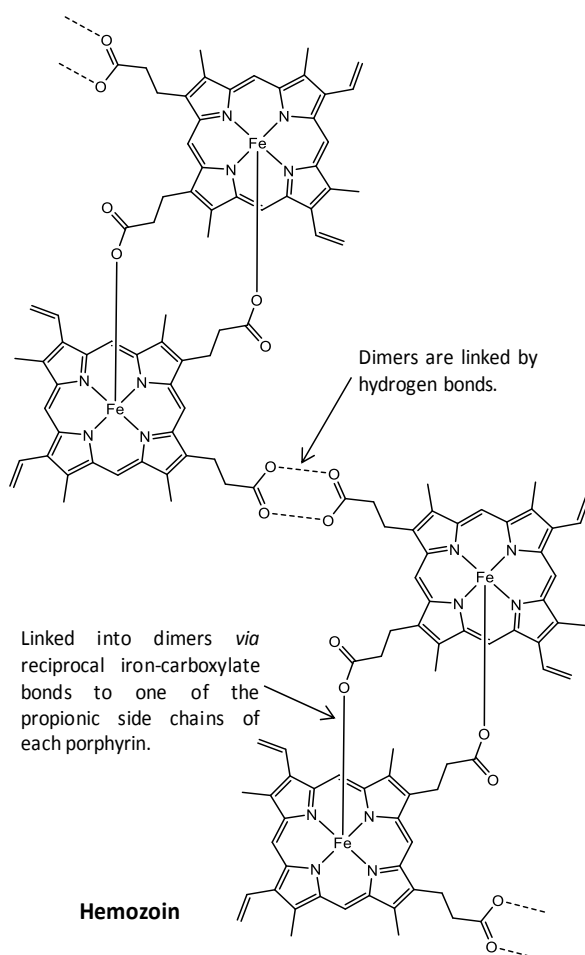
**Appendix I** Characterisation of synthesised  $\beta$ -hematin (synthetic Hz). (A) Raman spectra of starting material, hemin, and synthesised  $\beta$ -hematin (labelled as hemozoin). Both gave rise to similar Raman spectra because of their structural similarities. However, there were some relative intensity differences between individual Raman bands, especially in the 1500 – 1650  $\text{cm}^{-1}$  region where the two peaks in the hemozoin spectrum were more intense and well resolved. Also, hemozoin had a band at  $\sim 1168 \text{ cm}^{-1}$  that was not present in the hemin spectrum. (B) FTIR spectra of starting material, hemin, and synthesised hemozoin. Spectra were similar to those previously reported for both compounds.<sup>61,118,186</sup> Two sharp peaks were present in the hemozoin spectrum,  $\sim 1662$  &  $1710 \text{ cm}^{-1}$ , that appeared as only one peak in the hemin spectrum. These bands were assigned to the carbonyl stretching mode of the propionate linkage and hydrogen-bonded carboxylate group that links the dimers together, respectively. Also, a peak at  $1208 \text{ cm}^{-1}$  in the hemozoin spectrum was assigned to C – O stretching vibration of the propionate linkage. (C) UV-visible spectrum of synthesised hemozoin crystals. This showed the key absorption bands of the synthesised hemozoin. Excitation of hemozoin in 425 nm region would lead to enhancement of Soret bands, whereas, in the region above this (i.e. 532 nm that was used in this project) you get enhancement of the Q-absorption bands.<sup>112,113</sup> The absorption at  $\sim 546 \text{ nm}$  in the UV-visible spectrum indicates resonance enhancement would be gained by exciting hemozoin with a 532 nm excitation laser.



**Appendix II** Empirical analysis results using different peak ratios. (A) Empirical analysis results for alternative peaks at 532 nm and 785 nm. (A) Scatter plot of the peak intensity ratios ( $I_{1170} / I_{1585}$ ) for the 43 average infected and 43 uninfected Raman spectra analysed with 532 nm laser excitation. (B) Average intensity ratio plots for the control ( $0.18 \pm 0.01$ ) and infected ( $0.26 \pm 0.01$ ) data sets at 532 nm (C) Scatter plot of peak intensity ratios ( $I_{1658} / I_{1004}$ ) for 43 average Raman spectra from all the control and malaria infected mice spleen tissue imaged with a 785 nm laser excitation. (D) Average intensity ratio plots for the control ( $0.89 \pm 0.02$ ) and infected ( $0.58 \pm 0.01$ ) 785 nm data sets. A clear separation of the two data sets at both excitation wavelengths was observed, with little intra-sample variability. This difference in mean ratios for both the 532 nm and 785 nm data were shown to be statistically relevant (unpaired Student's t-test,  $p < 0.0001$ ). Error bars highlight the standard deviation between the control and infected datasets, respectively.

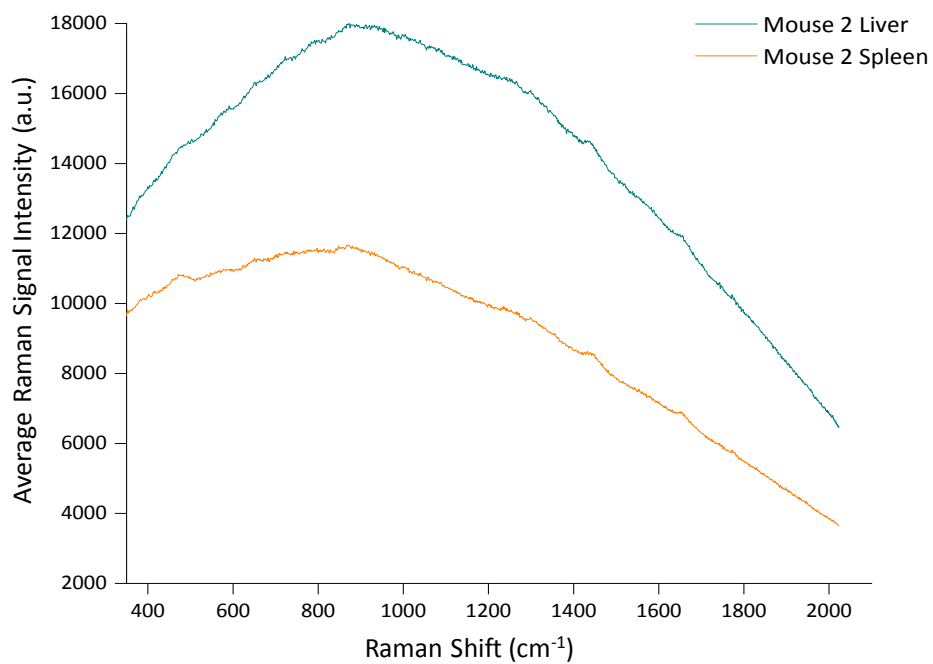


***ferrous [Fe<sup>II</sup>] protoporphyrin IX***  
**Heme**



**Hemozoin**

**Appendix III** Core heme-structure of hemoglobin and hemozoin units, highlighting the structural similarities of the two compounds. Hemoglobin is composed of 2  $\alpha$ -polypeptide chains plus 2  $\beta$ -polypeptide chains, with inorganic heme structure. The iron core can be in either +2 or +3 oxidation state. Shown below is the core heme structure of hemoglobin which is the basic building block for hemozoin. Hemozoin consists of an array of hematin units (oxidised form of heme), linked into dimers through reciprocal iron-carboxylate bonds between central iron atoms of one heme and the propionic acid side chain of another. These dimers are then connected by hydrogen bonding to build a large regular network





**Appendix IV** Average raw *in-vivo* spectra from infected Mouse 2 liver and spleen showing the large fluorescence backgrounds due to tissue autofluorescence encountered when recording Raman point spectra of these organs. This was also observed with *ex-vivo* analysis for all mice. Mouse 2 liver (cyan) and Mouse 2 spleen (orange) spectra are the average of 3 spectra taken from different points on the organ. Spectra were recorded with 1 s acquisition time and 0.45 mW 785 nm laser excitation.



Cite this: *Analyst*, 2018, **143**, 157

## Development of a label-free Raman imaging technique for differentiation of malaria parasite infected from non-infected tissue†

Laura Frame, <sup>a</sup> James Brewer,<sup>b</sup> Rebecca Lee,<sup>b</sup> Karen Faulds<sup>a</sup> and Duncan Graham <sup>\*a</sup>

During malarial infection, the host uses the spleen to clear the malaria parasites, however, the parasites have evolved the ability to bind to endothelial receptors in blood vessels of tissues to avoid removal, known as sequestration, and this is largely responsible for the symptoms and severity of infection. So a technique which could non-invasively diagnose tissue burden could be utilised as an aid for localised malaria diagnosis within tissue. Raman spectroscopy is a label-free imaging technique and can provide unique and chemically specific Raman 'fingerprint' spectrum of biological samples such as tissue. Within this study, Raman imaging was used to observe the changes to the molecular composition of mice spleen tissue under malarial infection, compared with non-infected samples. From analysis of the Raman imaging data, both tissue types showed very similar spectral profiles, which highlighted that their biochemical compositions were closely linked. Principal component analysis showed very clear separation of the two sample groups, with an associated increase in concentration of heme-based Raman vibrations within the infected dataset. This was indicative of the presence of hemozoin, the malaria pigment, being detected within the infected spleen. Separation also showed that as the hemozoin content within the tissue increased, there was a corresponding change to hemoglobin and some lipid/nucleic acid vibrations. These results demonstrate that Raman spectroscopy can be used to easily discriminate the subtle changes in tissue burden upon malarial infection.

Received 25th October 2017,  
Accepted 10th November 2017

DOI: 10.1039/c7an01760j

rsc.li/analyst

## Introduction

Malaria is a mosquito-borne infectious disease, caused by the *Plasmodium* parasite<sup>1</sup> and is a leading cause of morbidity and mortality in the developing world.<sup>2</sup> Five species are known to cause malaria infection in humans, with *Plasmodium falciparum* (*P. falciparum*) being responsible for a large number of cases in Africa.<sup>1,3</sup>

During the erythrocytic infection phase, the parasite catabolises up to 80%<sup>4</sup> of the hosts' hemoglobin. This occurs within the digestive vacuole of the parasite<sup>5</sup> and produces free heme as a by-product (ferrous [Fe<sup>II</sup>] protoporphyrin IX),<sup>6</sup> which is toxic to the parasite.<sup>5</sup> To detoxify this, the parasite oxidises it to an insoluble, crystalline material known as hemozoin or the

malaria pigment.<sup>5,7</sup> At the end of the erythrocytic cycle, red blood cells (RBCs) rupture, releasing hemozoin and parasites into the bloodstream, with the parasites going on to infect further RBCs and continue the cycle of infection. While hemozoin, under physiological conditions, is not degraded and circulates in the bloodstream until it is digested by macrophages present within specific organs.<sup>7</sup> The spleen is the primary organ involved in the development of an immune response<sup>8</sup> during the erythrocytic stage of infection along with the elimination of parasitised RBCs and hemozoin.<sup>9,10</sup> However, *P. falciparum* proteins on the surface of infected erythrocytes give these cells the ability to bind to endothelial receptors in blood vessels of tissue, leading to sequestration<sup>2,11</sup> of these infected cells and hence reduced clearance from the bloodstream.<sup>2</sup> Sequestration of parasites into tissue is largely responsible for the severity and symptoms of infection,<sup>12,13</sup> therefore, a technique which could non-invasively detect tissue burden would be a great step forward.

Raman spectroscopy has been extensively used for the identification of malaria infection most commonly *via* the detection of hemozoin. It has been widely reported by groups including Frosch *et al.*<sup>4</sup> and Wood *et al.*<sup>14</sup> that the choice of Raman exci-

<sup>a</sup>Centre of Molecular Nanometrology, Department of Pure and Applied Chemistry, University of Strathclyde, Technology and Innovation Centre, 99 George Street, G1 1RD, UK. E-mail: Duncan.graham@strath.ac.uk

<sup>b</sup>Institute for Infection, Immunity and Inflammation, University of Glasgow, G12 8QQ, UK

†Electronic supplementary information (ESI) available. See DOI: 10.1039/c7an01760j

tation wavelength is key to gaining selective enhancement of hemoglobin and hemozoin bands over other non-resonant cellular components. Wood *et al.*<sup>15</sup> reported that by exploiting the resonance Raman characteristics of hemozoin, coupled with partial dark field microscopy, there was potential to detect low-pigmented phases of the malaria parasite's life-cycle within infected erythrocytes. More recently, Hobro *et al.*<sup>16</sup> applied resonance Raman imaging to study the progression of malaria infection *via* blood and plasma samples. They showed that within infected blood samples, changes associated with a loss of hemoglobin and an increase in hemozoin could be detected after four days of infection. However, hemozoin detection limits were shown to be reduced to only one day, following *Plasmodium* infection, when plasma samples were analysed due to a reduced heme background. Resonance Raman spectroscopy has also been used within a multimodal imaging approach to study the disease mechanisms of murine cerebral malaria.<sup>17</sup> This work by Hackett *et al.*<sup>17</sup> showed strong evidence that during cerebral malaria infection iron-mediated protein oxidation occurs within the tissue.

These studies highlight how valuable Raman spectroscopic techniques are for the study of biological matrices within malarial infection. Because Raman spectroscopy is a powerful, label-free technique, it can provide a unique and chemically specific Raman 'fingerprint' spectrum of biological samples.<sup>18–20</sup> It has a number of advantages for studying these types of materials including requiring minimal to no sample preparation;<sup>18</sup> being a non-destructive technique;<sup>21</sup> and allowing specific chemical information to be gained without the use of stains.<sup>22</sup> During the pathogenesis of disease, biological alterations occur, which lead to changes in the biochemical composition of affected tissues. These changes in structure, concentration and composition of biomolecules can be reflected in the Raman spectra of tissue samples. Indeed, Raman spectroscopy has been used to study the subtle molecular changes in tissue samples associated with other diseases including, lung<sup>23</sup> cancer; breast<sup>20,24</sup> cancer; and diabetes.<sup>18</sup>

In this work, we used Raman spectroscopic imaging to study the changes in the biochemical composition of mouse spleen tissue sections following infection with the rodent parasite, *Plasmodium berghei* (*P. berghei*). We compared the Raman spectra of infected with non-infected samples to detect changes in the Raman spectral signature associated with infection. The multivariate chemometric analysis technique, principal component analysis (PCA) was applied to decompose the spectral data into components and attempt to identify subtle changes to biological components within tissue sections which could differentiate infected tissue burden from non-infected samples.

## Materials and methods

### Infections and tissue preparation

Procedures on mice were approved following local ethical review by the University of Glasgow Animal Procedures and

Ethics Committee and were performed in strict accordance with the UK Home Office Animals (Scientific Procedures) Act 1986 (project licence no. P2F28B003). Two female, BALB/c mice (Harlan, Bicester, UK; 6–8 weeks old) were infected with asynchronous *P. berghei* ANKA, and euthanised when peripheral blood parasitemia reached 5%. At this level, although high, the infection is asymptomatic in BALB/c mice. Spleens were removed from these and from two uninfected control mice and embedded in tissue freezing medium (Tissue-Tek O. C.T.).<sup>25</sup> This freezing medium was used to preserve the tissue structure. Frozen tissue blocks were then positioned in a cryostat chamber at  $-22\text{ }^{\circ}\text{C}$ , cut into sections with a thickness of  $10\text{ }\mu\text{m}$  and placed on poly-L-lysine glass slides with Tissue-Tek O.C.T. Ten tissue sections were taken from the infected spleens, along with a further ten from the uninfected spleens. Tissue sections on glass slides were stored at  $-20\text{ }^{\circ}\text{C}$  prior to analysis. Spleen tissue was chosen as it is a key tissue for the sequestration of the parasite.

### Reference spectra

Synthetic hemozoin was prepared using methods reported by Egan *et al.*<sup>26,27</sup> (full synthetic method is given in ESI S1†) and a  $2.5\text{ mg mL}^{-1}$  solution prepared with PBS (10 mM, pH 7.2). Hemoglobin was purchased from Sigma-Aldrich and a  $10\text{ mg mL}^{-1}$  solution prepared with PBS.  $100\text{ }\mu\text{L}$  of each solution were spotted on glass coverslips and allowed to dry overnight before analysis.

### Raman spectroscopy

Tissue sections were left to thaw at room temperature, washed once with PBS (10 mM, pH 7.2) and finally rinsed in  $\text{d.H}_2\text{O}$ . Raman mapping was performed using a Renishaw inVia Raman spectrometer equipped with 532 nm laser excitation (5% laser power, 1 mW) and an  $1800\text{ l mm}^{-1}$  grating. Raman images of uninfected and infected malaria tissue were recorded using a  $\times 50$  objective (NA = 0.75) with an integration time of 3 s per spectrum, a step size of  $1\text{ }\mu\text{m}$ , and in the spectral range of  $680\text{--}2330\text{ cm}^{-1}$ .

Hemoglobin and hemozoin reference spectra were collected using a  $\times 20$  objective, 30 s acquisition time per spectra and a 532 nm laser excitation (1% laser power, 0.1 mW).

### Data pre-processing

In all datasets, a cosmic ray removal algorithm was first applied within WiRE 4.2 software. This algorithm sets values for width and height of features to detect potential cosmic rays, which are then accepted or rejected by the programmer. Noise filtering was then applied within the same software, to reduce the level of random noise within the data whilst maintaining the important Raman spectral features. This pre-processing method applies a form of PCA to the dataset, which subsequently provides scores and loadings for each principal component (PC) to determine whether components primarily relate to real Raman signals or noise. The optimum number of PCs, which describe all the real Raman signal with minimal noise interference, can then be selected for each Raman map.



Raman spectra were baseline corrected using an asymmetric least square smoothing algorithm<sup>28</sup> operating in Matlab R2013a software (The MathWorks, Natick, MA, USA). Finally, all datasets were truncated so only the fingerprint region of interest was studied (700–1700  $\text{cm}^{-1}$ ).

The reference spectra shown are the average of five spectra, that were baselined using the same asymmetric least square smoothing algorithm as above.

### Empirical analysis

In this study, the empirical analysis focused on the ratio of the Raman peak intensity at  $\sim 745 \text{ cm}^{-1}$  ( $\nu_{15}$  hemoglobin),<sup>29,30</sup> to the peak intensity at  $\sim 1307 \text{ cm}^{-1}$  ( $\nu_{21}$  hemoglobin & lipids)<sup>18,29</sup> for both tissue types. An unpaired student's *t*-test was used to assess whether the difference in the Raman intensity ratio ( $I_{745}/I_{1307}$ ) between non-infected and infected tissues was statistically significant.<sup>18,19</sup> To manage the data for analysis, all infected Raman maps were combined to give one large data matrix containing thousands of Raman spectra, the same process was carried out with the uninfected data. These were

then averaged to leave 43 final infected Raman spectra and 43 control spectra ( $n = 43$ ). These data were subsequently used for empirical and multivariate analysis. The intensity ratios for all samples were plotted to observe sample distribution, along with the average intensity ratio plot for both the control and infected tissue. This analysis was performed on the same data set, used for the PCA model.

### Multivariate analysis

PCA was applied to highlight any spectral separation between the control and infected data sets using Matlab software version R2013a (The MathWorks, Natick, MA, USA). Multiple maps for both tissue types were combined and averaged to give 43 final spectra for both the control and infected tissue data sets. The dataset was then normalised and mean centred prior to PCA being applied. Principal component one (PC1) was then plotted against principal component two (PC2). The loadings plots were also plotted to determine correlation. All analysis within Matlab software was performed using custom scripts.

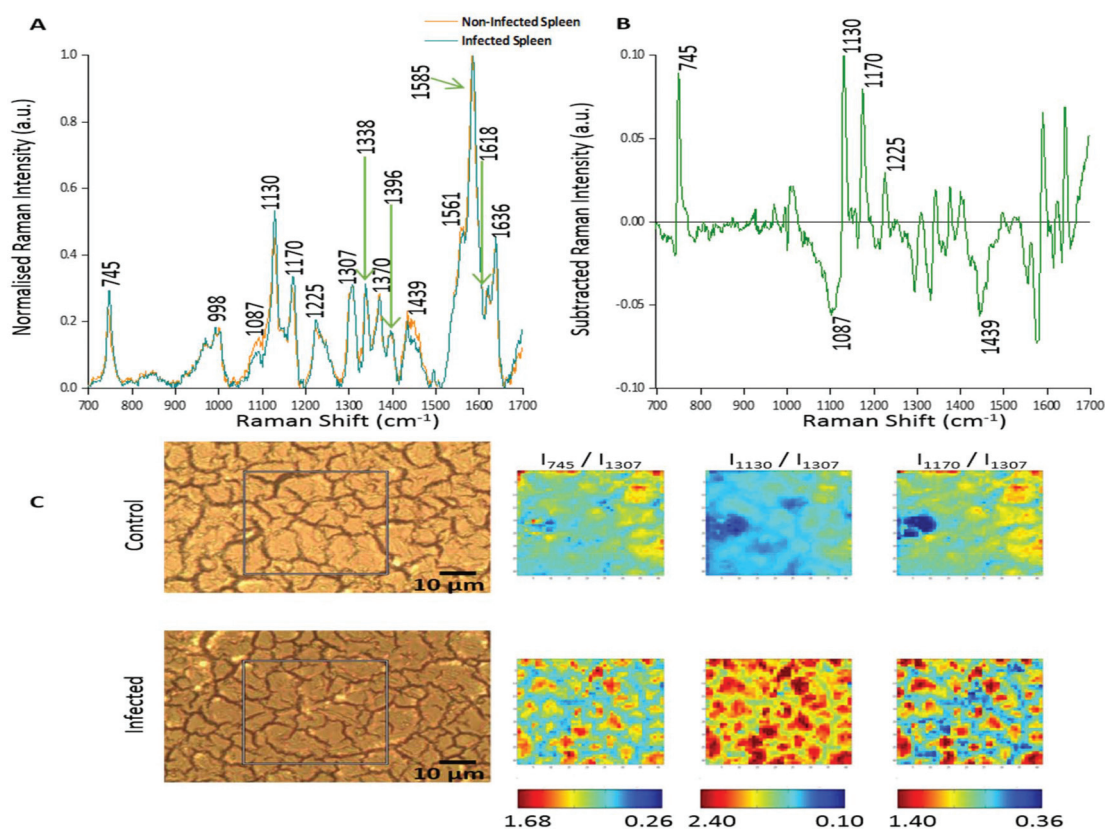


**Fig. 1** Analysis of Raman peak intensity for control and *P. berghei*-infected tissue sections. (A) Averaged, normalised spectra from a mapped area of control and infected tissue. Spectra were then normalised against the peak at  $1585 \text{ cm}^{-1}$ . Tentative peak assignments are also given in Table 1. (B) Subtracted Raman spectrum. The average, normalised control spectrum was subtracted from the average, normalised infected spectrum, both shown in (A), to highlight any potential biological components that were being altered within the malaria infected tissue. (C) Image shows white light images of both tissue sections, with the grey box indicating the area that was mapped, along with peak intensity ratio maps for selected Raman peaks. Intensity ratio maps were created using the peak intensities for:  $745 \text{ cm}^{-1}$ ,  $1130 \text{ cm}^{-1}$ ,  $1170 \text{ cm}^{-1}$ , and  $1307 \text{ cm}^{-1}$  ( $I_{745}/I_{1307}$ ;  $I_{1130}/I_{1307}$ ;  $I_{1170}/I_{1307}$ ). These ratio maps visually show relative changes in the intensity of these Raman peaks within the area of *P. berghei*-infected tissue that was mapped compared to the uninfected area. These maps suggest an increase or alteration to some key biological components within the infected tissue including, multiple hemoglobin vibrations,<sup>29</sup> lipids,<sup>31</sup> and proteins.<sup>30</sup>

**Table 1** Tentative peak assignments for the main peaks observed in the spectral profile for both non-infected and *P. berghei* infected spleen samples

| Raman shift (cm <sup>-1</sup> ) | Assignment <sup>a</sup>  |
|---------------------------------|--|
| 745                             | $\nu_{15}$ Hb [ $\nu$ (pyr breathing)]                                       |
| 998                             | Proteins (Phe), $\nu_{45}$ Hb [ $\nu$ (CC) <sub>asym</sub> ]                 |
| 1087                            | DNA/nucleic acids [ $\nu_s$ (PO <sub>2</sub> <sup>-</sup> ), $\nu$ (CC)], Hb |
| 1130                            | Lipids, $\nu_5$ Hb [ $\delta$ (=CH <sub>2</sub> ) <sub>4</sub> ]             |
| 1170                            | Proteins (Tyr), $\nu_{30}$ Hb [ $\nu$ (pyr half-ring) <sub>asym</sub> ]      |
| 1225                            | Proteins (amide III), $\nu_{13}/\nu_{42}$ Hb [ $\delta$ (CH)]                |
| 1307                            | Lipids, $\nu_{21}$ Hb [ $\delta$ (CH)]                                       |
| 1338                            | Nucleic acid modes, $\nu_{41}$ Hb [ $\nu$ (pyr half-ring) <sub>sym</sub> ]   |
| 1370                            | $\nu_4$ Hb [ $\nu$ (pyr half-ring) <sub>sym</sub> ]                          |
| 1396                            | CH <sub>2</sub> deformation, $\nu_{20}$ Hb [ $\nu$ (pyr quarter-ring)]       |
| 1439                            | Lipids [ $\delta$ (CH <sub>2</sub> )]  |
| 1561                            | $\nu_{11}$ Hb [ $\nu$ (CC)]  |
| 1585                            | $\nu_{37}$ Hb [ $\nu$ (CC) <sub>asym</sub> ]                                 |
| 1618                            | $\nu_{19}$ Hb [ $\nu$ (CC) <sub>asym</sub> ]                                 |
| 1636                            | Proteins (amide I), $\nu_{10}$ Hb [ $\nu$ (CC) <sub>asym</sub> ]             |

<sup>a</sup> Abbreviations:  $\nu$  – stretch vibration;  $\delta$  – in-plane bending vibration; sym – symmetric; asym – asymmetric; Hb – hemoglobin; Phe – phenylalanine; Tyr – tyrosine. Assignments from ref. 16, 18 and 29–31.

## Results and discussion

### Average spectra of non-infected and malaria parasite infected tissue

In this study two approaches were used to analyse the large spectral data sets. Firstly, spectral features were studied and changes in relative peak intensity investigated using intensity ratio maps and empirical analysis. The second approach used PCA to determine the primary spectral features resulting in correlations or anti-correlation between the infected and non-infected tissue, by creating principal components to explain the data set variance in an unsupervised manner.

Fig. 1A shows the averaged, normalised Raman spectra obtained from a non-infected (control) tissue map and a *P. berghei* infected mouse spleen tissue map. Both tissue types showed a very similar spectral profile, highlighting that the biochemical compositions were closely linked. Tentative peak assignments of the Raman bands are listed in Table 1. However, differences in the relative Raman peak intensities for infected vs. control tissue were observed. These were highlighted through subtraction of the average, normalised control spectra from the infected (Fig. 1B). This emphasised some peaks that appeared to increase ( $\sim 745$ , 1130, 1170 and 1225 cm<sup>-1</sup>) and decrease ( $\sim 1087$  and 1439 cm<sup>-1</sup>) in Raman signal intensity within the *P. berghei* infected tissue compared with the control. This change in relative peak intensity suggests an alteration in the biological composition of the spleen at this level of infection, characterised by changes in level and/or composition of the biological species assigned to these Raman signals.

Intensity ratio maps (Fig. 1C) were created to visually show these relative peak changes, using the 1307 cm<sup>-1</sup> peak as a constant background. These heat intensity maps showed a clear overall increase in the peak intensity ratios within the

infected mapped areas compared to the control samples. This suggests alterations to biological components including hemoglobin<sup>29,32</sup> ( $\sim 745$ , 1130 and 1170 cm<sup>-1</sup>), lipids<sup>30</sup> ( $\sim 1130$  cm<sup>-1</sup>) and other proteins<sup>30</sup> ( $\sim 1170$  cm<sup>-1</sup>) at this level of *P. berghei* infection. Ratio maps were also created for different samples to show this overall increase was common throughout the infected tissue (ESI Fig. S2†). Within these maps, for both uninfected and infected samples, particularly intense regions are present (Fig. 1C and ESI Fig. S2†). This can be explained through enhanced Raman intensity from resonance contributions of the biological components within these areas of tissue. These ratio maps visually show relative changes in biological peaks in a simple manner and can be used alongside empirical analysis and PCA to aid in classification of tissue types from Raman spectroscopy data.

### Empirical analysis of Raman spectra

Diagnostic algorithms based on peak intensity ratios have been widely employed in the literature for tissue classification using Raman spectroscopy.<sup>18,19,23</sup> These have been shown to successfully correlate variations in tissue spectra with tissue pathology<sup>19</sup> in a simple manner.

An empirical analysis based on the peak intensity ratio of two Raman bands was used for tissue classification within this study. Fig. 2A shows the scatter plot of the ratio of Raman peak intensity at 745 cm<sup>-1</sup> to 1307 cm<sup>-1</sup> ( $I_{745}/I_{1307}$ ) for the 43 averaged *P. berghei* infected samples and 43 uninfected samples. A clear separation was observed in the scatter plot for the two data sets, with replicate data within each tissue type

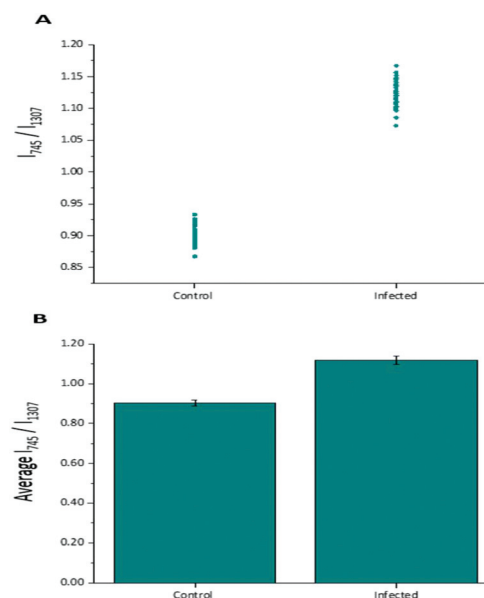


**Fig. 2** Empirical analysis results. (A) Scatter plot of peak intensity ratios ( $I_{745}/I_{1307}$ ) for 43 average Raman spectra from all the control and malaria infected mice spleen tissue that were mapped. A clear separation of the two data sets was observed, with little intra-sample variability. (B) Average intensity ratio plots for the control ( $0.903 \pm 0.015$ ) and infected ( $1.119 \pm 0.021$ ) data sets. This difference in mean ratios was shown to be statistically relevant (unpaired Student's *t*-test,  $p < 0.0001$ ).

being grouped closely together, indicating little intra-sample variation in the intensity ratios. The mean ratio values (mean  $\pm$  std. dev.) for both control ( $0.903 \pm 0.015$ ) and infected ( $1.119 \pm 0.021$ ) data sets were also plotted (Fig. 2B). It was shown that the differences between the mean ratios for each tissue type were statistically relevant (unpaired student's *t*-test,  $p < 0.0001$ ). Infected tissue showed a higher ratio value compared with control, this could be explained by the increase in heme-based Raman vibrations ( $\sim 745 \text{ cm}^{-1}$  assigned to  $\nu_{15} \text{ Hb}^{29}$ ) due to the presence of hemozoin within the infected samples.

From these results, this intensity ratio is a potential simple and reliable marker to indicate the presence of infection. It has also been shown that other peak ratios can also be used to classify the two tissue types with good results (ESI Fig. S3†). However, this method does not consider the entire Raman spectrum. To help improve tissue analysis and classification, PCA was employed to highlight the most diagnostically significant Raman peaks.

### Principal component analysis

PCA was used to analyse this data set to better distinguish the spectral differences between the non-infected and infected spleen tissue. Fig. 3 shows the scores plot for PC1 (97.6% var-

iance) and PC2 (1.45% variance), along with the corresponding loadings vectors. As can be seen from the scores plot (Fig. 3A) PC1 was primarily responsible for the separation of the two tissue types. The loadings plot (Fig. 3B) for PC1 indicated that the peaks in the negative half of the plot were spectrally important for describing the separation of the infected tissue ( $\sim 750$ , 1130, 1170, 1225, 1370, 1529, 1588 and  $1628 \text{ cm}^{-1}$ ), with the latter few being more indicative of hemozoin than hemoglobin. The negative peaks at  $\sim 1529$ , 1588 and  $1628 \text{ cm}^{-1}$  matched closely with that of the hemozoin reference spectra in Fig. 4 (core structures of hemoglobin and hemozoin shown in ESI S4† to highlight structural similarities) and therefore suggested detection of the insoluble pigment by Raman. The negative  $\sim 1370 \text{ cm}^{-1}$  peak was present in both reference spectra; however, it was much more prominent within hemozoin and so suggested that hemozoin was contributing to this peaks appearance within the PC1 loadings plot. It is well known that hemozoin accumulates within the spleen<sup>8,9</sup> (presence of hemozoin within the infected spleen can be seen in stained tissue images, ESI S5†), therefore it follows that there will be an associated increase in concentration of heme-based Raman vibrations. This is clearly shown in this PCA model as many of these peaks separating the infected tissue from the

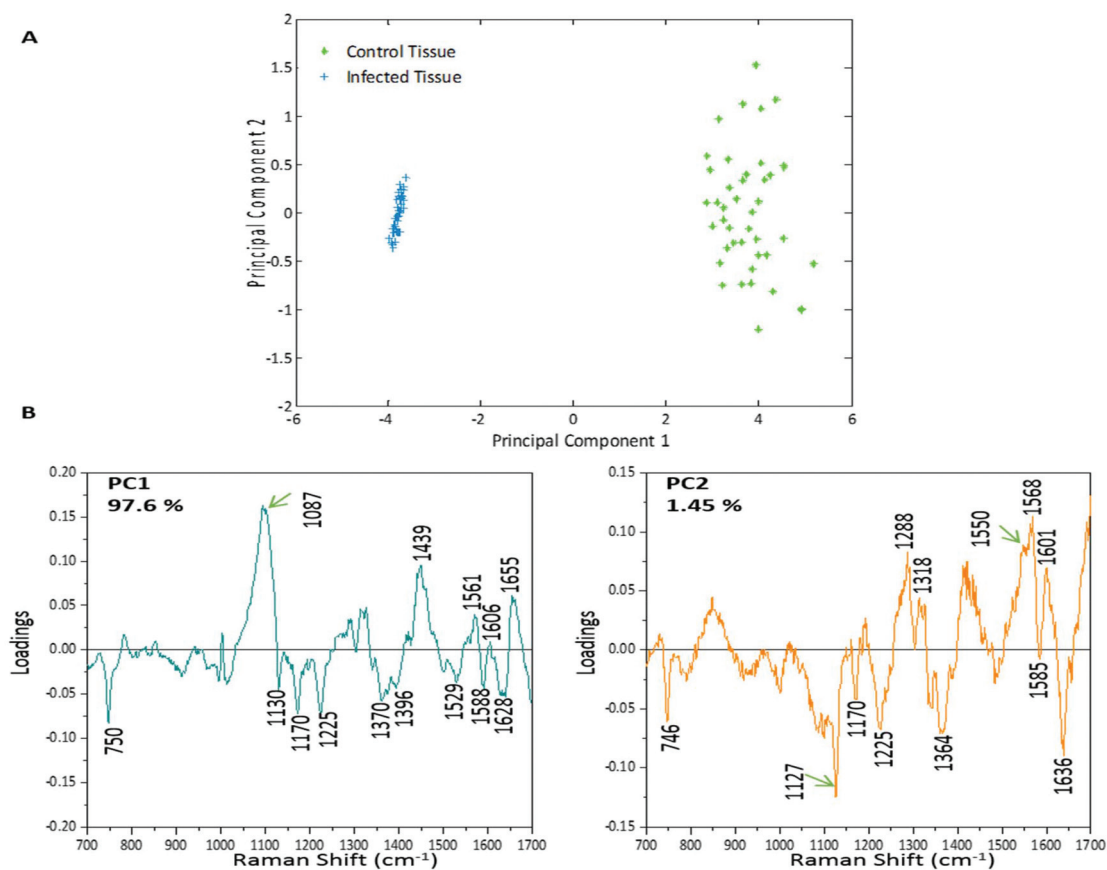


**Fig. 3** PCA plot for control and malaria infected samples from mouse spleen tissue sections. (A) Scores plot showing very clear separation of the control (green) and infected (blue) data sets. Separation is occurring mainly along PC1, with little separation along PC2. (B) Loadings plots for PC1 and PC2, with the main peaks in both indicated. The peaks in the negative half of PC1 are responsible for the separation of the infected samples along PC1 away from the control samples.

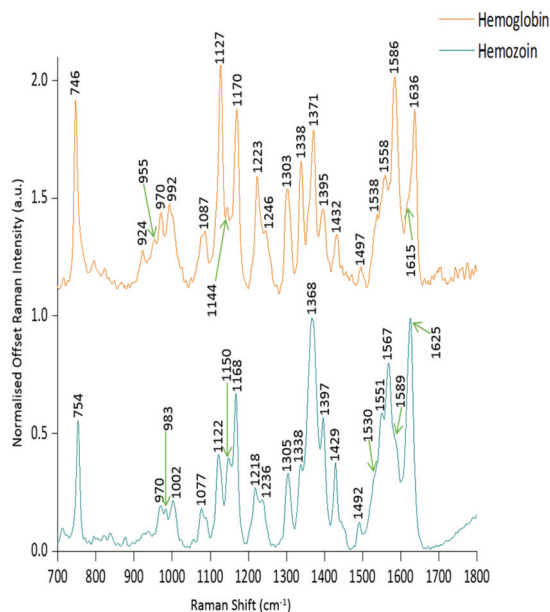


**Fig. 4** Raman reference spectra of hemoglobin and hemozoin. The spectra shown are the average of five spectra and have been baseline corrected, normalised to the highest peak and offset for clarity. Key Raman bands are also indicated.

uninfected samples can be assigned to heme-vibrations, including hemozoin. Although other proteins and lipids will be present and exhibit Raman bands in similar positions to those of hemoglobin ( $\sim 1130$ ,  $1170$ ,  $1225$  &  $1396$   $\text{cm}^{-1}$ ), resonance effects would mean hemoglobin will tend to dominate the spectra (excitation in the regions of Q-absorption bands),<sup>29,32,33</sup> with the other proteins and lipids having only small contributions to the observed spectra.

Within the positive peaks in the PC1 loadings plot, the relatively broad  $\sim 1087$   $\text{cm}^{-1}$  peak is likely to have a significant contribution from hemoglobin (Fig. 4), however, its broadness suggested contributions from other components. Raman bands within this region can also be assigned to C–C and O–P–O vibrations of nucleic acids.<sup>18,30</sup> The other prominent positive peak at  $\sim 1439$   $\text{cm}^{-1}$  can mainly be assigned to Raman vibrations from lipids,<sup>18,31</sup> although it may also have slight hemoglobin contributions ( $\sim 1432$   $\text{cm}^{-1}$  peak in reference spectra). Analysis of the PC1 loadings plot indicated that at this level of *P. berghei* malaria infection Raman spectroscopy can clearly detect hemozoin accumulation within the spleen, with the positive peaks ( $\sim 1087$  and  $1439$   $\text{cm}^{-1}$ ) indicating that as the amount of hemozoin increases within the spleen there is a corresponding change to hemoglobin and some lipids/nucleic acid vibrations.

PC2 describes little separation between the control and infected samples. From the PC2 loadings plot (Fig. 3B) the positive peaks ( $\sim 1550$ ,  $1568$ ,  $1601$   $\text{cm}^{-1}$ ) originate mainly from hemoglobin vibrations, whereas the negative peaks have contributions from hemoglobin as well as from other proteins<sup>18,30</sup> ( $\sim 1170$ ,  $1225$  and  $1636$   $\text{cm}^{-1}$ ) and lipids<sup>31</sup> ( $\sim 1127$   $\text{cm}^{-1}$ ). This PCA analysis indicates that Raman imaging can easily dis-

tinguish between *P. berghei* infected spleen tissue from uninfected samples, through identification of hemozoin accumulation and alterations to other key biological components.

## Conclusions

In conclusion, a combination of Raman imaging with multivariate analysis resulted in very clear discrimination of *P. berghei* infected tissue from non-infected samples. Separation highlighted an overall increase in heme-based Raman vibrations within the infected samples, which correlates with the accumulation of hemozoin within the spleen contributing to this. Hemozoin detection was clear with the identification of key peaks occurring  $\sim 1370$ ,  $1529$ ,  $1588$ , and  $1628$   $\text{cm}^{-1}$  which matched closely with the reference spectra. Chemometric analysis also showed that at the level of *P. berghei* infection reported here, changes to hemoglobin and some other lipid/nucleic acid vibrations corresponded with an increase in hemozoin content within the spleen. Other proteins (tyrosine  $\sim 1130$   $\text{cm}^{-1}$ , and amide III  $\sim 1225$   $\text{cm}^{-1}$ ) and lipids ( $\sim 1130$   $\text{cm}^{-1}$ ) were also contributing to the separation of infected tissue from control. However, due to the resonance effects of heme-based compounds the separation contribution from these biological components would have been small.

The use of peak ratio maps and empirical analysis also highlighted changes to the biological components as you move towards an infected tissue state. These two simple data analysis methods could be used as tools in combination with the PCA to help improve efficiency of Raman tissue analysis and classification.

As the Raman imaging technique used in this study had a short penetration depth, it would not be suitable for *in vivo* diagnostics. However, with the development of spatially offset Raman spectroscopy, which allows accurate analysis through millimetres of material when obscuring barriers such as skin are present,<sup>34,35</sup> this may allow for biochemical information from tissue to be detected *in vivo* in the near future. Overall, this approach demonstrates the potential use of Raman spectroscopy to provide detailed chemical information from both malaria parasite infected and control tissue and when coupled with PCA, discrimination due to infection burden is achievable between the two sample groups.

## Conflicts of interest

There are no conflicts to declare.

## Acknowledgements

This work was supported by the University of Strathclyde. Data associated with research published in this paper is accessible at: <http://dx.doi.org/10.15129/89483183-40b2-4ebb-8b10-43a4615e40db> and <http://dx.doi.org/10.15129/b069f380-61ae-494d-9419-dcdf28a5b160>.

## Notes and references

- 1 World Health Organisation, *World Malaria Report 2015*, 2015.
- 2 W. C. Aird, L. O. Mosnier and R. M. Fairhurst, *Blood*, 2014, **123**, 163–168.
- 3 CDC: malaria parasites, <https://www.cdc.gov/malaria/about/biology/parasites.html> (accessed Sep 22, 2017).
- 4 T. Frosch, S. Koncarevic, K. Becker and J. Popp, *Analyst*, 2009, **134**, 1126–1132.
- 5 L. M. Coronado, C. T. Nadovich and C. Spadafora, *Biochim. Biophys. Acta*, 2014, **1840**, 2032–2041.
- 6 T. Frosch, S. Koncarevic, L. Zedler, M. Schmitt, K. Schenzel, K. Becker and J. Popp, *J. Phys. Chem. B*, 2007, **111**, 11047–11056.
- 7 M. Boura, R. Frita, A. Góis, T. Carvalho and T. Hänscheid, *Trends Parasitol.*, 2013, **29**, 469–476.
- 8 M. Ferrer, L. Martin-Jaular, M. De Niz, S. M. Khan, C. J. Janse, M. Calvo, V. Heussler and H. A. Del Portillo, *Parasitol. Int.*, 2014, **63**, 195–205.
- 9 H. A. DelPortillo, M. Ferrer, T. Brugat, L. Martin-Jaular, J. Langhorne and M. V. G. Lacerda, *Cell. Microbiol.*, 2012, **14**, 343–355.
- 10 C. R. Engwerda, L. Beattie and F. H. Amante, *Trends Parasitol.*, 2005, **21**, 75–80.
- 11 B. Franke-Fayard, J. Fonager, A. Braks, S. M. Khan and C. J. Janse, *PLoS Pathog.*, 2010, **6**, 1–10.
- 12 B. Autino, Y. Corbett, F. Castelli and D. Taramelli, *Mediterr. J. Hematol. Infect. Dis.*, 2012, **4**, 1–12.
- 13 D. S. Khoury, D. Cromer, S. E. Best, K. R. James, P. S. Kim, C. R. Engwerda, A. Haque and M. P. Davenport, *Infect. Immun.*, 2014, **82**, 212–220.
- 14 B. R. Wood, S. J. Langford, B. M. Cooke, F. K. Glenister, J. Lim and D. McNaughton, *FEBS Lett.*, 2003, **554**, 247–252.
- 15 B. R. Wood, A. Hermelink, P. Lasch, K. R. Bambery, G. T. Webster, M. A. Khiavi, B. M. Cooke, S. Deed, D. Naumann and D. McNaughton, *Analyst*, 2009, **134**, 1119–1125.
- 16 A. J. Hobro, A. Konishi, C. Coban and N. I. Smith, *Analyst*, 2013, **138**, 3927–3933.
- 17 M. J. Hackett, J. B. Aitken, F. El-Assaad, J. a. McQuillan, E. a. Carter, H. J. Ball, M. J. Tobin, D. Paterson, M. D. de Jonge, R. Siegele, D. D. Cohen, S. Vogt, G. E. Grau, N. H. Hunt and P. A. Lay, *Sci. Adv.*, 2015, **1**, 1–13.
- 18 K. Kochan, K. M. Marzec, K. Chruszcz-Lipska, A. Jaształ, E. Maslak, H. Musiolik, S. Chłopicki and M. Baranska, *Analyst*, 2013, **138**, 3885–3890.
- 19 S. K. Teh, W. Zheng, K. Y. Ho, M. Teh, K. G. Yeoh and Z. Huang, *Br. J. Cancer*, 2008, **98**, 457–465.
- 20 C. J. Frank, R. L. McCreery and D. C. Redd, *Anal. Chem.*, 1995, **67**, 777–783.
- 21 T. Huser and J. Chan, *Adv. Drug Delivery Rev.*, 2015, **89**, 57–70.
- 22 A. J. Hobro, N. Pavillon, K. Fujita, M. Ozkan, C. Coban and N. I. Smith, *Analyst*, 2015, **140**, 2350–2359.
- 23 Z. Huang, A. McWilliams, H. Lui, D. I. McLean, S. Lam and H. Zeng, *Int. J. Cancer*, 2003, **107**, 1047–1052.
- 24 A. S. Haka, K. E. Shafer-Peltier, M. Fitzmaurice, J. Crowe, R. R. Dasari and M. S. Feld, *Proc. Natl. Acad. Sci. U. S. A.*, 2005, **102**, 12371–12376.
- 25 Tissue-Tek O.C.T Compound and Cryomolds, <http://www.sakura.eu/Our-products/item/11/Cryotomy/48/Tissue-Tek-OCT-Compound-and-Cryomolds>, (accessed Sep 15, 2017).
- 26 T. J. Egan, D. C. Rossa and P. A. Adamsb, *FEBS Lett.*, 1994, **352**, 54–57.
- 27 T. J. Egan, W. W. Mavuso and K. K. Ncokazi, *Biochemistry*, 2001, **40**, 204–213.
- 28 P. H. C. Eilers and H. F. M. Boelens, *Life Sci.*, 2005, 1–26.
- 29 G. Rusciano, A. C. De Luca, G. Pesce and A. Sasso, *Sensors*, 2008, **8**, 7818–7832.
- 30 Z. Movasaghi, S. Rehman and I. U. Rehman, *Appl. Spectrosc. Rev.*, 2007, **42**, 493–541.
- 31 C. Krafft, D. Codrich, G. Pelizzo and V. Sergo, *Analyst*, 2008, **133**, 361–371.
- 32 M. Polakovs, N. Mironova-Ulmane, N. Kurjane, E. Reinholds and M. Grube, *Proc. SPIE*, 2008, **7142**, 1–8.
- 33 T. G. Spiro and T. C. Strekas, *J. Am. Chem. Soc.*, 1974, **96**, 338–345.
- 34 N. Stone and P. Matousek, *Cancer Res.*, 2008, **68**, 4424–4430.
- 35 M. D. Keller, S. K. Majumder and A. Mahadevan-Jansen, *Opt. Lett.*, 2009, **34**, 926–928.